



Fiber optic sensors for metrology, geophysics and strain measurements

Han Cheng Seat

► To cite this version:

Han Cheng Seat. Fiber optic sensors for metrology, geophysics and strain measurements. Optics / Photonic. Institut National Polytechnique de Toulouse - INPT, 2014. tel-01068810

HAL Id: tel-01068810

<https://theses.hal.science/tel-01068810>

Submitted on 26 Sep 2014

HAL is a multi-disciplinary open access archive for the deposit and dissemination of scientific research documents, whether they are published or not. The documents may come from teaching and research institutions in France or abroad, or from public or private research centers.

L'archive ouverte pluridisciplinaire **HAL**, est destinée au dépôt et à la diffusion de documents scientifiques de niveau recherche, publiés ou non, émanant des établissements d'enseignement et de recherche français ou étrangers, des laboratoires publics ou privés.

Habilitation
INSTITUT NATIONAL POLYTECHNIQUE DE TOULOUSE

**Fiber optic sensors for metrology, geophysics and
strain measurements**

Manuscript submitted by

Han Cheng SEAT
Optoelectronics for Embedded Systems Group
Laboratoire d'Analyse et d'Architecture des Systèmes
(LAAS-CNRS, Group OSE)

for the degree of Habilitation à Diriger les Recherches

Reviewers

Professor Brian CULSHAW (University of Strathclyde)
Professor Pascal PICART (ENSIM)
Professor Lin ZHANG (Aston University)

Examiners

Professor Thierry BOSCH (LAAS-CNRS, Groupe OSE)
Dr (DR CNRS) Jean CHERY (Géosciences Montpellier)
Dr (HDR) Pierre FERDINAND (CEA LIST, Centre de Saclay)
Professor Guy PLANTIER (ESEO)

Viva held on 18 April 2014

Summary

This HDR manuscript principally describes the research activities in which I have been involved since my appointment in August 2003 to my current laboratory, the Optoelectronics for Embedded Systems Group of the Laboratory for Analysis and Architecture Systems (LAAS-OSE). Before detailing these activities, I have also added a brief description of research work carried out during my PhD. This has been willingly added to this manuscript to demonstrate the evolution of my research activities over the past decade.

Chapter 1 is a very brief introduction to my early career as a researcher in optics and fiber optics, basically describing work carried out on ruby crystal fiber-based sensors for harsh environments during my PhD at the University of Glasgow. Results show that *c*-axis ruby crystal fibers are uniquely sensitive to temperature effects while being insensitive to high levels of strains.

Chapter 2 concerns an extrinsic-type fiber Fabry-Perot (EFFPI) interferometer which I initially developed during my post-doctoral fellowship at the *Ecole des Mines de Nantes* where I was responsible for setting up and leading the fiber optic sensing branch of the Instrumentation and Sensor Group. The proof-of-concept of the fiber interferometer was demonstrated before my departure to ENSEEIHT-INPT in Toulouse where I continue to work on its improvement at my current laboratory, LAAS-OSE, for metrology purposes. The initial polarization-based EFFPI which was developed earlier is thus described in the first half of Chapter 2 where a quadrature signal pair is obtained, hence the optical dual-cavity nature of the instrument. This is followed by its evolution into a modulation-based instrument, in the second half of the chapter, where, effectively, the introduction of a double-modulation scheme to the laser drive current enables a quadrature pair as well as the capability for detecting displacement amplitudes smaller than $\lambda/4$ to be achieved. This latter sensor has been conceived for applications in optical metrology and, more specifically, in geophysics under the ANR RISK-NAT-sponsored LINES project. Three optical fiber-based geophysics instruments have been developed during the course of this project, namely, an EFFPI-based long baseline tiltmeter (or hydrostatic leveling system, HLS), an EFFPI-based borehole tiltmeter and an EFFPI-based seismometer. The modulation-based EFFPI is currently undergoing further development as a key component of the HLS for accelerator alignment at the CERN. A TRL 7 (technology readiness level) maturity state is envisaged at the outcome of this project. The final ambitions are to attain TRL 8 and TRL 9 before production and commercialization of the instrument for geophysics and industrial applications.

Chapter 3 describes the second research activity which I lead at LAAS-OSE. This essentially involves the development of a novel technique for interrogating fiber Bragg grating-based (FBG) strain sensors based on optical feedback or self-mixing interferometry. The reflections off an FBG are retro-injected into the cavity of a laser diode, perturbing the internal fields. These result in a series of sawtooth fringes being detected by an internal photodiode and which are a function of the strength as well as frequency of the external strains applied on the FBG. This sensor has been demonstrated for dynamic strain measurements under a cantilever set-up. Further, a proof-of-concept is also experimentally demonstrated for extending the dynamic strain measurement range by 50% of the current limit via a low-frequency modulation scheme to the laser diode current.

Chapter 4 is a summary of all the administrative tasks throughout my research career. It is organized around my supervision of PhD students including post-doctoral fellows, the various research projects that I have led and a selected list of my publications. Included is also a short discussion on the perspectives for leading further research as well as my services to my research

community. I have also summarized my teaching duties and, to conclude this manuscript, my Curriculum Vitae is enclosed for perusal.

Résumé

Ce manuscrit d'Habilitation décrit les principales activités de recherche que je mène au sein du groupe Optoélectronique pour les Systèmes Embarqués du LAAS depuis 2003. Par ailleurs, j'ai volontairement inclus une brève description de mes travaux de thèse avec pour objectif de montrer l'évolution de ma recherche.

Le chapitre 1 résume donc le début de ma carrière dans le domaine de la recherche sur l'optique et les fibres optiques. Il porte essentiellement sur le développement des capteurs à fibres optiques à base de fibres cristallines de rubis pour des environnements hostiles à savoir température très élevée et déformations mécaniques très importantes. Il est à noter que ces capteurs sont insensibles aux dernières perturbations, et par conséquent, ne mesurent que la grandeur physique ciblée (c'est-à-dire température).

Le chapitre 2 contient deux parties principales et porte sur le développement initial de l'interféromètre fibré de Fabry-Pérot extrinsèque (EFFPI). Ce premier dispositif est basé sur le principe de la décomposition du mode fondamental injecté dans l'interféromètre résultant ainsi en deux signaux intrinsèques interférométriques déphasés de $\pi/2$ ou en quadrature, d'où l'EFFPI à double-cavité optiques. Malgré une très large bande passante puisqu'aucune modulation n'est appliquée sur le courant du laser utilisé, l'EFFPI à double-cavité se montre sensible au niveau de son état de polarisation lors des perturbations induites (variations de température et vibrations parasites). Pour éliminer ces sensibilités, un EFFPI à modulation est développé, comme décrit dans la deuxième partie du chapitre. Ce travail est effectué dans le cadre d'un projet ANR qui a pour objectif de développer des nouveaux instruments pour les applications géophysiques. En effet, une double modulation du courant de la diode laser est appliquée, ce qui équivaut une modulation sur la longueur d'onde du laser. Ainsi, nous obtenons une condition de quadrature où l'amplitude du déplacement ainsi que sa direction peuvent être précisément déterminées sans aucune ambiguïté. Par ailleurs, grâce à cette double modulation, l'EFFPI est aussi capable de mesurer des déplacements équivalents inférieurs à $\lambda/4$ (<327.50 nm pour $\lambda = 1310$ nm). Trois instruments opto-géophysiques ont ainsi été développés à savoir un inclinomètre longue base à fibre optique, un inclinomètre de forage à fibre optique et un sismomètre à fibre optique.

Une autre de mes activités de recherche concerne le développement de nouvelles techniques d'interrogation pour les fibres à réseaux de Bragg sous déformations mécaniques. Ces travaux sont décrits dans le chapitre 3 où le phénomène de rétro-injection optique (plus connu sous le nom de "self-mixing") est exploité pour réaliser des capteurs de contraintes (déformations mécaniques) avec une bonne précision. Le faisceau laser réfléchi par le réseau de Bragg est rétro-injecté dans la cavité laser provoquant des franges d'interférence sous forme de dents-de-scie. Ainsi, en présence d'une perturbation mécanique, ces franges dites de self-mixing sont fonction de la déformation mécanique induite dans le réseau. La faisabilité de cette technique d'interrogation est amplement démontrée. Par ailleurs, en modulant le courant du laser, nous avons pu augmenter la plage dynamique de mesure de $\sim 50\%$.

Enfin, le chapitre 4 résume toutes les tâches administratives et de responsabilités au niveau de ma recherche : l'encadrement des thèses et de chercheurs postdoctoraux, les projets de recherche et de contrats accordés ainsi qu'une liste de mes publications (sélectionnées) au cours de ces dernières années. J'ai aussi inclus une discussion sur les perspectives envisagées et envisageables sur mes activités de recherche. Pour terminer, j'ai joint un curriculum vitae démontrant mon parcours professionnel dans le domaine de la recherche scientifique.

Acknowledgements

As acknowledgements go, I would first of all like to express my gratitude and thanks to my Viva panel members all of whom have accepted to review my work as well as make the trip to Toulouse for a rather fruitful discussion. First in line, Professor Brian Culshaw for offering very helpful critiques and comments on my manuscript in his capacity as external examiner. I value your comments highly. Professor Lin Zhang next for agreeing to be one of my external examiners and for her expertise in FBG-based devices. Professor Pascal Picart, the third external examiner is also acknowledged for agreeing to grind through the manuscript as one of the experts in interferometry and interferometric techniques. Dr Pierre Ferdinand as well is acknowledged for his questions which subtly orient one beyond the limits of experimental work towards a more accomplished research vision. I hope that I have kept my "chapeau chinois" on that "vendredi Saint"! I would also like to express my gratitude to Professor Guy Plantier for accepting to sit on the panel. Human qualities abounding, I believe I have never met anyone so strong at signal processing. Last but not least, to Dr Jean Chéry, my panel president, with whom I had worked over the past four to five years on the LINES project and with whom I continue to perpetuate further collaboration, I have this to say: geophysics is not only fun but is a credible way of taking the real mickey out of an instrument in the field. It has been a great pleasure to take the stage and be counted amongst you all.

This habilitation would not have been possible if not for the encouragement and support of those who believed in me. A big Thank You must sincerely go out to my boss and friend Thierry Bosch, without whom I would never have been at ENSEEIHT in the first place. Thanks for the confidence and trust throughout the years. Notwithstanding the kidney pies, of course. Here it is, boss!

Not forgetting my dear friends Olivier and Caroline with whom I shared many a good times in the years past. Vive the cycling adventure in Ottawa! It is also a blessing that Olivier has decided to come back to Toulouse to partake in camaraderie suffering with me. Welcome back man, after Singapore.

To my colleague and friend Michel with whom I had worked on various projects. It's good to be working as a team. We should have started much earlier! Here's hoping it continues beyond LINES and the CERN.

Special dedication is extended to Françoise, dear colleague and friend as well, for wisdom and her contribution to the successful outcome of the ANR LINES project, and without whom I would have hated IT, programming and computers all my life. I still hate PCs though, but with a lot less vehemence these days. Thank you, and not just for the computers! Stay and may there be further adventures!

Acknowledgements to Francis Jayat and Clément Tronche who have had to suffer my continuous demands for service and last-minute rush work.

Acknowledgements as well to all those whose names are not mentioned here but have in one way or another made life a little more fun in the laboratory.

My heart naturally also goes out to Sabrina who patiently and understandingly shared many a nights without sleep and lots of my lousy humor during the writing up of this manuscript. Mea culpa. Thanks for all the understanding, support and hanging on throughout these taxing months.

Contents

Chapter 1 - Single-crystal fibers for sensing applications	1
1.1 Introduction	1
1.2 Laser-heated pedestal growth of SCFs	1
1.3 Ruby SCFs for fluorescence-based high temperature and strain sensing	2
1.3.1 Absorption and fluorescence spectra of ruby SCFs	3
1.3.2 Temperature dependence of ruby SCF fluorescence	3
1.3.2.1 Lifetime decay	3
1.3.2.2 R-line shifts	7
1.3.3 Strain dependence of ruby SCF fluorescence	9
1.3.3.1 Lifetime decay	9
1.3.3.2 R-line shifts	10
1.4 Conclusions and Perspectives	11
References	13
Chapter 2 - Polarization-based and dual-modulation fiber Fabry-Perot interferometry	15
2.1 Introduction	15
2.2 Polarization-based dual-cavity extrinsic EFFPI (EFFPI)	16
2.2.1 Operating principles and experimental validation	17
2.2.2 Polarization-induced influence in dual-cavity EFFPI sensor	19
2.2.3 Demodulation of dual-cavity EFFPI sensor by modified fringe-counting for displacement applications	22
2.2.4 Dual-cavity EFFPI sensor characteristics and performance	25
2.2.5 Applications to vibration measurements	27
2.3 Dual-modulation EFFPI with double reflection	31
2.3.1 Operating principles of dual-modulation EFFPI sensor	31
2.3.2 Demodulation of dual-modulation EFFPI sensor via phase tracking	34
2.3.3 Dual-modulation EFFPI sensor characteristics and performance	36
2.3.4 Applications to displacement measurements	38
2.3.5 Applications to geophysics	39
2.3.5.1 Fiber optic long baseline tiltmeter	40
2.3.5.2 Fiber optic borehole tiltmeter	43
2.3.5.3 Fiber optic seismometer	46
2.4 Conclusions and Perspectives	48
References	50

Chapter 3 - Self-mixing interrogation technique for fiber Bragg grating strain sensors	53
3.1 Introduction	53
3.2 Operating principles	54
3.3 Experimental validation and sensor characteristics under dynamic strain loading	57
3.4 SM-FBG Sensor limits and improvements to sensor performance	59
3.5 Conclusion and Perspectives	63
References	65
Chapter 4 - Research administration	67
4.1 Introduction	67
4.2 PhD Supervision	67
4.3 Research Projects and Collaborations	69
4.4 General Perspectives and Future Work	72
4.5 Publications	74
4.5.1 Patent Application	74
4.5.2 Journal Papers	74
4.5.3 Conference Papers (Selected)	75
4.5.4 Invited Seminars	76
4.6 Administrative Duties and Service to the Community	77
4.7 Teaching Duties	77
4.8 Curriculum Vitae	78

Chapter 1 - Single-crystal fibers for sensing applications

1.1 Introduction

Most fiber optic sensing systems employ conventional glass fibers as sensing elements, which can often constrain the measurement of certain parameters of interest such as temperature, strain, stress and bending, to a lower range due to the intrinsic physical properties of glasses. These limitations, especially in the domain of fiber optic temperature sensing, have led to the search for more robust and stable systems based on other high temperature materials. Generally, most glass-based systems are limited to temperatures below ~ 700 K, with the exception of fused-silica fibers which can be used intermittently up to 1300 K. For applications where temperatures higher than 1300 K are to be measured, these “conventional” fibers cannot be used. Suitable replacements must thus be found for this important temperature region.

Single-crystal fibers (SCFs), or “whiskers” as commonly known, on the other hand possess both mechanical and optical proprieties which are unavailable in glass fibers. Although the majority of SCFs produced to date have mainly been employed in the domains of solid-state lasers and amplifiers, guided-wave non-linear optics, optical parametric devices, etc, their application in fiber sensing schemes have recently been attracting interest, particularly for metrology in hostile environments. SCFs fabricated from sapphire (Al_2O_3), yttria (Y_2O_3), yttria-stabilized zirconia ($\text{Y}_2\text{O}_3\text{-ZrO}_2$ or YSZ) and neodymium-doped yttrium aluminum garnet ($\text{Nd:Y}_3\text{Al}_5\text{O}_{12}$ or Nd:YAG) exhibit near-theoretical strength, very high melting temperature ($\geq 2000^\circ\text{C}$), very high optical damage threshold and chemical inertness.

Most early sensors were either intrinsic or extrinsic fiber Fabry-Perot interference devices for temperature and strain measurements [1,2]. The fluorescence emission, consisting of both lifetime decay and wavelength shift, of appropriately doped SCFs has also been investigated for temperature and strain dependencies. Fluorescence characteristics are attractive as they are relatively independent of power fluctuations of the pump source (usually a laser diode).

The synthesis of SCFs employed in this work is carried out by the laser heated pedestal growth technique due to its versatility. Both undoped and doped sapphire-based SCFs with lengths of 20 to more than 200 mm have been produced.

1.2 Laser-heated pedestal growth of SCFs

Laser-heated pedestal growth or LHPG is a non-contact growth method which couples homogeneity and high melting capacity from its heat source, the laser. Hence, axially symmetric heating of the source rod and large temperature gradients can easily be obtained together with little or no impurity contamination during fiber growth. As schematically illustrated in Fig. 1.1, by proportionally controlling the upward feeding speed, V_{feed} , of the source rod of diameter D into the laser focus and the pulling rate, V_{pull} , of an oriented seed crystal fiber of diameter d using mass conservation,

$$\frac{V_{pull}}{V_{feed}} = \left(\frac{D}{d} \right)^2 \quad (1.1)$$

an SCF of good optical quality can be obtained. Stable fiber growth, as shown in Fig. 1.2, is achieved via software control.

Typical pull rates are from 1–8 mm/min although an optimum reduction ratio of ~ 3 is used here [3] as larger values may result in growth instability and larger diameter fluctuations. Hence using a pull rate of 1 mm/min, SCFs with diameters ranging from 22.5–170 μm are grown.

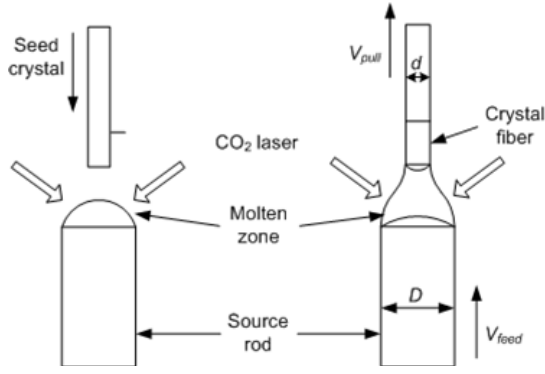


Fig. 1.1. Schematic of LHPG

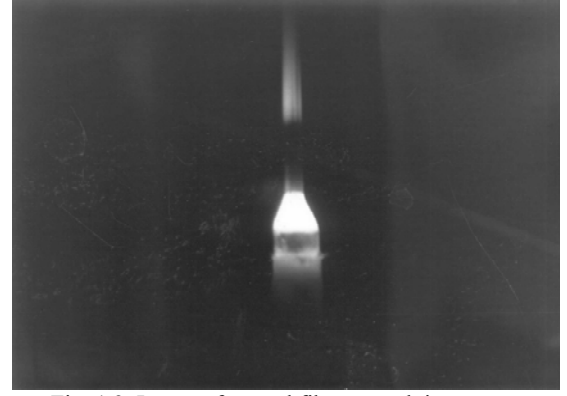


Fig. 1.2. Image of crystal fiber growth in process

The complete LHPG system is schematically illustrated in Fig. 1.3 where the heat source is a stabilized Synrad, Inc. Series 48 CO₂ laser emitting at 10.6 μm with 28W of power. A viewing system is integrated into the system to facilitate the alignment of the source rod and seed fiber and, more importantly, to monitor the molten zone from orthogonal directions.

The software control of the growth system thus ensures closed-loop control of both the pull and feed motors as well as the laser power to limit fiber diameter variations to <1%, considered sufficient for sensing applications.

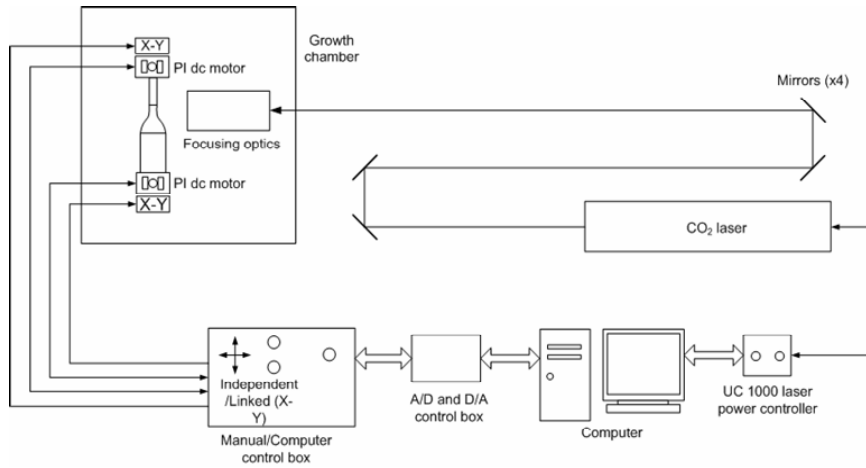


Fig. 1.3. Schematic of LHPG station

Throughout the course of this work, almost all the fibers grown are based on Al₂O₃ hosts, typical examples of which are shown in Figs. 1.4. Further, no vacuum or inert gases are required.



Fig. 1.4(a). *a*-axis
Al₂O₃ SCF



Fig. 1.4(b). *c*-axis
ruby SCF



Fig. 1.4(c).
Er³⁺+Yb³⁺: Al₂O₃
SCF

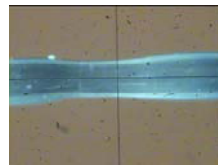


Fig. 4(d). YSZ SCF



Fig. 4(e). SCF end
taper

1.3 Ruby SCFs for fluorescence-based high temperature and strain sensing

Ruby (Cr³⁺: Al₂O₃), a precious gem stone, is also a well-known crystalline laser material which was used by Maiman to demonstrate the first successful laser operation in the pulsed mode [4]. Continuous laser emission from ruby, in fiber form, was later demonstrated by Burrus and Stone [5] with Cr³⁺ concentration as low as 0.02 wt.%. Subsequently, several studies have been carried out into the fluorescence characteristics of ruby crystals and their dependence on external physical influences, especially that of temperature [6,7] and physical deformations [8,9].

The earliest exploitation of ruby fluorescence characteristics for potential temperature sensing involved monitoring the intensity variation of the ruby R-lines (at 694.3 and 692.7 nm) and its fluorescence lifetime decay as a function of temperature [10,11]. Although the maximum temperature investigated was below 200°C, the use of phase-sensitive detection techniques or phase-locked detection (PLD) can greatly extend the maximum temperature limit [12]. Note that most temperature studies carried out to date have involved small ruby crystals cut from bulk ruby laser rods.

In this work, phase-sensitive lock-in detection and feed-back control of the excitation source modulation frequency are employed to increase the signal-to-noise ratio of the detected decay signal. The basic problem of cross-sensitivity in a ruby SCF sensor is also investigated.

1.3.1 Absorption and fluorescence spectra of ruby SCFs

Ruby is formed by incorporating Cr^{3+} ions into an Al_2O_3 host lattice at sites with a threefold axis of symmetry by substitutionally replacing the Al^{3+} ions [13,14], resulting in the Cr^{3+} ion being subjected to a trigonally-distorted octahedral crystal field which splits the $3d^3$ energy levels of the ion. The combination of a distorted field linked with an even-parity energy term and spin-orbit coupling [19] leads the lowest-lying excited ${}^2\text{E}$ state to split into the E and 2A states with an energy gap of $\sim 29 \text{ cm}^{-1}$. This manifests itself as the $\text{E} \rightarrow {}^4\text{A}_2$ transition for the R_1 line (694.3 nm) and the $2\text{A} \rightarrow {}^4\text{A}_2$ transition for the slightly weaker R_2 line (692.9 nm).

The absorption spectrum of a *c*-axis ruby fiber produced by LHPG is shown in Fig. 1.5 against that of a reference ruby rod and has been measured using unpolarized light from a stabilized Tungsten-Halogen lamp.

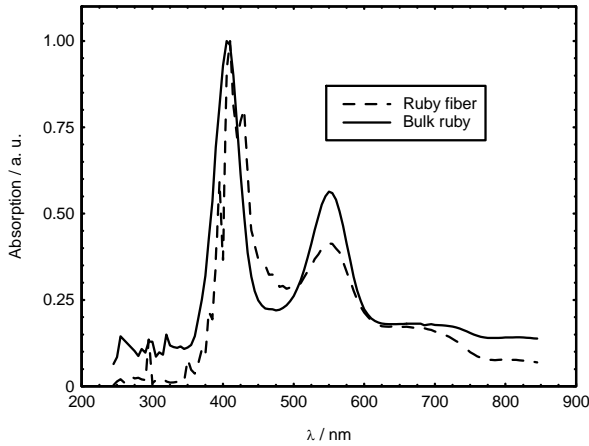


Fig. 1.5. Ruby SCF absorption spectrum compared to that of ruby laser rod

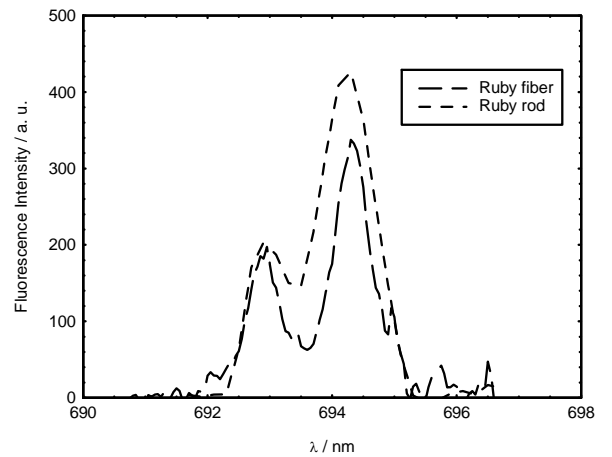


Fig. 1.6. Emission spectra from ruby SCF and its bulk counterpart

As seen, the strong interaction of Cr^{3+} ions with the sapphire crystal field leads to a wide absorption spectrum in the fiber, ranging from $\sim 350 \text{ nm}$ to $\sim 700 \text{ nm}$, with two absorption peaks centered at approximately 410 nm and 550 nm. The fluorescence emission from the same fiber, excited using a 514.5 nm *Spectra Physics 2060-10S* Ar^+ ion laser, is shown in Fig. 1.6. Two sharp R-lines typical of ruby (R_1 at 694.3 nm and R_2 at 692.9 nm) are emitted, corresponding to that of the ruby laser rod.

1.3.2 Temperature dependence of ruby SCF fluorescence

1.3.2.1 Lifetime decay

The temperature-dependent fluorescence lifetime decay from both the radiative ${}^2E \rightarrow {}^4A_2$ and nonradiative ${}^4T_2 \rightarrow {}^4A_2$ transitions in ruby fibers can be predicted using a simplified configurational coordinate (SCC) model, as illustrated in Fig. 1.7.

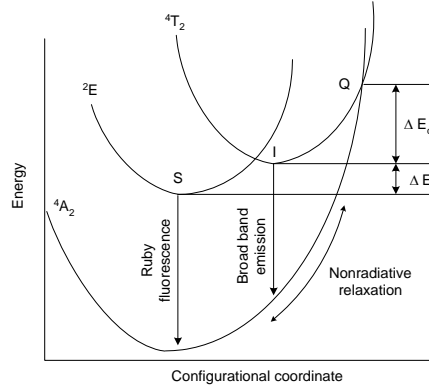


Fig. 1.7. Simplified configurational coordinate (SCC) model for Cr^{3+} interactions in ionic crystal hosts

Then, assuming a quasi-thermodynamic equilibrium in the 4T_2 and 2E states, the rate change in their total population can be given by

$$\frac{dn}{dt} = - \frac{1/\tau_s + (1/\tau_i)e^{-\Delta E/kT} + (1/\tau_q)e^{-(\Delta E_q + \Delta E)/kT}}{1 + 3e^{-\Delta E/kT}} \quad (1.2)$$

where τ_q is the nonradiative decay rate (or thermal quenching rate) and ΔE_q the energy gap between the 4T_2 and 4A_2 states. ΔE , k and T represent the energy gap between 4T_2 and 2E , Boltzman's constant and temperature, respectively, τ_s and τ_i being the lifetimes of 2E and 4T_2 . By integrating (1.2), the fluorescence lifetime, τ , can be found as

$$\tau = \tau_s \frac{1 + 3e^{-\Delta E/kT}}{1 + \alpha e^{-\Delta E/kT} + \beta e^{-(\Delta E_q + \Delta E)/kT}} \quad (1.3)$$

with $\alpha = \tau_s/\tau_i$ and $\beta = \tau_s/\tau_q$. Thus with an appropriate choice of fit parameters, relatively good accuracy can be obtained when predicting the fluorescence lifetime for temperature sensing applications [7].

The experimental set-up for monitoring the temperature-induced fluorescence lifetime variation is illustrated in Fig. 1.8. The ruby SCF employed (Cr^{3+} concentration ~ 0.1 wt.%) has a nominal diameter of $\sim 167 \mu\text{m}$ (maximum variation $< 2\%$) and a total length of ~ 75 mm. One end is tapered for better reflection of the fluorescence signal. A $200 \mu\text{m}$ core silica fiber (*Thorlabs FVP-200-PF*) is used to transmit the chopped excitation beam from an Ar^+ laser to the target ruby SCF, both of which are butt-coupled together in a tapered silica capillary (see inset) and then secured together by high-temperature ceramic adhesives (*Fortafix AL/CS*). The reflected fluorescence signal is next directed to a 10 MHz *Hamamatsu C5460* avalanche photodiode (APD) after the fiber coupler. Further, a narrow bandpass optical interference filter centered at 694 nm (FWHM ± 2 nm) placed in front of the APD separates the desired fluorescence signal from the excitation source. A high-speed (100 MHz) *FEMTO* voltage amplifier is used to match signal levels to be coupled into a 500 MHz *HP* digitizing oscilloscope.

Preliminary tests performed to characterize the bandwidth of the entire detection circuit without the ruby fiber using a squarewave-modulated signal from the Ar^+ laser result in a curve-fitted lifetime of $\tau_{\text{system}} \sim 7.4 \mu\text{s}$, which is also taken as the measurement limit in this experiment. For temperature characterization, the ruby SCF is inserted into the middle of a *CARBOLITE Eurotherm* furnace (quoted stability ± 1 K and maximum temperature 1473 K) while high-temperature ceramic wool is used to plug both ends of the heating chamber to maintain a stabilized temperature at the set level and to hold the sensor probe so that no contact occurs

between the fiber and the internal furnace wall. A type “K” thermocouple is also inserted into the heating chamber to serve as reference.

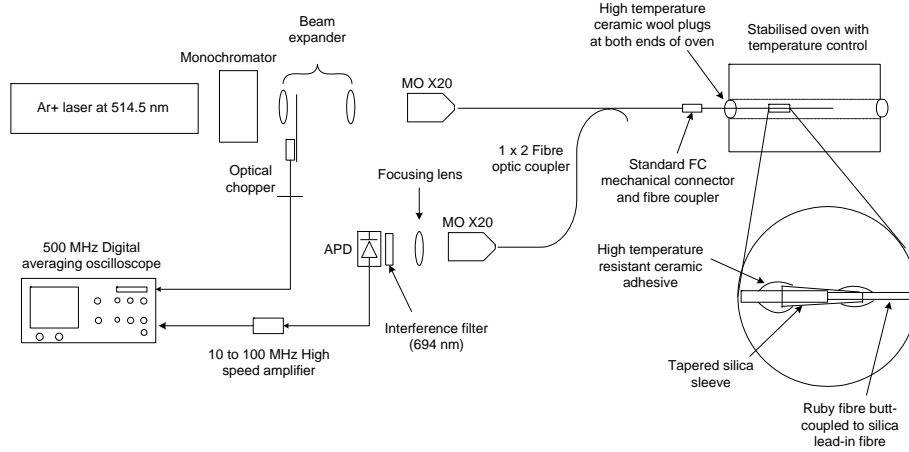


Fig. 1.8. Experimental set-up for ruby SCF fluorescence lifetime measurement as a function of temperature

The least-squares curve-fitting technique is used to determine the averaged fluorescence lifetime of the sensor taken at 50 K intervals via the following expression

$$I(t) = I_0 e^{(-t/\tau)} + C \quad (1.4)$$

where $I(t)$ is the decaying fluorescence intensity at time t , I_0 the intensity at $t=0$, τ the lifetime decay and C a constant due to any dc offset in the detected signal. Figure 1.9 illustrates the lifetime decay of the ruby SCF at room temperature (292 K) together with the curve-fitting statistics: r^2 indicates the confidence and σ_τ the standard deviation of the curve-fitting achieved.

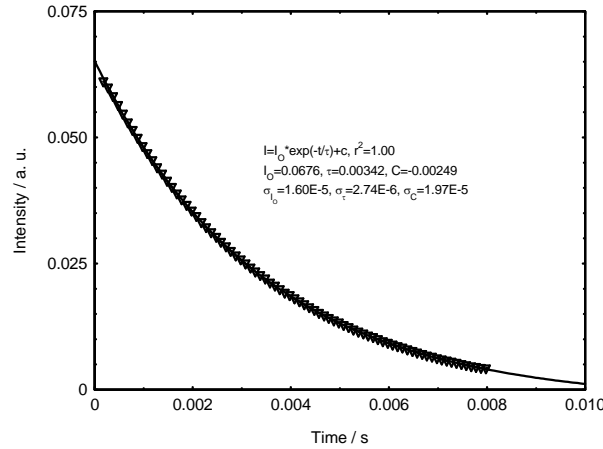


Fig. 1.9. Fluorescence lifetime decay of ruby SCF at 292 K

Very good fits have been achieved up to 773 K where the r^2 parameter is $\sim 100\%$. Further, σ_τ is found to be significantly low at $\sim 0.5 \mu\text{s}$ and the error associated with this deviation is $\sim 0.32\%$. The curve-fitting accuracy beyond this temperature is then affected by the low intensity of the decay signal. The maximum deviation of the lifetime limited the resolution of temperature measurements and is also the resolution limit of the sensor system. This is found to be $\sim 4.6\%$ at 923 K, translating into an error of ~ 40 K. The average precision from 292 K to 773 K is ~ 2.4 K. Below 673 K, a precision of better than 1 K is obtained. Hence, temperature changes of less than 1 K can be accurately detected, implying the possibility of high-resolution measurement coupled to effective and simple detection and signal processing. The SCC model in (1.3) is next used to fit the experimental lifetime data as a function of temperature in Table I.

The fitted curve for temperatures up to 923 K is shown in Fig. 1.10, demonstrating the good coherence of the experimental data to the SCC model except at high temperatures, where,

due to the low signal intensities, relatively large errors are committed. An approximation of the sensitivity of the model is shown in Fig. 1.11, where the sensitivity curve is observed to increase to a negative maximum at ~400 K before decreasing again rapidly to a minimum at 923 K.

Table I
Fitted parameters for the SCC model.

τ_s / ms	ΔE / cm^{-1}	α	β	ΔE_q / cm^{-1}
3.617	1637.4	197.6	2.818×10^6	4888.26

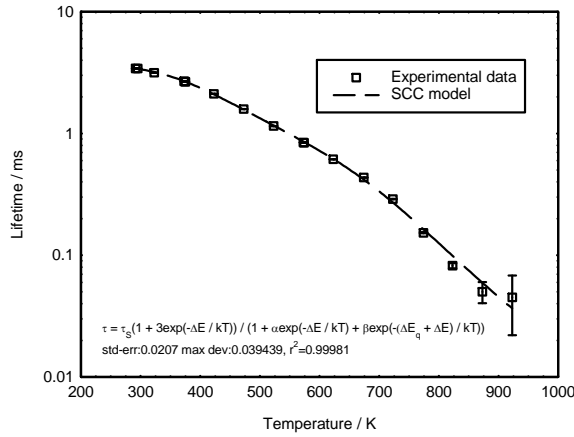


Fig. 1.10. Curve-fitting using SCC model for 292 K to 923 K

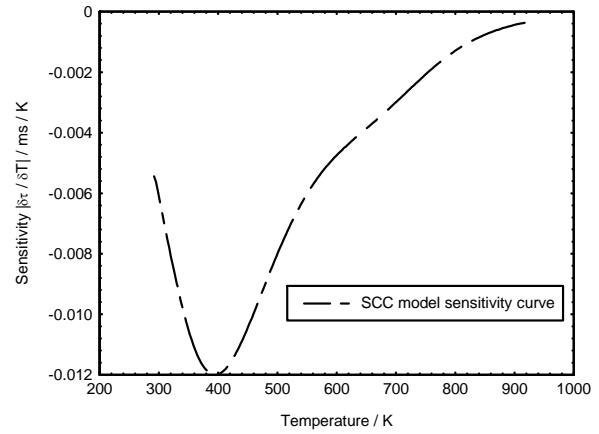


Fig. 1.11. Calculated sensitivity curve for SCC model

The SCC model also enables accurate comparison of the fluorescence lifetime characteristics of the ruby SCFs with theory, taking into consideration the rapid nonradiative transition and thermal quenching rates within a relatively large temperature range. Hence, relatively long lifetimes (~2–3 ms) are measured at low temperatures while beyond 600 K, when nonradiative transition and thermal quenching become dominant, the fluorescence lifetime falls rapidly below 1 ms, resulting in increasing errors being obtained. These errors limit the resolution and accuracy achievable when employing the SCC model as a calibration curve. However, comparison with published data [7,15] shows that reasonably good agreement has been achieved for predicting temperature-induced lifetime decay.

It is seen that the lifetime decays monotonically with temperature and no ambiguities at different temperatures are observed. At ~673 K, the beginning of a change in the gradient of the lifetime-temperature curve is also observed as well as large discrepancies beyond 823 K. Moreover, the flattening of the lifetime between 873 K and 923 K occurs very close to the detectable limit of the sensing system, resulting in considerable inaccuracies and, thus, large errors at these two temperatures (1.98 % and 4.62 %, respectively). Another important factor contributing to this disparity is the choice of the optical filter used. Centered at 694 nm, corresponding to the ruby peak fluorescence wavelength, the ± 2 nm FWHM bandwidth isolates the sideband phonon energies associated with ruby emission characteristics which are highly temperature-dependent. Hence, the sensitivity curve (Fig. 1.11) reflects a sensitivity amplitude reaching a maximum value at ~673 K, followed by a decrease towards the minimum with increasing temperature. On the other hand, the negative sensitivity is due to the drop in the lifetime rate with temperature.

1.3.2.2 R-line shifts

Another fluorescence characteristic which is affected when ruby is subjected to elevated temperature is the spectral shift in the R-lines. Both empirical and theoretical models have been employed to fit the R_1 and R_2 lines with relatively good results and accuracy over a limited

temperature range [16-18]. However, the R-line shifts may not vary constantly or uniformly with temperature. It is thus highly possible that beyond a certain temperature the R_1 and R_2 lines overlap and it would then be almost impossible to distinguish one from the other. One way to overcome this is to use a double-Lorentzian line shape, a Voigt profile which is a combination of Gaussian and Lorentzian lineshapes or a simple cubic model to describe the characteristic fluorescence curve of ruby. Further, since the two R-lines do not shift together exactly, a double-Lorentzian line shape could be useful to overcome the overlapping of these two lines at high temperatures (~ 450 K). The general cubic equation adopted here is based on the double Lorentzian lineshape, given by

$$R_i(T) = \alpha + \beta T + \delta T^2 + \gamma T^3 \quad (1.5)$$

where $R_i(T)$ represents either the R_1 or R_2 line being studied in units of cm^{-1} , α , β , δ and γ the fit parameters (constants).

For consistency, the same ruby SCF used for lifetime measurements is employed here. The experimental set-up differs from the previous experiment by replacing the detection system with a monochromator. The reflected fluorescence signal is focused onto the entrance slit of a $\frac{1}{2}$ m *DIGIKRÖM DK480* monochromator. Signal detection is assured by a conventional Si PIN photodiode at the output slit of the monochromator and connected to a *Sci-Tech* lock-in amplifier to increase the signal-to-noise ratio of the measurement system. Lock-in amplification also enables very stable detection of the desired signal during monochromator scanning (from 690 to 697 nm) at ~ 0.02 nm steps. A dedicated computer program written in LabView coordinates the monochromator scanning rate and data acquisition. The experimental repeatability falls within the 0.02 nm specified by the scanning steps, except at very high temperatures where the inherent noise from the ruby fluorescence becomes relatively high.

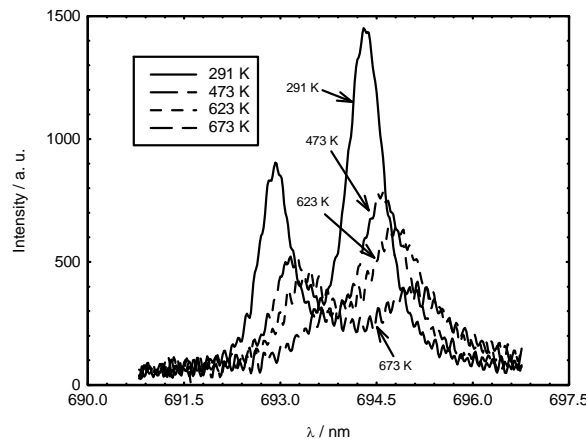


Fig. 1.12. Fluorescence spectra of ruby SCF at 4 different temperatures

The shifts of the two R-lines with temperature are plotted in Fig. 1.12 and Fig. 1.13 where a sliding data window of ~ 0.4 nm is employed to smooth the high frequency fluctuations observed in order to improve peak detection. The error, obtained by comparing measured and smoothed peak values, is within the 0.03 nm imposed by the monochromator resolution, hence, the resulting data may be taken as having an accuracy of this value. The shifts in both lines are linear and almost uniform up to ~ 623 K beyond which they are seen to diverge, with R_2 shifting more than R_1 . The red shift of R_2 is also more obvious and increases more significantly beyond ~ 623 K to 823 K, where it overlaps with the main body of the fiber fluorescence.

At 823 K, only R_1 is clearly distinguishable, as shown in Fig. 1.14. The maximum temperature investigated is ~ 973 K, at which point the useful signal is lost in background noise. Further, a relatively large increase can be seen from ~ 623 K. There are therefore two temperature regions where the R-line shifts are linear, separated by a sharp but significant increase from 623 to 673 K (Fig. 1.13) which represents an almost doubling of the shifts for both R-lines.

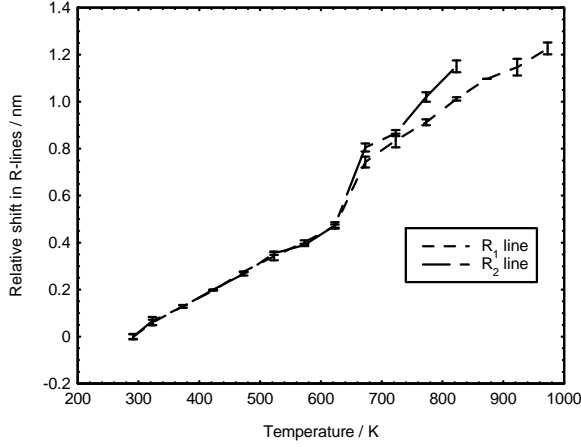


Fig. 1.13. Relative R_1 and R_2 shifts with temperature

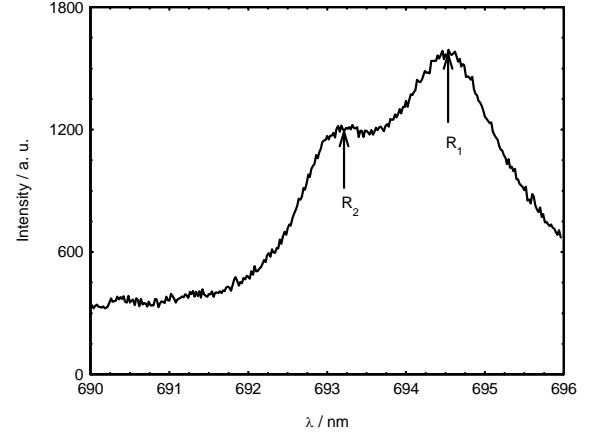


Fig. 1.14. Ruby SCF spectrum at 823 K

Two sets of cubic calibration curves based on (1.5) are used to predict the wavelength shifts of the ruby SCF for temperatures up to 623 K (350 °C). The fitted values obtained are respectively $\alpha = 693.74$ nm, $\beta = 0.0023464$ nm K⁻¹, $\delta = -1.5802 \times 10^{-6}$ nm K⁻² and $\gamma = 7.6748 \times 10^{-10}$ nm K⁻³ for the R_1 line; and 692.29 nm, 0.0027091 nm K⁻¹, -2.498×10^{-6} nm K⁻² and 1.4853×10^{-9} nm K⁻³ for R_2 . Neglecting the sharp rise in lineshifts between 623 and 673 K, the calibration of the R-lines from 673 K to 973 K and 823 K, respectively for R_1 and R_2 , results in $\alpha = 694.25$ nm, $\beta = -3.3161 \times 10^{-4}$ nm K⁻¹, $\delta = 3.7492 \times 10^{-6}$ nm K⁻² and $\gamma = -1.8444 \times 10^{-9}$ nm K⁻³ for R_1 . For R_2 , where the largest error occur at the maximum of 823 K, the fitted values of α , β , δ and γ are respectively 695.33 nm, -0.005613 nm K⁻¹, 3.9402×10^{-6} nm K⁻² and 1.2679×10^{-9} nm K⁻³. The measured and calculated values of the lineshifts are plotted in Figs. 1.15(a) and 1.15(b), showing relatively good agreements. The maximum red shift of the R-lines is ~ 1.23 nm for R_1 .

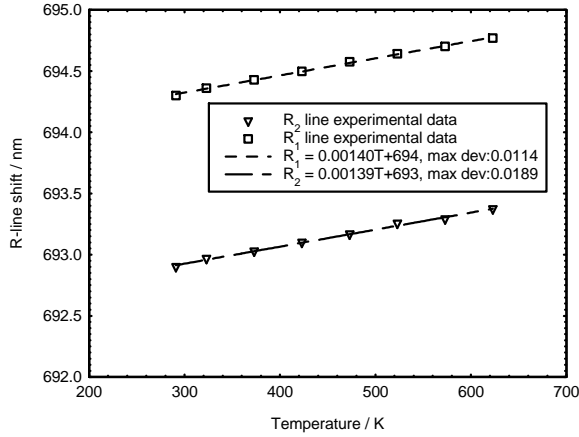


Fig. 1.15(a). Wavelength coefficient of linear fit (291-623 K).

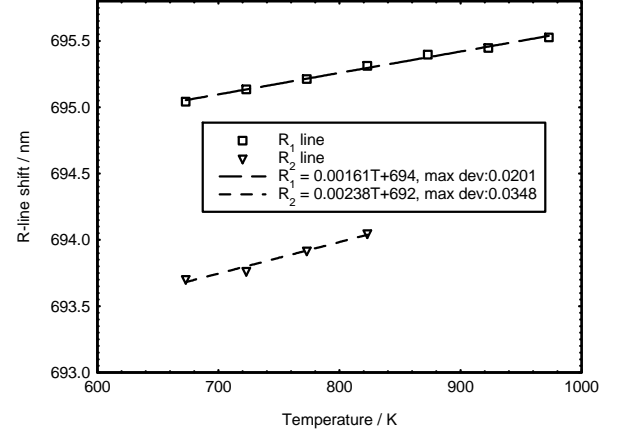


Fig. 1.15(b). Wavelength coefficient of linear fit (673-923 K).

The temperature-induced shifts of the c -axis ruby fiber have been monitored up to 973 K for the stronger R_1 line and 823 K for the R_2 line. However, a single continuous fit cannot be used to describe the wavelength coefficient. Hence, the separate temperature regions have been investigated by employing two simple calibration curves based on [17]. The doubling of the wavelength shift has not been reported anywhere in published literature, hence, the causes are still unknown. The only parameters which have been changed are the laser power and the sensitivity of the lock-in amplifier used. At room temperature, no observable changes in the position of the R-line have been detected by changing the laser power, while increasing the lock-in amplifier's sensitivity by one setting only increases the intensity detected by a factor of 3. However, the large increase in the temperature-induced lineshifts can be attributed to the domination of the nonradiative decay from the 4T_2 state due to thermal quenching as

demonstrated by the beginning of a sudden change in gradient in the decay lifetime at ~ 673 K [19].

1.3.3 Strain dependence of ruby SCF fluorescence

The fluorescence characteristics of ruby can also be influenced by stresses applied due to high pressure or shockwave loading to its a - or c -crystallographic plane. The excited state splitting (Δ) of the lowest excited 2E state due to stress is dependent on the diagonal trigonal crystal field parameter, v , which is strongly dependent on the immediate surrounding of the chromium ion, Cr^{3+} [20]. The $\alpha\text{-Al}_2\text{O}_3$ host lattice is trigonally symmetric and the Cr^{3+} ions substituting for the Al^{3+} ions alter the energy-level structure of the otherwise free Cr^{3+} ions [21]. When unstressed, the level splittings of the Cr^{3+} ions in Al_2O_3 form the sharp R-lines characteristic of ruby fluorescence. However, applied stresses can change the trigonal field but not the symmetry of the host lattice, thus leading to variations of the energy level splittings which manifest as R-line shifts under very high isotropic pressure or compressive stress.

The use of ruby R-lines for precision pressure measurement in a diamond anvil cell (DAC) has been performed using a piece of ruby crystal with ~ 0.05 wt.% Cr^{3+} up to a maximum pressure of 40 kbar [10]. The R-lines have been found to shift linearly with the applied pressure, with the R_1 -shift being of the order of ~ -0.77 $\text{cm}^{-1}/\text{kbar}$ and that of R_2 being ~ -0.84 $\text{cm}^{-1}/\text{kbar}$. Nevertheless, no line broadening has been observed but under non-hydrostatic conditions (such as shockwave loading) line broadening could occur [9,18].

1.3.3.1 Lifetime decay

The strain-based experimental set-up is shown in Fig. 1.16 where a straining device with a 1 μm resolution micrometer head is now used to induce uniaxial strains in the ruby SCF. The fiber is attached to the movable and fixed translation stages with strong adhesives (*Permabond F241* + Hardener no. 1) and secured co-linearly with the longitudinal axis of the strain-inducing device.

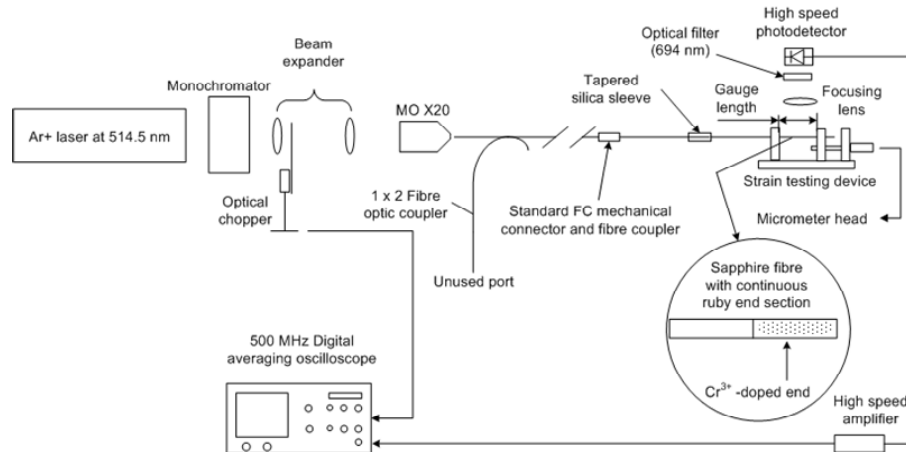


Fig. 1.16. Experimental schematic for ruby SCF fluorescence lifetime strain sensing.

The reflected fluorescence decay signal, which is too weak to be detected in the reflection mode, is here detected directly along the ruby SCF length. A narrow bandpass optical filter placed in front of the high-speed Si detector filters all undesired light. The excitation beam is modulated via an optical chopper and data averaging performed with the 500 MHz oscilloscope. The ruby SCF is oriented along the c -axis with one section grown as sapphire while the gauge end of ~ 12.33 mm is Cr^{3+} -doped (see inset in Fig. 1.16).

The ruby fiber is uniaxially strained at 5 μm steps up to a maximum extension of $\delta L \sim 100$ μm , equivalent to $\varepsilon (= \delta L/L) \sim 8110$ μe . The lifetime decay of the ruby SCF at 0 μe (or $\delta L = 0$

$\mu\epsilon$) is 3.43 ms, as shown in Fig. 1.17 while that at 8110 $\mu\epsilon$ is found to be ~ 3.44 ms (Fig. 1.18). The fitting confidence, r^2 , is better than 0.998 at each strain level. Over the monitored strain range, no observable change in the decay rate is thus detected. The strain experiment is repeated to verify that no slippage from either the bonding adhesives or the mechanical parts has occurred. The ruby SCF is subsequently tested to destruction at $\sim 33500 \mu\epsilon$.

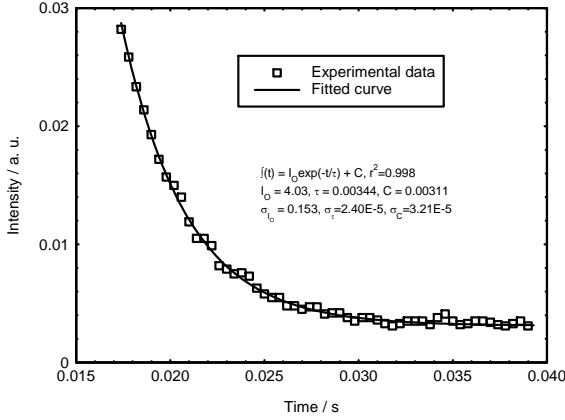


Fig. 1.17. Fitted lifetime decay at $\epsilon = 0 \mu\epsilon$.

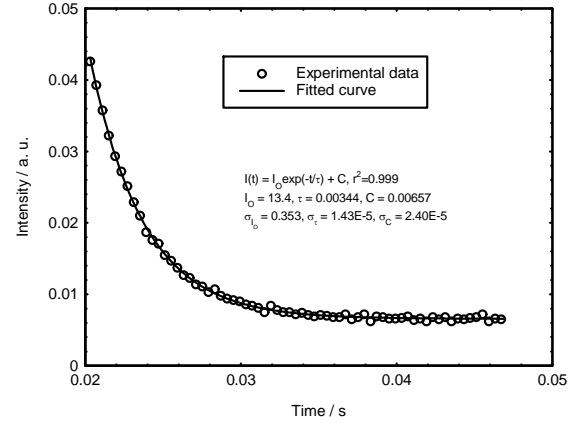


Fig. 1.18. Fitted lifetime decay at $\epsilon = 8110 \mu\epsilon$.

The fluorescence lifetime decay of the ruby SCF under uniaxial strain loading up to 8110 $\mu\epsilon$ is plotted in Fig. 1.19, the error bars representing the standard deviation. The lifetime is seen to fluctuate between 3.42 and 3.54 ms and is considered as being insensitive to strain influence. Both the temperature and strain influences on the lifetime decay plotted in Fig. 1.20 indicate the relative insensitivity of the lifetime to applied strains. This thus eliminates the problem of cross-sensitivity to strains during temperature measurement [22].

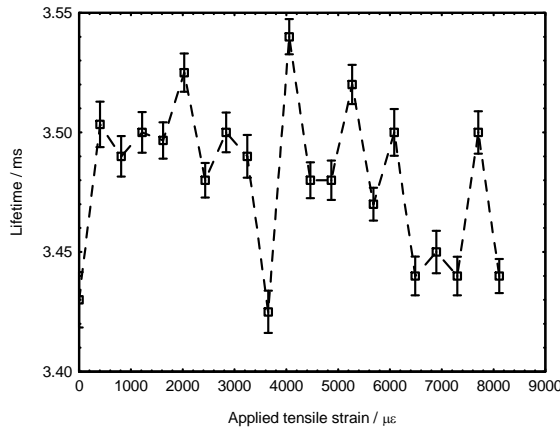


Fig. 1.19. Ruby SCF fluorescence lifetime decay versus uniaxial tensile strain.

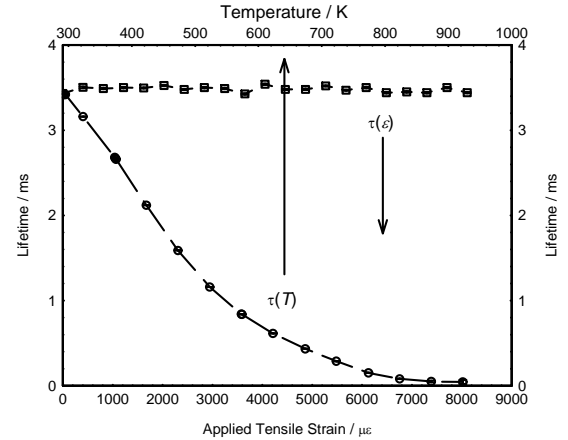


Fig. 1.20. Strain and temperature dependences of ruby SCF fluorescence lifetime.

1.3.3.2 R-line shifts

The R-line dependence on strain is investigated for the ruby SCF tested above (i.e. before its destruction) as illustrated in Fig. 1.21 with a scan step of 0.05 nm. Also, a 0.4 nm sliding average digital smoothing is employed to localize the curve peaks. Lock-in techniques and computer control enable the R-line shifts to be monitored from 0 to 33500 $\mu\epsilon$, beyond which the ruby SCF fractures. The elongation prior to fiber failure is $\sim 240 \mu\text{m}$ while the gauge length in this experiment is $\sim 6 \text{ mm}$ thus giving a breaking strain of $\sim 40100 \mu\epsilon$.

Each spectrum is averaged over a minimum of 6 scans at each applied strain. At 0 $\mu\epsilon$, the R-lines are respectively 694.3 nm and 692.9 nm. The relative shifts of the two R-lines with uniaxial strain are plotted in Fig. 1.22 showing no significant shifts for both R_1 and R_2 . Both R-

lines demonstrate a very low strain coefficient with $\sim -3.62 \times 10^{-6} \text{ nm}/\mu\epsilon$ for R_1 while for R_2 , it is $\sim -3.64 \times 10^{-6} \text{ nm}/\mu\epsilon$.

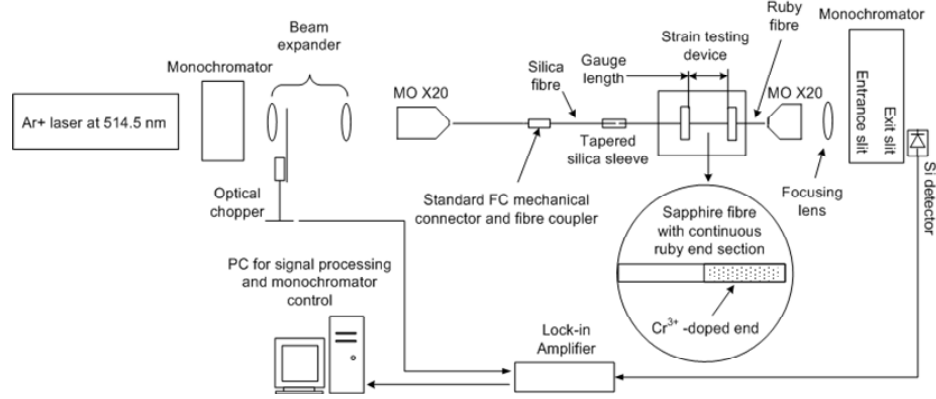


Fig. 1.21. Experimental set-up for R-line shift measurements in transmission mode.

It is of importance to note that the maximum permissible strain which can be applied before any degradation of the *F241* adhesive is $\sim 250000 \mu\epsilon$. The ruby SCF suffers brittle fracture at $\delta L \sim 240 \mu\text{m}$ for a gauge length of $\sim 6 \text{ mm}$ implying a strain limit $\sim 40100 \mu\epsilon$. This is more than 5 times less than that of the adhesive used hence, it can be safely assumed that the fiber broke due principally to the physical extension applied. The ruby lineshifts under tensile straining is even smaller than those under temperature effects, considering the relative insensitivity of the lifetime decay rates to strain. The negative gradients in Fig. 1.22 indicate a minute shift towards the blue. Unlike the red shifts observed when subjected to increasing temperature, straining of the ruby fiber actually shifts the R-line peaks towards the higher energy regions.

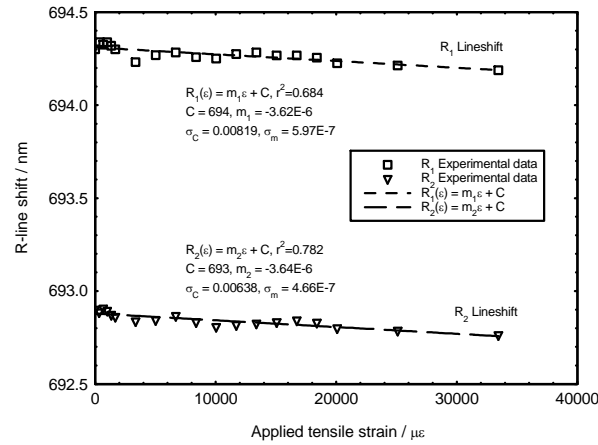


Fig. 1.22. R-line shifts as a function of uniaxial tensile strain.

1.4 Conclusions and Perspectives

Fiber optic sensors based on doped sapphire (Al_2O_3) single-crystal fibers (SCFs) have been developed in this PhD work for metrology in very harsh environments. The interest in these crystal fibers is due in particular to their properties: chemical inertness, very high strength, high mechanical resistance to abrasion, very high melting point ($>2000^\circ\text{C}$), wide optical transparency ($\sim 0.15\text{--}5 \mu\text{m}$), etc. These SCFs are produced by the laser-heated pedestal growth (LHPG) technique with relatively good optical quality.

Ruby SCFs have been demonstrated for temperature sensing by exploiting their unique response: their fluorescence spectra in terms of lifetime decay as well as R-line shifts. Its fluorescence lifetime decay is characteristic of the spectral response to temperature and, since it

is wavelength-coded, has the unique advantage of being relatively independent of the pump power fluctuation. Further, no parasitic fluorescence decay is detected since ruby emits uniquely in the 692–694 nm region away from the pump source (~480 nm). Both the fluorescence lifetime and R-line shifts have been investigated up to 923 K (or 650°C) and 973 K (700°C) respectively with a relatively good precision before extinction of the emitted signal. Further, in both investigations, no hysteresis has been detected, demonstrating the robustness of this technique. Both fluorescence characteristics are also tested for their strain-induced response up to the fracture point and have been found to be relatively insensitive to tensile stress. The principal ambition to design a sensor system which is uniquely sensitive to a single physical parameter is therefore achieved. Nevertheless, a major inconvenience with these fibers is their high transmission losses since SCFs typically have no optical cladding and are hence multimode devices. Further, due to their crystalline structure, they are difficult to couple to conventional glass fibers, in particular via fusion splicing. The majority of the work on these fibers involves their butt coupling to glass fibers for transmission purposes. The technical challenge is therefore to implant a cladding layer either by re-growing an already-doped SCF or by using sol-gel techniques to obtain a compatible cladding material which is at the same time suitable for the targeted applications.

Although not described in this manuscript, Er^{3+} and Yb^{3+} co-doped Al_2O_3 crystal fibers have been investigated for high temperature sensing up to 1423 K (~1150°C) with a precision better than 5 K over the entire dynamic range [23]. However, most importantly, simultaneous fluorescence and upconversion processes over the 1540 nm and the visible green and red regions, respectively, have been observed from rare-earth-doped SCFs produced by LHPG. Their emission spectra correspond to the major laser devices in use for emission in the visible (blue, red and green) as well as in the telecommunications sector [24-27]. Although employed for metrological applications here, further investigation of these devices could be highly worth pursuing in the context of solid-state amplifiers with an intrinsic fiber geometry. However, like ruby fibers, these RE-doped SCFs exhibit large optical losses and the sensing probes produced have to be reliably coupled to glass fibers for remote sensing.

Potential applications for these SCFs are in the aeronautics, turbo-machine and petrochemical sectors where harsh sensing environments are frequently encountered. Towards the end of my PhD research, discussions were in progress with Rolls-Royce Plc (UK) to employ these sensors for high-temperature mapping of turbine engines. Further work was also launched at the same time to investigate the use of sol-gel techniques for developing compatible cladding layers to be applied on such fibers. This PhD research was funded by an EPSRC grant of 50 k£.

References

- [1] A. Wang, G. Z. Wang, S. Gollapudi, R. G. May, K. A. Murphy and R. O. Claus, Advances in sapphire optical fiber sensors, Fiber optic smart structures and skins V, Proc. SPIE, vol. 1798, pp. 56-65, 1992
- [2] A. Wang, S. Gollapudi, R. G. May, K. A. Murphy and R. O. Claus, Sapphire optical fiber-based interferometer for high temperature environmental applications, Smart Mater. Struct., vol. 4, pp. 147-151, 1995
- [3] M. M. Fejer, J. L. Nightingale, G. A. Magel and R. L. Byer, Laser-heated pedestal growth apparatus for single-crystal optical fibers, Rev. Sci. Instrum., vol. 55, no. 11, pp. 1791-1796, 1984
- [4] T. H. Maiman, Stimulated optical radiation in ruby, Nature, vol. 187, pp. 493-494, 1960
- [5] C. A. Burrus and J. Stone, Room-temperature continuous operation of a ruby fiber laser, J. Appl. Phys., vol. 49, no. 6, pp. 3118-3123, 1978
- [6] W. H. Fonger and C. W. Struck, Temperature dependences of Cr^{3+} radiative and nonradiative transitions in ruby and emerald, Phys. Rev. B, vol. 11, no. 9, pp. 3251-3260, 1975
- [7] Z. Zhang, K. T. V. Grattan and A. W. Palmer, Temperature dependences of fluorescence lifetimes in Cr^{3+} -doped insulating crystals, Phys. Rev. B, vol. 48, no. 11, pp. 7772-7778, 1993
- [8] R. A. Forman, G. J. Piermarini, J. D. Barnett and S. Block, Pressure measurement made by the utilization of ruby sharp-line luminescence, Science, vol. 176, pp. 284-285, 1972
- [9] X. A. Shen and Y. M. Gupta, Effect of crystal orientation on ruby R-line shifts under shock compression and tension, Phys. Rev. B, vol. 48, no. 5, pp. 2929-2940, 1993
- [10] K. T. V. Grattan, R. K. Selli and A. W. Palmer, Ruby fluorescence wavelength division fiber-optic temperature sensor, Rev. Sci. Instrum., vol. 58, no. 7, pp. 1231-1234, 1987
- [11] R. R. Sholes and J. G. Small, Fluorescent decay thermometer with biological applications, Rev. Sci. Instrum., vol. 51, no. 7, pp. 882-884, 1980
- [12] Z. Zhang, K. T. V. Grattan and A. W. Palmer, A novel signal processing scheme for a fluorescence based fiber-optic temperature sensor, Rev. Sci. Instrum., vol. 62, no. 7, pp. 1735-1742, 1991
- [13] J. Friedel, Transition metals: Electronic structure of the d-band. Its role in the crystalline and magnetic structures in: The Physics Of Metals. 1. Electrons, J. M. Ziman (Ed.), Cambridge University Press, Cambridge, p. 340, 1969
- [14] V. Evtuhov and J. K. Neeland, Pulsed ruby lasers in: Lasers, vol. 1, A. K. Levine (Ed.), Edward Arnold Ltd., London, P. 1, 1966
- [15] K. T. V. Grattan and Z. Y. Zhang, Temperature dependences of Cr^{3+} fluorescence lifetimes in: Fiber Optic Fluorescence Thermometry, K. T. V. Grattan and A. Augousti (Eds.), Chapman and Hall, Suffolk, p. 35, 1995
- [16] D. E. McCumber and M. D. Sturge, Linewidth and temperature shift of the R lines in ruby, J. Appl. Phys., vol. 34, no. 6, pp. 1682-1684, 1963
- [17] D. D. Ragan, R. Gustavsen and D. Schiferl, Calibration of the ruby R_1 and R_2 fluorescence shifts as a function of temperature from 0 to 600 K, J. Appl. Phys., vol. 72, no. 12, pp. 5539-5544, 1992
- [18] R. G. Munro, G. J. Piermarini, S. Block and W. B. Holzapfel, Model line-shape analysis for the ruby R lines used for pressure measurement, J. Appl. Phys., vol. 57, no. 2, pp. 165-169, 1985
- [19] J. H. Sharp, H. C. Seat, Z. Y. Zhang and K. T. V. Grattan, Single-crystal ruby fiber temperature sensor, Sensors Actuator A, vol. 101, pp. 24-29, 2002
- [20] R. M. Macfarlane, Stress-induced trigonal crystal-field parameters in some oxide lattices, Phys. Rev., vol. 158, no. 2, pp. 252-255, 1967
- [21] D. E. Rimmer and D. F. Johnston, A study of the origin of the trigonal crystal field in ruby. I. Analysis of experimental data, Proc. Phys. Soc., vol. 89, pp. 943-952, 1966
- [22] H. C. Seat and J. H. Sharp, Dedicated temperature sensing with c-axis oriented single-crystal ruby ($\text{Cr}^{3+}:\text{Al}_2\text{O}_3$) fibers: Temperature and strain dependences of R-Line fluorescence, IEEE Trans. Instrum. Meas. (Special Joint Issue with J. Lightwave Technol.), vol. 53, no. 1, pp. 140-154, 2004
- [23] H. C. Seat and J. H. Sharp, $\text{Er}^{3+}+\text{Yb}^{3+}$ -codoped Al_2O_3 crystal fibres for high temperature sensing, Meas. Sci. Technol., vol. 14, pp. 279-285, 2003
- [24] M. J. F. Digonnet (Ed.), Rare Earth Doped Fiber Lasers and Amplifiers, Marcel Dekker, New York, 1993
- [25] G. N. van den Hoven, E. Snoeks, A. Polman, J. W. M. van Uffelen, V. S. Oei and M. K. Smit, Photoluminescence characterization of Er-implanted Al_2O_3 films, Appl. Phys. Lett., vol. 62, no. 24, pp. 3065-3067, 1993
- [26] R. Serna, M. Jiménez de Castro, J. A. Chaos, C. N. Afonso and I. Vickridge, The role of Er^{3+} - Er^{3+} separation on the luminescence of Er-doped Al_2O_3 films prepared by pulsed laser deposition, Appl. Phys. Lett., vol. 75, no. 26, pp. 4073-4075, 1999
- [27] R. Scheps, Upconversion laser processes, Prog. Quant. Electron., vol. 20, no. 4, pp. 271-358, 1996

Chapter 2 - Polarization-based and dual-modulation fiber Fabry-Perot interferometry

2.1 Introduction

This first half of this chapter describes the development of an all-optical dual-cavity extrinsic fiber Fabry-Perot interferometer (EFFPI) based on polarization decomposition of the fundamental mode for periodic and non-periodic vibration measurements (PhD thesis, Dr. S. Pullteap, 2004–2008 [1]). The second half concerns the evolution of the dual-cavity EFFPI into a modulation-based EFFPI which has been developed into an instrument for slowly-varying and quasi-static displacement measurements with specific focus on applications to geophysics.

Knowledge of the three important parameters, namely, vibration amplitude, velocity and acceleration, associated with mechanical vibration can be usefully exploited to characterize and analyze the complete behaviour of important machinery. Vibration also plays a major role in various domains and its influences can have potentially dire consequences particularly in the aeronautics and aerospace industry, in civil engineering, manufacturing, precision mechatronics applications, as well as in the continuously-evolving microelectronics sector [2,3]. Vibration analysis not only allows the performance limits of an engineering component to be determined but can also be employed for fatigue or damage detection so that preventive maintenance can be carried out before the occurrence of critical failure. In geophysics, fiber interferometers are particularly well-adapted for monitoring seismic and volcanic activities, earth strains as well as exploration of petroleum and other natural resources [4].

Fiber optic interferometers (FOIs) exploit the effects of beating between a reference optical wave and a sensing wave modulated by a physical parameter to result in a series of cosinusoidal fringes that can be detected by a suitable photodetector. The difference in the optical path lengths traversed by the two waves then induces an optical phase difference, $\Delta\phi$, which can then be interpreted using [5]

$$\Delta\phi = \frac{2\pi(\Delta nd)}{\lambda} = (n_1d_1 - n_2d_2)\frac{2\pi}{\lambda} \quad (2.1)$$

with n_1d_1 and n_2d_2 the optical path lengths, n_1 and n_2 being the refractive indices of the respective medium, and λ the wavelength of the optical source used.

The fiber-based Fabry-Perot interferometer (FFPI) is a versatile multiple-beam device which has undergone intense development only since the early 1980s [6-8]. Interference is generated from the reference and sensing beams propagating within a single fiber arm [9]. As schematically shown in Fig. 2.1, an incident beam, I_i , is injected into the interferometric cavity at an arbitrary angle. A small percentage is back-reflected as the reference beam at the fiber-air interface with reflection R_1 while the sensing beam is transmitted into an optical cavity of length d , at the end of which can be an adjacent fiber or another reflecting surface with reflectivity R_2 , before being reflected back along the same optical path to a photodetector, as I_r . This then describes a reflection-mode FFPI. The sensing beam can also be transmitted as I_t beyond the cavity end as a transmission type FFPI. If R_2 is a highly reflective surface (such as a metallic film coating at the second fiber end or a mirror in air), then multiple reflections can occur between this surface and the reference interface, as illustrated in Fig. 2.1(b). The intensity distribution of the reflected (I_r) and/or transmitted (I_t) interfering beams from the FP cavity results in a set of fringes in which the distance between subsequent interference peaks (or valleys) is proportional to the distance (cavity length) between the two reflectors. The FFPI is thus extremely sensitive to longitudinal perturbations. In addition, due to its multiple reflections, the FP device generally has at least twice the sensitivity of other interferometers. In this case, the optical phase difference

thus induced will be amplified by the number of reflections, enabling a very high resolution to be obtained.

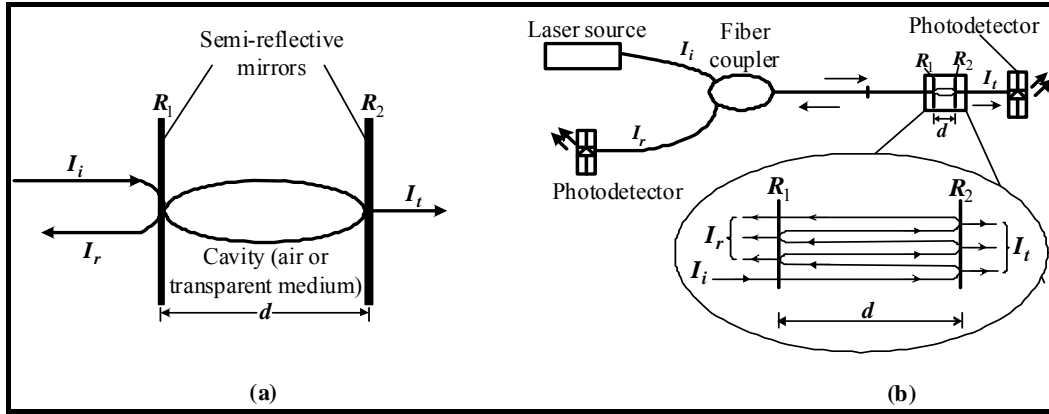


Fig. 2.1. Fabry-Perot interference: (a) interferometric cavity with medium of refractive index n and (b) fiber equivalent with illustrated multiple reflections from high-reflective surface.

Two typical FFPI configurations have been exploited in optical metrology (see Fig. 2.3). The intrinsic sensor in Fig. 2.2(a) has its optical cavity generally formed by a short fiber length abutting the transmission fiber. Both ends are perfectly cleaved and can be coated with a reflective film. The main inconvenience is the two fibers becoming detached. The extrinsic fiber Fabry-Perot interferometer (EFFPI), in which the probing light is allowed to exit the fiber end as shown in Fig. 2.2(b), is less affected by this problem. The sensing fiber serves to transmit the incident and reflected lightwaves to and from an optical cavity.

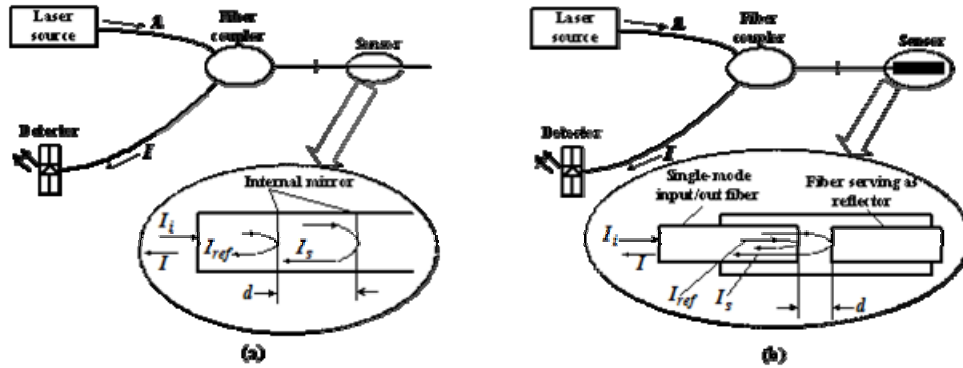


Figure 2.2. Fiber FPI configurations: (a) intrinsic device, and (b) extrinsic FFPI.

The measurand thus affects only the optical cavity length without modifying the fiber properties. Further, since both the reference (I_{ref}) and sensing (I_s) beams traverse identical paths in the sensing fiber, most common-mode perturbations are reduced.

2.2 Polarization-based dual-cavity extrinsic FFPI (EFFPI)

This section describes the development of the EFFPI device incorporating a specially-designed sensing probe for displacement measurements. I initially designed this sensor during my post-doctoral research at the *Ecole des MINES de Nantes* (2001–2003). Further development of this device is pursued since my appointment at INPT–ENSEEIH (Sept. 2003). The operating principles of the proposed sensor are first elaborated followed by its experimental validation. The all-important polarization behavior of the fiber sensor is next discussed. Important parameters such as the sensor's resolution, precision, dynamic range and directional detection are also addressed.

2.2.1 Operating principles and experimental validation

The EFFPI operates with an external optical cavity formed by the cleaved end of the sensing fiber and a reflecting surface whose movement is to be determined. Also, due to the generally low reflectivity of the reflective surfaces used, a relatively low finesse (<10) is obtained and the EFFPI can be assimilated to a two-beam interferometer [10]. However, as in all interferometers, the characteristic cosinusoidal output signal often leads to directional ambiguity in fringe motion when the measurands (compressive/tensile stresses, strains, vibration, etc) displace in counter directions, unless an additional reference arm or specific signal processing coupled to modulation schemes are employed.

This directional ambiguity can be overcome by introducing a phase lead and lag in the interference signal pair (i.e. sine and cosine fringes) via an electronic circuit [11]. Thus, when the sensing signal leads the reference signal, the target is seen as moving away from the sensing arm and vice versa. Modulating the laser diode drive current to obtain the phase lead and lag conditions has also been reported [12] whereby the sensing signal was generated from the drive current variation while the reference signal was un-modulated. Other schemes employed a homodyne technique to generate two interference signals phase-shifted by $\pi/2$ [13]. Heterodyne interferometry, more often employed in absolute distance measurements, can also be used [14] in which two beams from a single laser with slightly different wavelengths are modulated to obtain a 90° phase-shift between the beams.

In this work, the orthogonality of the fundamental injected mode is employed to obtain two sets of interference signals phase-shifted by $\pi/2$. The EFFPI undergoes no modulation to the laser source current and thus has an almost infinite bandwidth. Simple fringe counting is initially adopted for demodulating the interference pair into the desired parameter, the difference from other existing interferometers being that the quadrature signals are here generated uniquely optically, as demonstrated in Fig. 2.3 and Fig. 2.4.

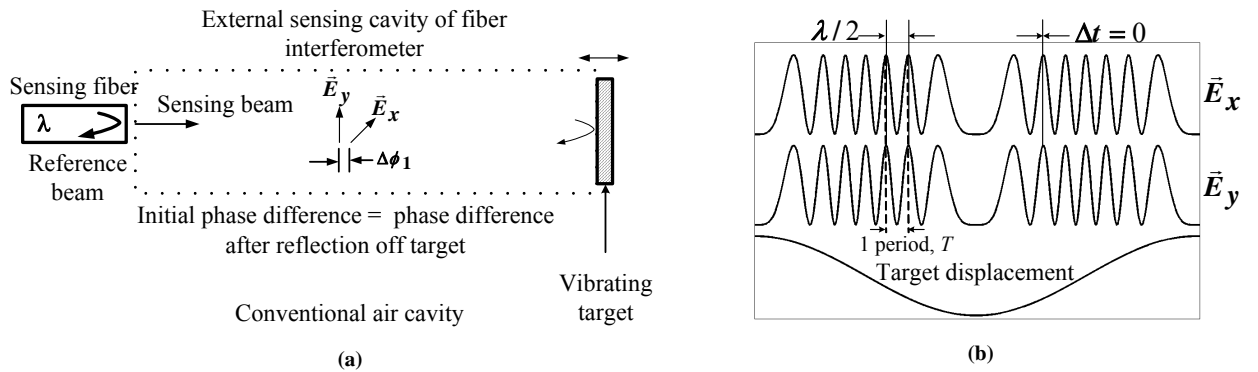


Fig. 2.3. Conventional EFFPI cavity: (a) both \vec{E}_y and \vec{E}_x components from fundamental mode \vec{E} are in phase, and (b) resulting interference fringes associated with \vec{E}_y and \vec{E}_x (simulated) versus target displacement.

The fundamental mode injected into the interferometric cavity, with an arbitrary polarization, can be decomposed into two orthogonal fields, \vec{E}_y and \vec{E}_x with an initial phase difference of $\Delta\phi_1$. If the cavity medium is homogeneous and the target surface not birefringent, then upon reflection off the latter, $\Delta\phi_1$ remains unaltered, hence \vec{E}_y and \vec{E}_x are not phase-shifted. The resulting interference with their respective reference components reflected off the fiber end will lead to two sets of interference signals which are in phase, with $\Delta t = 0$ (Fig. 2.3(b)). An optical retarder such as a quarterwave plate can, however, be inserted into the cavity to induce a relative phase difference of $\Delta\phi = \Delta\phi_2 - \Delta\phi_1$ ($\Delta\phi_2 \neq \Delta\phi_1$, in general), as in Fig. 2.4(a). If $\Delta\phi$ is $\pi/2$, then two sets of interference signals can be obtained whose intensities are

$$I_x = I_{xr} + I_{xs} + 2\sqrt{I_{xr}I_{xs}} \cos \Delta\phi_1 = I_{xr} + I_{xs} + 2\sqrt{I_{xr}I_{xs}} \cos \Delta\theta \quad (2.2)$$

$$\begin{aligned}
I_y &= I_{yr} + I_{ys} + 2\sqrt{I_{yr}I_{ys}} \cos \Delta\phi_2 = I_{yr} + I_{ys} + 2\sqrt{I_{yr}I_{ys}} \cos(\Delta\phi_1 - \pi/2) \\
&= I_{yr} + I_{ys} + 2\sqrt{I_{yr}I_{ys}} \sin \Delta\theta
\end{aligned} \tag{2.3}$$

where $\Delta\phi_1$ is generalized to become $\Delta\theta$, I_{xr} and I_{xs} , and, I_{yr} and I_{ys} are the reference and sensing intensities for both the x and y components, respectively. Equations (2.2) and (2.3) are then the quadrature interference pair to be employed to differentiate between phase-leads or phase-lags induced by a moving object to determine its directional sense.

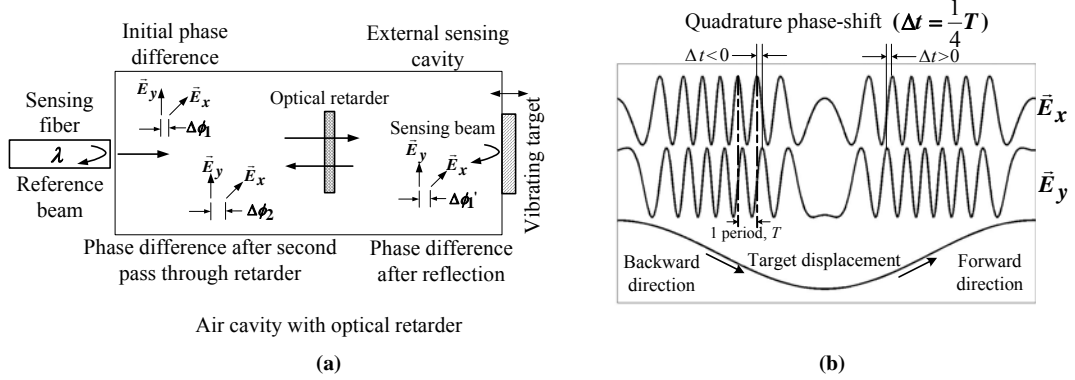


Fig. 2.4. Optical dual-cavity EFFPI: (a) optically generated $\pi/2$ phase shift between \vec{E}_y and \vec{E}_x , and (b) quadrature interference pair (simulated) as a function of target displacement.

This quadrature point corresponds to a temporal Δt value of $1/4$ of a fringe period (or $\Delta t_i = 1/4T_i$ with i the corresponding fringe number), as shown in Fig. 2.4(b). Then for negative Δt , the target moves away from the sensor while positive Δt indicates target movement towards the sensing fiber. An optically generated dual-cavity EFFPI sensor in quadrature is thus achieved.

The experimental validation of the dual-cavity sensor is next carried out using the set-up shown in Fig. 2.5. Monochromatic light from a 1310 nm *Modulight* fiber-pigtailed DFB-type laser diode (LD) is injected into the interferometer and guided via a 1x2 fiber coupler (FC) to the sensing fiber (SF) end where $\sim 3.6\%$ is back-reflected as the reference wave (RW). This wave is a contribution of 2 orthogonal polarization components since the injected mode is slightly elliptically-polarized. The remaining light is transmitted as the sensing wave (SW), collimated via an anti-reflection coated collimator, traverses an optical retarder oriented at $\sim 45^\circ$ to its polarization direction and upon its return trip after reflection off a micro-prismatic target, results in a relative phase shift of $\pi/2$.

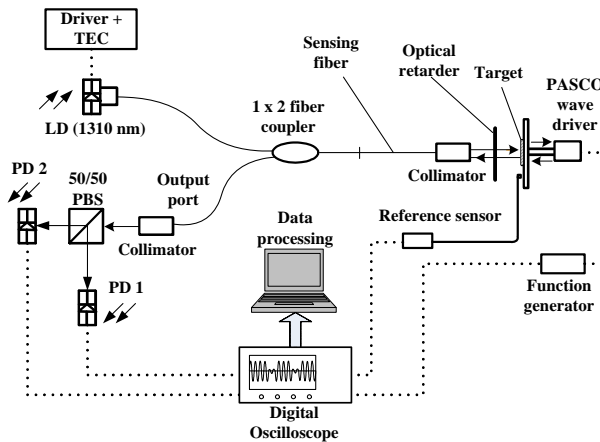


Fig. 2.5(a). Configuration of dual-cavity EFFPI sensor used during experimental validation.

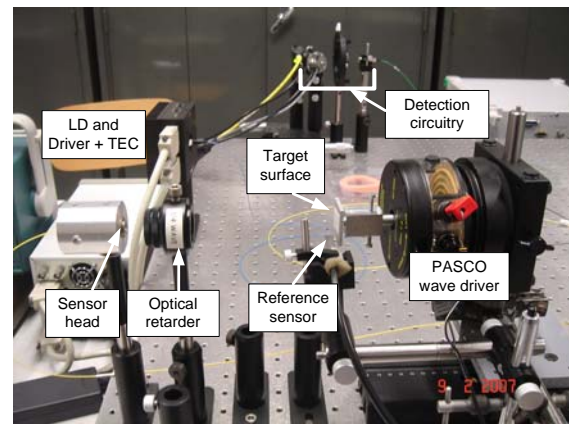


Fig. 2.5(b). Image of experimental set-up of fiber sensor.

After reflection off the target surface, SW is re-injected into SF where its phase-shifted components combine with their respective reference components, leading to two sets of interference signals. These are guided to the output port of FC where a 50/50 polarizing beam-

splitter decomposes the orthogonal interference signal sets to two respective photodetectors. The micro-prismatic target is secured to a mechanical vibrator and excited using a function generator at 100 Hz with an amplitude of 500 mV. Two quadrature interference signals from \vec{E}_y and \vec{E}_x are therefore induced, as validated experimentally in Fig. 2.6. A *Philtec D63* displacement sensor with a sensitivity of 2.786 mV/ μm and a quoted precision of 125 nm is employed as reference for comparison. The relative temporal difference of the quadrature pair clearly determines the directional sense of the target displacement ($\Delta t < 0$: movement away dual-cavity EFFPI sensor and $\Delta t > 0$: movement towards sensor). Note also that Δt is $\frac{1}{4}T$ at the i^{th} fringe (illustrated by the second fringe), confirming that a quadrature condition has been achieved between the interference pair.

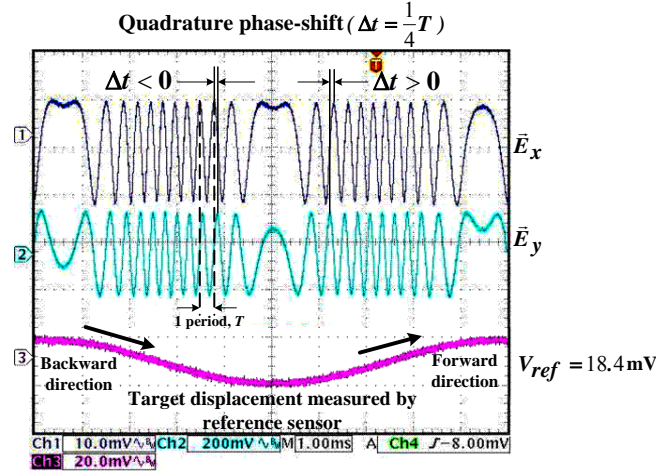


Fig. 2.6. Quadrature interference pair obtained from dual-cavity EFFPI sensor together with reference displacement curve.

This experiment clearly demonstrates the proof-of-concept of the dual-cavity fiber interferometer where in-quadrature dual interference cavity operation of the specially-designed sensor head has been achieved. The intrinsic resolution of the sensor is limited to $\lambda/2$ here. Improvements to the sensor resolution and precision will be discussed later when two competing interference signal demodulation schemes are implemented.

2.2.2 Polarization-induced influence in dual-cavity EFFPI sensor

One important criterion to the correct operation of the dual-cavity EFFPI sensor is the state of polarization (SOP) of the interfering lightwaves since the device is based on optically decomposing the fundamental mode into 2 orthogonal polarization components in quadrature. The SOP must be initially known so that the injected lightwave can be manipulated to optimize the sensor performance. since under certain conditions, perturbations to the SOP of one or both of the \vec{E}_y or \vec{E}_x fields can lead to complete extinction of one of the interference signals while leaving a non-zero fringe visibility in the other component. This phenomenon is commonly known as polarization-induced signal fading (*PIF*). Note that the orthogonal components are of dissimilar amplitudes hence an elliptical SOP representation on a polar plot is generally obtained.

The objective here is to demonstrate the sensibility of the dual-cavity EFFPI sensor to *PIF* when only one optical element, i.e. a $\lambda/4$ waveplate, is used to obtain quadrature signals and to propose a potential solution to reduce its influence. Now, the 2 polarization states in SF can be represented by their combined fields as $\vec{E}_{t(i)} = \vec{E}_{r(i)} + \vec{E}_{s(i)}$, with \vec{E}_r and \vec{E}_s the reference and sensing fields, and index i either of the orthogonal components. Here, *PIF* is induced by introducing bends into SF as shown in Fig. 2.8. The sensor SOP is then measured in conjunction with the quadrature phase-shifted interference signals.

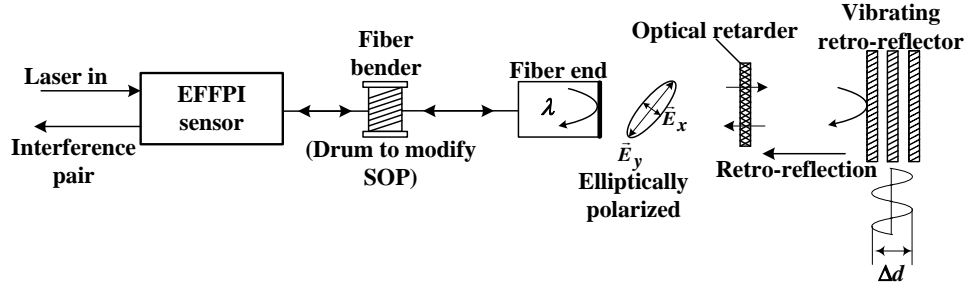


Fig. 2.8. Experimental set-up used to induce polarization-induced stress into sensing fiber by winding fiber on 10 cm diameter aluminum mandrel

Under no bending stress, Figs. 2.9 shows the interference signals to be in quadrature and the SOP between the \vec{E}_y and \vec{E}_x fields remains very slightly elliptical with an orientation of $\alpha = 20^\circ$. The visibility of the x component (V_{mx}) is measured as 31.19% while that of the y component (V_{my}) is $\sim 25.0\%$. The ellipticity is defined as $e = (1 - b^2/a^2)^{1/2}$ with $2a$ representing the major axis of the ellipse and $2b$ the minor axis of the same ellipse.

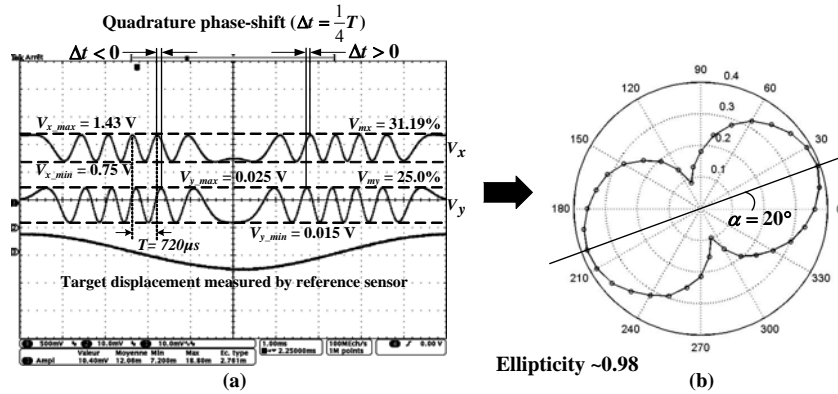


Fig. 2.9. (a) Quadrature interference pair measured under no bending and (b) its corresponding SOP orientation

SF is next wound 3 turns around an aluminum mandrel and the evolution of the orthogonal interference signals measured. As seen in Fig. 2.10(b), the visibility of the y -component interference signal is strongly attenuated to $\sim 1.4\%$ rendering it un-exploitable. This *PIF* phenomenon also induces a rotation of the output SOP away from the PBS principal axes where $\alpha = 10^\circ$ now, as plotted in Fig. 2.10(a).

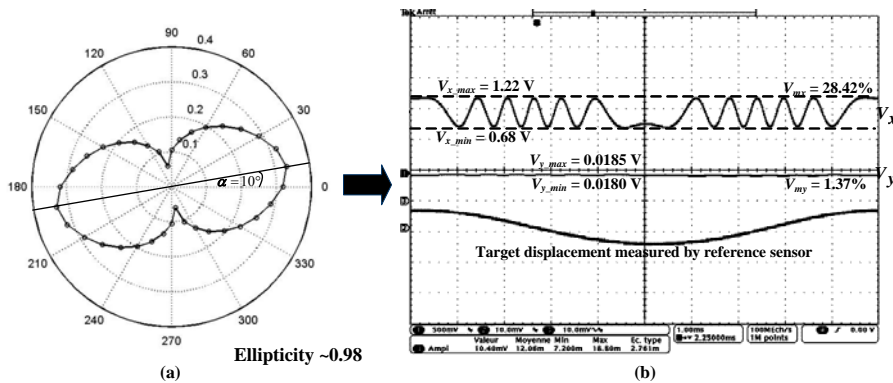


Fig. 2.10. (a) SOP in polar plot with $\alpha = 10^\circ$ and (b) PIF attenuation of \vec{E}_y interference component after 3 rounds of bending

The sensor configuration is thus not resistant to *PIF* and this can be particularly impractical when SF has to be displaced from its original set-up position as the waveplate has to be continuously re-orientated to ensure balanced visibilities from the orthogonal components. One solution without resorting to polarization-maintaining fiber components is to impose a circular SOP in the reflected SW propagating in fiber. Thus, interference from the x and y components can continuously take place between SW and RW.

To produce the desired circularly-polarized light, polarization-controlling optics consisting, in the respective order, of first a $\lambda/4$ waveplate followed by a linear polarizer (LP), are inserted along the optical path between SF and the target, as shown in Fig. 2.11.

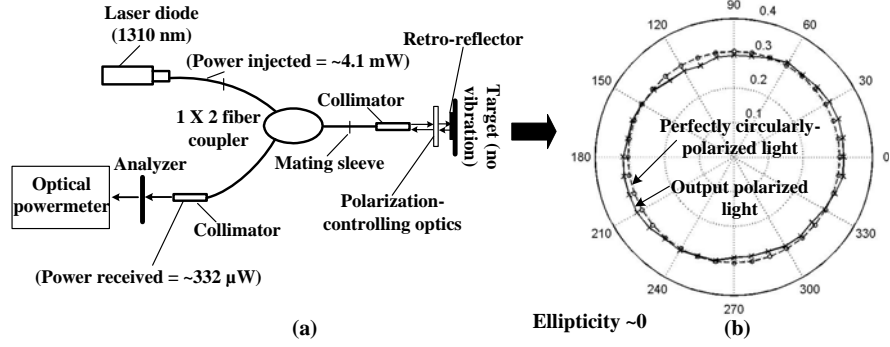


Fig. 2.11. Experimental validation of optically-generated dual-cavity EFFPI (a) using passive polarization-controlling optics to obtain (b) circular SOP at interferometer output

RW, which is reflected off the fiber end, exhibits identical an SOP as the injected light vector (given by $e = 0.98$). The transmitted beam, on the other hand, has its SOP phase-shifted by $\pi/2$ before being transformed into a linear polarization after LP. The second passage through LP, which also serves to filter parasite polarization transformation of SW after reflection off the target, conserves the linear SOP of the returning beam. The $\lambda/4$ waveplate, oriented at 45° to the optical axis of LP, subsequently transforms this linear SOP into a circularly-polarized state (ellipticity ~ 0) to be re-injected into SF. The beating with the almost linear RW will thus lead to a relatively circular SOP being continuously obtained, resulting in two in-quadrature interference signals within a single fiber arm, hence the dual-cavity nature of the EFFPI.

To validate *PIF* tolerance, the sensor is subjected to bending stress as previously described. Figs. 2.12 show the evolution of the interference signals incorporating the novel optical configuration in the presence of bending stresses.

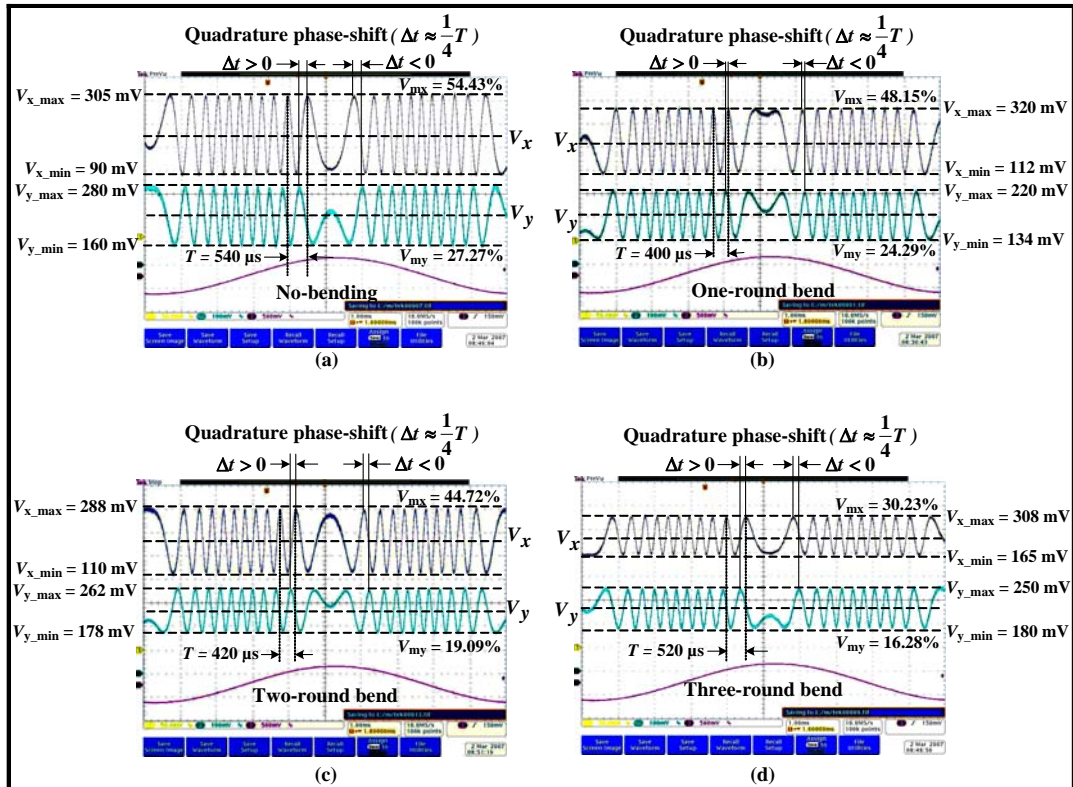
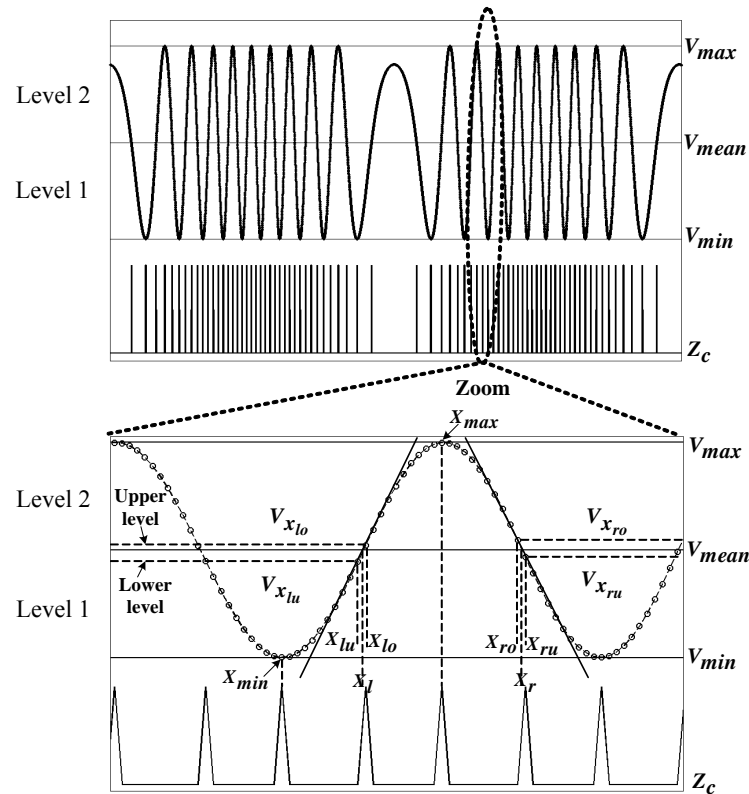


Fig. 2.12. PIF resistance of EFFPI sensor employing novel polarization optics for: (a) no fiber bending, (b) one-round bend, (c) two-round bends and (d) 3-round bends

It is seen that even under strong external perturbations, the output visibilities are only slightly attenuated, from 54.43–30.23% ($\sim 44\%$ reduction) for V_x and 27.27–16.28% ($\sim 40\%$ reduction) for V_y , respectively, without suffering complete extinction. The principal implication, however, is that the quadrature phase-shift between both components is continuously maintained, as evident from Δt being $\sim 1/4T$ with relatively small quadrature errors. The specially-designed optical probe of our sensor, incorporating the polarization-controlling optics, can thus be potentially exploited to reduce *PIF* effects [15].

Several well-known demodulation techniques for processing interference fringes from various fiber interferometers exist. These include automated fringe counting, digital curve-fitting, linear digital phase-locking, fringe-tracking, and phase-tracking [16-21]. However, optical fringe counting remains one of the most practical methods available for measuring beat frequency, displacement and optical path difference or phase-shift [22-23].



Two additional points from each position between the lower and upper levels where V_{mean} crosses over are denoted as the over-points (X_{lo} and X_{ro}) and the lower-points (X_{lu} and X_{ru}), and are used to determine the exact crossing-over points, X_l and X_r , respectively, with

$$X_l = \frac{V_{mean} - V_{X_{lu}}}{V_{X_{lo}} - V_{X_{lu}}} (X_{lo} - X_{lu}) + X_{lu} \quad (2.4)$$

$$X_r = \frac{V_{mean} - V_{X_{ru}}}{V_{X_{ro}} - V_{X_{ru}}} (X_{ro} - X_{ru}) + X_{ru} \quad (2.5)$$

For one set of interference fringe, zero-crossing signals (Z_c) are obtained at 4 points (X_l , X_r , X_{max} and X_{min}) in one period with X_{max} and X_{min} the peak and valley points, respectively. Now, by exploiting the quadrature phase-shift between V_y and V_x , zero-crossing signals can be generated at 32 points by sub-dividing the amplitude into 8 levels for each interference signal hence, leading to an increased resolution of $\lambda/64$ as shown in Fig. 2.14. This resolution is considered sufficient for the targeted application.

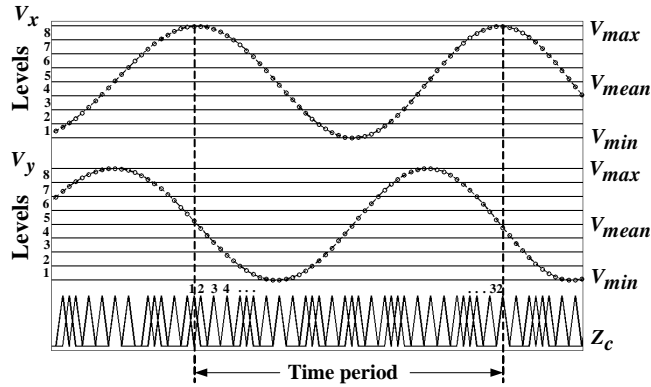


Fig. 2.14. 8 levels of zero-crossing signals to achieve $\lambda/64$ precision

The demodulation scheme is implemented using a software program written in MATLAB, the flow process of which is illustrated in Fig. 2.15.

Two sets of zero-crossing signals (Z_c) associated with V_y and V_x can thus be integrated within the same time length and counted together. The displacement curve for the vibration amplitude is then plotted by the program via $D = Z_c \lambda / 64$ where Z_c is the total number of combined crossing-over points.

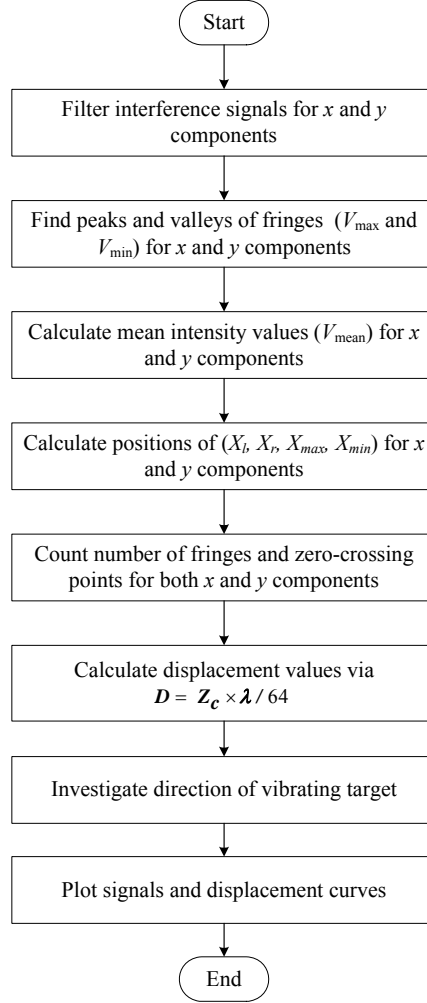


Fig. 2.15. Block representation of demodulation algorithm

The demodulation technique is next validated for the dual-cavity EFFPI sensor over a controlled displacement of $30.02 \mu\text{m}$ (given by the reference sensor) at 30 Hz. The processed output from the program, shown in Fig. 2.16, gives a total count of $Z_c = 1468$ which computes to a displacement of $30.04 \mu\text{m}$ for a $\lambda/64$ step size. A maximum discrepancy of 20 nm (or relative difference of 0.07%) is obtained which can be attributed to very slight power and temperature variations of the LD source, a slight deviation from normal incidence of SW on the target surface, and/or noise from the reference displacement sensor, etc.

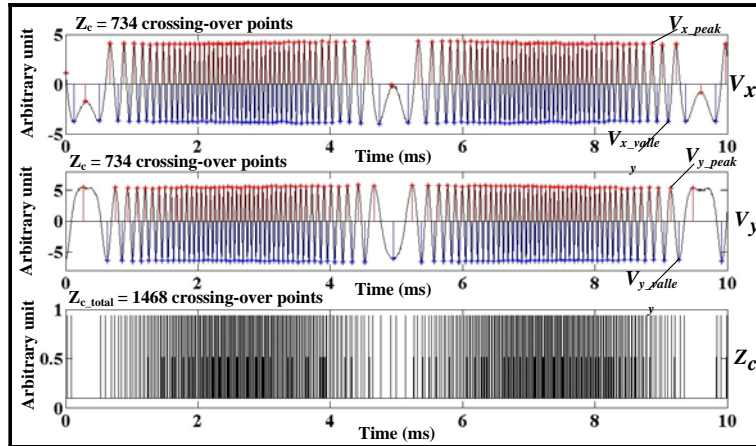


Fig. 2.16. Modified fringe counting demodulation program for a total count of $Z_c = 1468$ points, corresponding to $30.04 \mu\text{m}$ displacement

Further, the displacement amplitudes from both sensors, as plotted in Fig. 2.17, illustrate good accuracy obtained using the modified fringe counting technique. Note also that the demodulation resolution of $\lambda/64$ corresponds to ~ 20 nm for the DFB-LD emitting at 1310 nm.

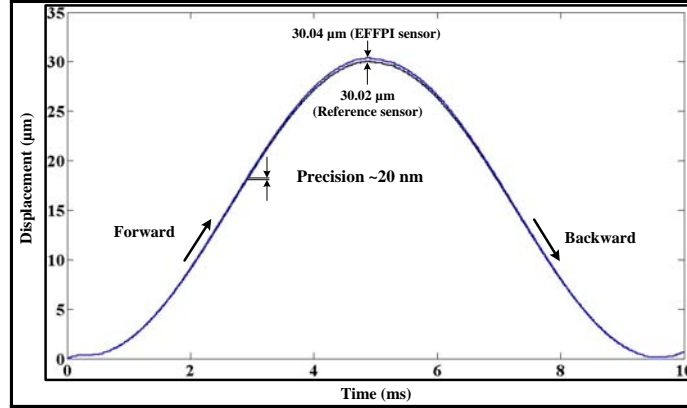


Fig. 2.17. Displacements measured by EFFPI and reference *D63 Philtec* sensors over 1 period

2.2.4 Dual-cavity EFFPI sensor characteristics and performance

The accuracy and precision of the EFFPI sensor are next investigated to treat potential error sources. An "ideal" dynamic displacement is simulated via $d = A \cos(2\pi ft)$, with A its amplitude (μm) and f the excitation frequency. Any variations in d will thus be reflected by the evolution of the quadrature interference fringes. The sensitivity of the *PASCO* wave driver is determined to be $\sim 7.67 \mu\text{m/mV}$ over the displacement range investigated.

Table II summarizes the simulated signals (D_{sim}), the EFFPI sensor (D_s) and the reference sensor (D_{ref}) measurements over a range of ~ 6 – $30 \mu\text{m}$. Displacement errors are also obtained from comparisons between 1) simulation and EFFPI data, 2) reference sensor and EFFPI data, and 3) simulation and reference sensor data. A minimum error of 0.07% is obtained between the reference sensor and EFFPI data while a maximum error of 1.81% occurs between the simulation and reference sensor data. The relative average displacement errors over the displacement range from the three different comparisons are found to be 0.76%, 0.57% and 1.14% respectively. No noise has been incorporated into the simulated signals while the experimental signals (interference pair and reference signal) contained a certain level of noise. The *Philtec D63 model* displacement sensor has a 0.35 mV_{p-p} (peak-to-peak) rms noise amplitude. The EFFPI displacement error is relatively independent of the displacement variations but could be induced by noise, temperature variations of the LD and/or incidence angle of SW with respect to the target surface.

Table II
Displacements obtained from 3 demodulated signals and corresponding relative displacement errors

D_{sim} (μm)	D_s (μm)	D_{ref} (μm)	Error comparison for simulation-EFFPI (%)	Error comparison for reference sensor-EFFPI (%)	Error comparison for simulation-reference sensor (%)
6.289	6.326	6.300	0.59	0.41	0.17
7.906	7.943	7.978	0.47	0.44	0.91
11.963	12.048	12.18	0.71	1.08	1.81
19.989	20.16	20.33	0.86	0.84	1.71
29.724	30.043	30.021	1.07	0.07	1.00

Further, comparison of the EFFPI data with the reference displacement leads to an accuracy of ~ 48 nm (or relative accuracy of 0.57%) while the precision of the sensor system is

$\sim \pm 56$ nm (or $\pm 0.4\%$) over the same displacement range. These values are deemed acceptable for a practical sensor device.

A major parameter with a direct impact on the sensor's accuracy is temperature variation which causes the laser wavelength to vary through an empirical relationship [29]

$$\lambda(T) = \lambda_{T_0} + \frac{d\lambda}{dT}(T - T_0) \quad (2.6)$$

with λ_{T_0} a central wavelength (~ 1309.636 nm ± 1 pm) emitted by the DFB-LD at a characteristic temperature T_0 (25°C), $d\lambda$ the wavelength shift with temperature variation dT . The subsequent displacements induced by these variations is then $D = Z_c \lambda(T)/64$ so that errors induced during vibration measurements can be estimated through $D_{error} = Z_c \Delta\lambda(T-T_0)/64$, with $\Delta\lambda(T-T_0)$ the wavelength difference over a temperature variation.

The DFB-LD wavelength sensitivity to temperature is measured as ~ 65 pm/ $^\circ\text{C}$ for increasing temperatures of 10 – 40°C in 1°C steps, as shown in Fig. 2.18. For decreasing temperatures, this is ~ 56 pm/ $^\circ\text{C}$ from $\sim 35^\circ\text{C}$ downwards whereas above this temperature, the gradient is seen to at least double. This could be due to the inherent thermal inertia which exists upon cooling the laser. Nevertheless, the greater value of 65 pm/ $^\circ\text{C}$ is used here, implying that subsequent errors are associated with the maximum possible values with respect to the wavelength-temperature gradient.

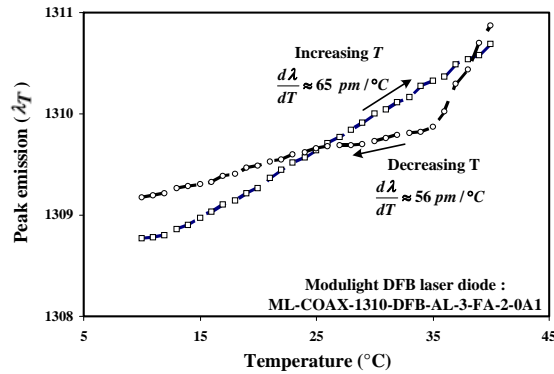


Fig. 2.18. Temperature sensitivity of DFB-LD wavelength with increasing and decreasing temperatures

To estimate the errors, an equivalent constant displacement of ~ 6.586 μm is imposed on the vibrating target while the DFB-LD temperature is varied from 10 to 40°C in steps of 5°C . The demodulated displacements from the EFFPI sensor, D_s , are carried out in conjunction with the reference sensor, D_{ref} and the errors plotted in Fig. 2.19.

Now, defining the relative displacement variation as $\Delta D_s/D_{avg}$, where $\Delta D_s = D_{s(max)} - D_{s(min)}$ is the difference between the maximum and minimum displacements over the entire range of D_s , and D_{avg} the mean displacement over the temperature range studied, one obtains $\Delta D_s/D_{avg} \sim 1.37 \times 10^{-3}$ for $D_{s(min)} \sim 6.585$ μm at 10°C and $D_{s(max)} \sim 6.594$ μm at 40°C as shown in Fig. 2.20.

The potential accuracy of the sensor is estimated as ~ 1 nm with a maximum error of 0.121% at 40°C (c.f. reference displacement). This error, although minimal for the displacement range studied, can become detrimental to the sensor performance if very large displacements are to be measured (i.e. for very large number of fringes). Now, since the displacement measured varies as a function of source wavelength which, in turn, is proportional to its temperature, then a relative wavelength variation can be found where $\Delta\lambda/\lambda_{avg} = (1310.69 - 1308.772\text{nm})/1309.649$ nm $\sim 1.49 \times 10^{-3}$ (measured with ± 1 pm precision). This value is in good agreement with the relative displacement variation determined earlier (1.37×10^{-3}). The wavelength stability over an 8-hr period is also found to vary from an initial 1309.637 nm to 1309.641 nm, thus equating to a relative variation of less than 0.0004% . The discrepancy observed between the EFFPI sensor and

the *Philtec* sensor can also be explained by the limited precision of the latter (quoted as 125 nm by the manufacturer) whereas the former has been designed with a precision of ~56 nm.

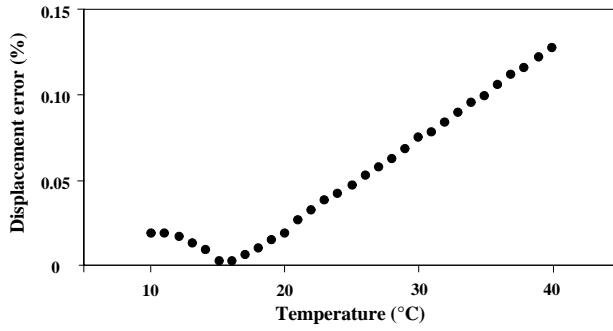


Fig. 2.19. Plotted errors induced due to temperature variation from 10–40°C

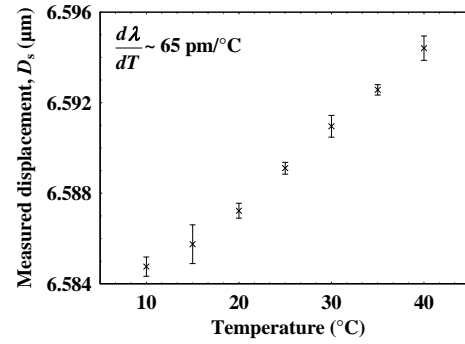


Fig. 2.20. Measured displacements for temperature variation of 10–40°C (vertical bars: absolute errors)

The final error source studied is that due to the target orientation with respect to the sensing beam. The demodulated displacement for a small angle α from perpendicular incidence is then given by [30]

$$D = Z_c \frac{\lambda}{64} = Z_c \frac{1}{64} \frac{4\pi n \Delta d}{\Delta \phi \cos \alpha} \quad (2.7)$$

where the optical phase variation $\Delta \phi$ due to an induced displacement Δd is $\Delta \phi = 2\pi n \Delta d / \lambda \cos \alpha$. If $\alpha \neq 0^\circ$, then an apparent displacement is measured instead of the true value due to the $\cos \alpha$ term, leading to an error. A simple analysis for $\alpha = 1^\circ$ and 2.5° results in displacement errors of 0.038% and 0.21% respectively.

Displacements ranging from 6.590 μm to 7.609 μm are measured by the EFFPI sensor for an angle variation of $0 - 30^\circ$ and plotted in Fig. 2.21. As is obvious, the errors incurred in the measured displacement, with respect to the true displacement of the vibrating target, are found to increase when α increases. This is principally due to the fact that, even for a constant vibration amplitude, the optical path length (OPL) “seen” by the sensing beam is increased, manifesting as the cosine term in (2.7), thus leading to an increased apparent displacement. Nevertheless, for an error of less than 1%, the dual-cavity EFFPI sensor can tolerate a beam misalignment of $\alpha \sim 10^\circ$.

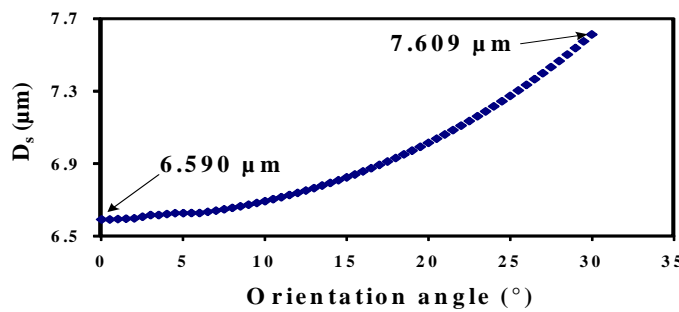


Fig. 2.21. Apparent displacement measured by dual-cavity EFFPI α variation from $0-30^\circ$

2.2.5 Applications to vibration measurements

The dual-cavity EFFPI sensor incorporating the demodulation technique is next tested against dynamic displacements under various excitation waveforms (sinusoidal, triangular, square, ramp, and triangular pulse). These are generated by a *PASCO Scientific SF-9324* wave driver driven by a *Tektronix AFG 3252* function generator. The target surface is a micro-prismatic retro-reflector attached to the vibrating arm of the wave driver. The ensuing

interference signals detected by the photodetectors are then recorded by a digital oscilloscope before being transferred to a dedicated computer for demodulation.

Fig. 2.22 plots the displacements, D_s , for sinusoidal and triangular waveforms at 125 Hz with excitation amplitudes from 0.1–5 V. D_{ref} is the reference displacement while ΔD_{imax} represents the maximum difference in displacements between the two devices. Note that the quadrature condition is maintained throughout the experiments, affirming the stability of the optically-imposed phase-shift. Each displacement point is measured at least 20 times over a range of ~ 0.7 – $118.167 \mu\text{m}$ for the sinusoidal profile and ~ 0.7 – $81.65 \mu\text{m}$ for the triangular profile. In the former case, the average error is $\sim 0.77\%$ with respect to the reference data ($\sim 0.655 \mu\text{m}$) with an average precision of $\sim \pm 0.16 \mu\text{m}$ (or $\pm 0.34\%$).

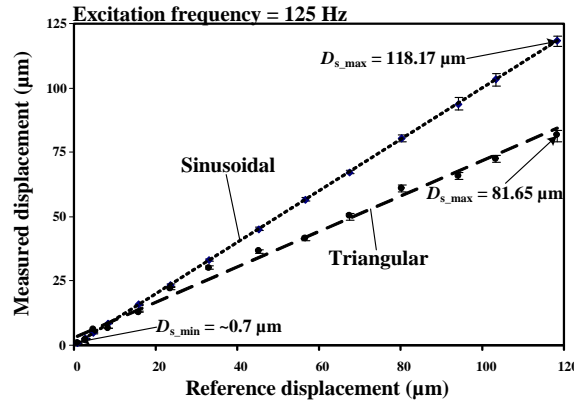


Fig. 2.22. Sinusoidal and triangular displacement profiles detected by EFFPI sensor at 125 Hz

For the triangular excitation, comparison with the reference sensor results in an average difference of 0.76% together with an average precision of $\sim \pm 0.14 \mu\text{m}$ (or $\pm 0.40\%$). Physically, this waveform is similar in property to the sinusoidal excitation since it has only one peak and one valley over one period, corresponding to the directional changeover of the moving target. The target displacement has been detected without any directional ambiguity.

It is further seen that the sinusoidal excitation induces a larger displacement amplitude than the triangular waveform since the bandwidth limit of the wave driver (0.1–1000 Hz) results in higher frequency components from non-sinusoidal waveforms being cut off. For the triangular excitation, some harmonics have effectively been cut off as its total energy (amplitude) is smaller than that of the sinusoidal waveform. The excitation frequency is therefore reduced to 13 Hz for the subsequent squarewave, ramp and triangular pulse waveforms.

The non-sinusoidal displacements measured by the EFFPI sensor are plotted in Figs. 2.23. The average error and precision for displacements induced by the squarewave, ramp and triangular pulse are, respectively, 0.19% and $\pm 0.17 \mu\text{m}$ (or $\pm 0.30\%$ in relative precision), 0.26% and $\pm 0.13 \mu\text{m}$ (or $\pm 0.36\%$), and, 0.56% and $\pm 0.15 \mu\text{m}$ (or $\pm 0.39\%$) over the entire dynamic range studied. With squarewave excitation, the displacement range is ~ 0.7 – $76.73 \mu\text{m}$. For ramp excitation, the measured displacements extend from 0.7 – $84.46 \mu\text{m}$ while the triangular pulse induces displacements ranging from 0.7 – $90.62 \mu\text{m}$. These are plotted against the reference displacement in Fig. 2.23(d) where the vertical error bars represent the calculated precision.

The observation of the triangular excitation inducing the largest displacement relative to the squarewave signal, which on the other hand, excites the smallest displacement can be attributed to the fact that the total energy of the square signal contains only odd harmonics along with the fundamental frequency. Hence, its output energy is lower with respect to the other 2 waveforms. In all cases, the non-sinusoidal signals result in a smaller excited displacement range as compared to the sinusoidally-excited displacement. Nevertheless, the experimental results clearly demonstrate the capability of the EFFPI sensor for measuring dynamic displacements under various operating conditions with reasonably good precision.

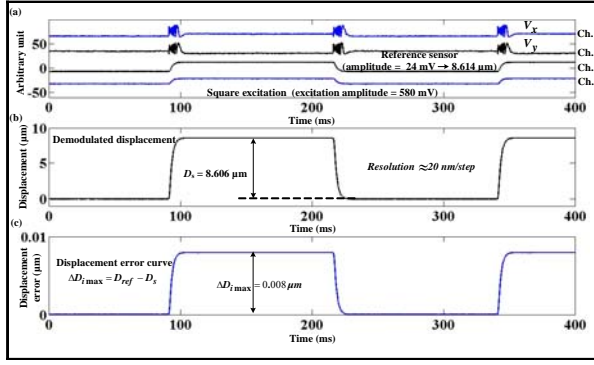


Fig. 2.23(a). Squarewave excitation with $\Delta D_{imax} = 8 \text{ nm}$

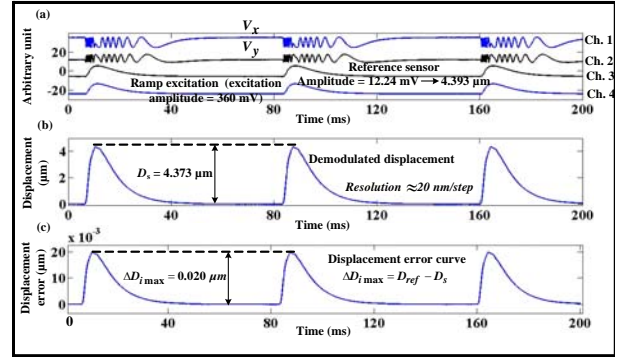


Fig. 2.23(b). Ramp excitation with $\Delta D_{imax} = 20 \text{ nm}$

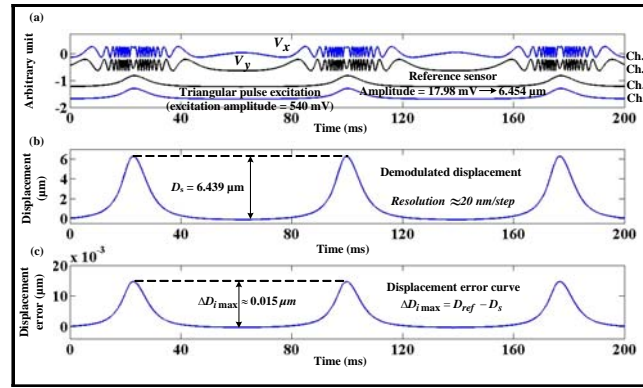


Fig. 2.23(c). Triangular pulse excitation with $\Delta D_{imax} = 20 \text{ nm}$

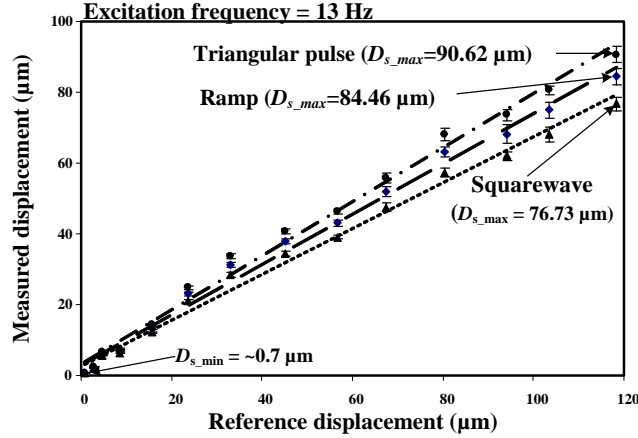


Fig. 2.23(d). Displacements detected by EFFPI sensor against reference displacement for squarewave, ramp and triangular pulse excitations

In collaborative work with Tyndall National Institute in Cork, Ireland, the dual-cavity EFFPI sensor is used for calibrating the vibration noise level of an acoustic vibrator to align and optimize the self-formation of opal photonic nano-crystals during their growth stage [31]. As shown in Fig. 2.24(a), this technique enables a tenfold improvement in the crystallographic ordering of the nano-crystals in the (111) plane, as compared to other crystallization methods. An SEM image of the crystallographic assembly of the opal film is illustrated in Fig. 2.24(b), illustrating the excellent quality of the opal nano-film synthesized.

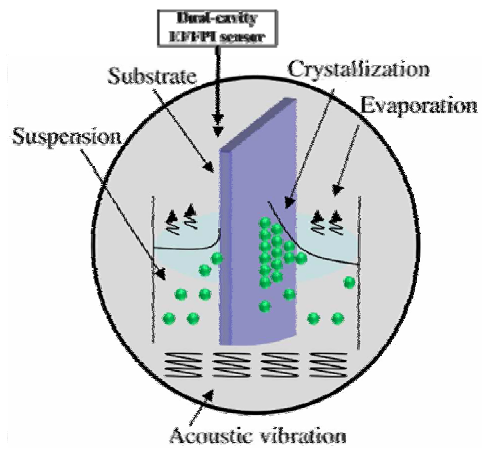


Fig. 2.24(a). Dual-cavity EFFPI sensor for calibrating vibration noise to apply for opal nano-crystal growth

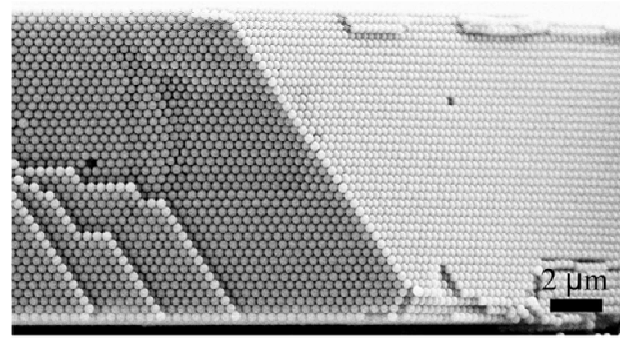


Fig. 2.24(b). SEM image of crystallographic orientation of opal nano-crystal film in (111) plane

2.3 Dual-modulation EFFPI with double reflection

The second half of this chapter concerns the evolution of the dual-cavity EFFPI sensor into a modulation-based device to overcome polarization instability over the long term. Further, the previous sensor is unsuitable for slowly-varying displacements. The modulation-based EFFPI sensor has been developed during the LINES (Laser Interferometry for Earth Strains) research project under the ANR Natural Risk Program for geophysics and has a patent application pending (France, USA, Europe and Japan). The operating principles are first described followed by its experimental validation. Various characteristics concerning the performance of the fiber device are next elaborated following the description of the demodulation technique employed.

2.3.1 Operating principles of dual-modulation EFFPI sensor

Unlike the all-optical dual-cavity EFFPI sensor discussed above, the modulation-based interferometer employs high-precision electronic modulation to achieve quadrature phase-shift. In addition, the sensor can also operate under quasi-static displacement conditions [32]. The interference signal at wavelength, λ_1 , is given in voltage terms as

$$V_x = V_{0x} + V_{mx} \cos(\theta + \varphi) \quad (2.8)$$

with V_{0x} the dc component, V_{mx} the ac component representing the fringe visibility, θ the optical phase induced between the reference and sensing waves (representing sensing cavity length variation), and φ an arbitrary phase. Since θ is calculated modulo π , directional ambiguities can arise [33-35] and can subsequently be overcome by generating another quadrature phase-shifted interference signal, V_y , via φ so that

$$V_y = V_{0y} + V_{my} \cos\left(\theta + \frac{\pi}{2}\right) = V_{0y} + V_{my} \sin(\theta) \quad (2.9)$$

where the terms on the right have the same definitions as in (2.8). The modulation scheme is introduced via the experimental set-up shown in Fig. 2.25.

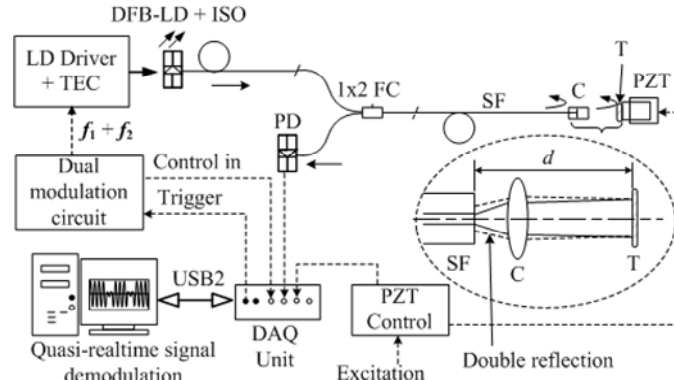


Fig. 2.25. Experimental configuration of dual-modulation EFFPI sensor

A temperature-stabilized fiber-pigtailed DFB-LD incorporating an optical isolator (ISO) illuminates the interferometer via a fiber coupler (FC). A reference wave (RW) of $\sim 3.7\%$ is reflected off the FC/PC end of the sensing fiber (SF) while the remaining light is transmitted via an AR-coated collimator (C) and back-reflected by a target (T) into SF as the sensing wave (SW). T is a front-face reflecting mirror ($>90\%$ reflectivity) at a distance d from the SF end. A target mirror is used here to avoid any SOP distortion which can occur with polymer-based retro-reflectors in this "single-cavity" interferometer and implicitly means a strict alignment constraint on SW. However, double reflection is obtained due to a combination of high reflectivity from SF's ceramic ferrule (CF) and the mirror [32,36], as shown in the inset of Fig. 2.25. This

subsequently enables the interferometer resolution to be doubled since the apparent cavity length d is now doubled.

Now, the wavelength amplitude of the first modulation component, f_1 , to achieve quadrature has to satisfy the condition $\Delta\lambda/\lambda^2 = 1/8nd$, with n the refractive index of the sensing cavity (~ 1 in air) and $d = 25$ mm. Also, $\Delta\lambda = \lambda_2 - \lambda_1$ with $\lambda_1 \approx \lambda_2 \cong \lambda$ (~ 1311.10 nm at 24°C). The wavelength-current response $\Delta\lambda/\Delta I$ is $\sim 9\text{pm/mA}$ and the corresponding current modulation amplitude $\Delta i(t)$ is ~ 0.48 mA, translating to an equivalent $\Delta\lambda$ of ~ 4.30 pm. f_1 is implemented as a squarewave modulation at 25 kHz and has been chosen for its compromise in terms of accuracy for geophysics where the phenomena to be monitored are typically in the 10^{-3} – 10^2 Hz range with amplitudes of 10^{-9} – 10^{-3} m.

f_1 , at 25 kHz, also corresponds to the spectral response limit of the DFB-LD under squarewave excitation [37]. The unique photodetector (PD) thus detects a multiplexed signal containing the interference pair, as shown in Fig. 2.26(a), which is subsequently demultiplexed to obtain V_x and its quadrature component V_y (Fig. 2.26(b)), using a phase demodulation technique which will be described below [38].

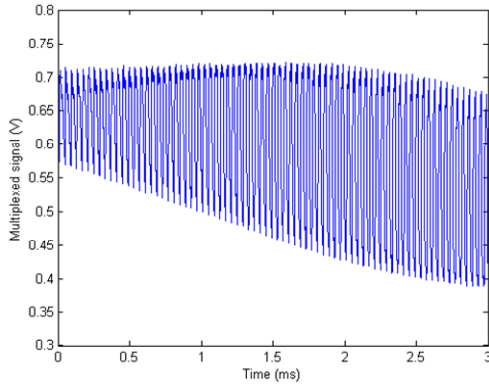


Fig. 2.26(a). Multiplexed interference signal

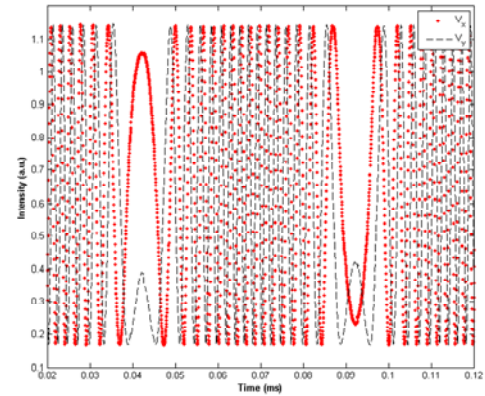


Fig. 2.26(b). Demultiplexed V_y and V_x

The quadrature phase-shift condition induced by f_1 is validated experimentally where, for an arbitrary displacement (~ 5 μm), V_y plotted against V_x imperatively traces a perfect circle (i.e. with zero quadrature error) on the Lissajous phase diagram, as illustrated in Fig. 2.27.

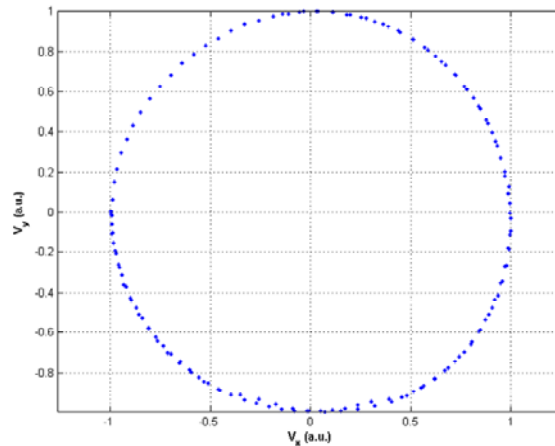


Fig. 2.27. Lissajous phase diagram for V_y vs V_x in quadrature (circle with zero quadrature phase error)

Here, one complete trajectory on the phase diagram represents an equivalent displacement of $\lambda/4$ due to double reflection.

Now, in the case when T is immobile or displaces very slowly then either no fringes are generated or the induced small-amplitude signals might be misinterpreted as intrinsic drifts of the sensor system. To overcome this ambiguity, a second modulation, f_2 , is applied to generate a reference set of fringes so that V_y versus V_x traces a bidirectional trajectory of $\geq 2\pi$ on the

Lissajous phase diagram with the condition $\Delta\lambda/\lambda^2=1/2nd$. The corresponding current amplitude is $\Delta i(t) \sim 1.94$ mA for $\Delta\lambda \sim 17.19$ pm. Hence, for a stationary T , f_2 , used simultaneously with f_1 , induces an equivalent displacement of $\Delta d \geq 327.8$ nm. f_2 employs a triangular excitation at ~ 1 Hz, applied together with f_1 , as shown in Fig. 2.28 and is selected to enable it to be easily distinguished from f_1 while 1 Hz is considered sufficiently rapid with respect to the DFB-LD power variation.

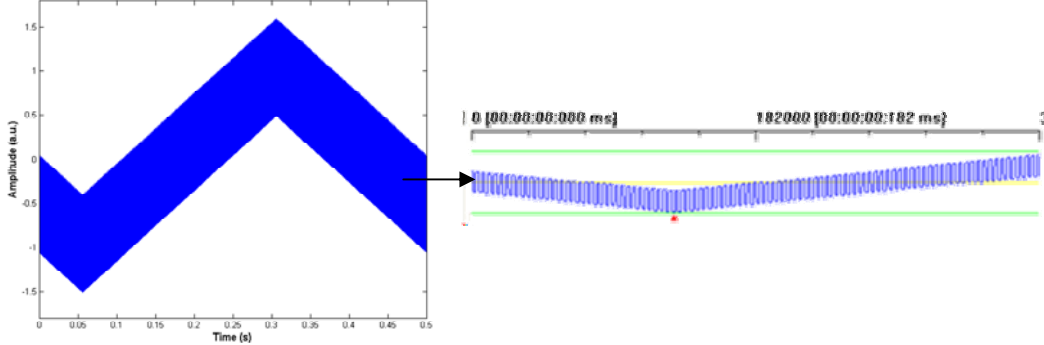


Fig. 2.28. Triangular excitation f_2 applied in conjunction with f_1 for stationary T

This dual-modulation is implemented for a fixed distance d (25 mm) over which T is maintained immobile, as illustrated in Figs. 2.29.

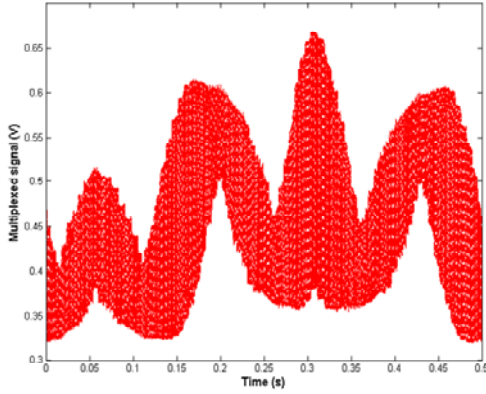


Fig. 2.29(a). Multiplexed V_y and V_x for immobile T

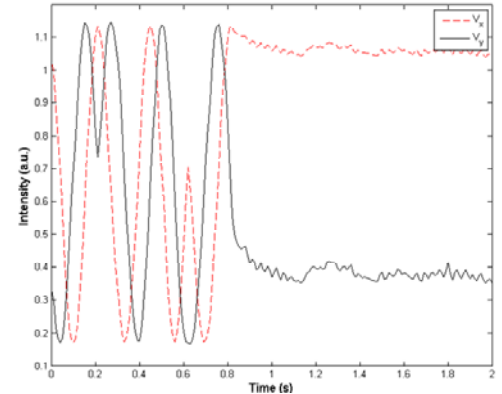


Fig. 2.29(b). Demultiplexed V_y and V_x in quadrature

Demodulation takes into account V_{0x} , V_{mx} , V_{0y} and V_{my} from the demultiplexed interference signals and displacement calculation then proceeds via incremental phase demodulation.

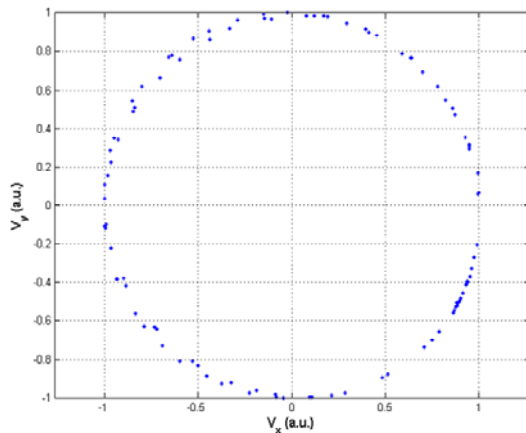


Fig. 2.30. V_y vs V_x for $\geq 2\pi$ trajectory

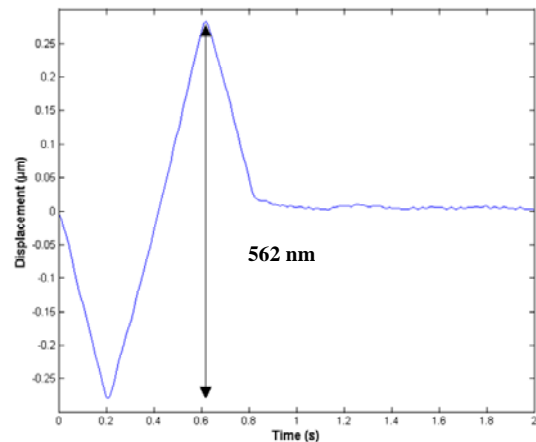


Fig. 2.31. Reference displacement due to dual-modulation

The plot of V_y against V_x results in a perfect circle with the phase trajectory corresponding to the artificially-induced displacement, as demonstrated experimentally in Fig. 2.30. The total phase variation induced by the dual-modulation scheme corresponds to a reference displacement of ~ 562 nm, as plotted in Fig. 2.31.

2.3.2 Demodulation of dual-modulation EFFPI sensor via phase tracking

This section details the phase tracking demodulation technique which is written in C++ and, it is to be strictly noted, has been developed by my colleague, Professor Michel CATTOEN. Software demultiplexing after data acquisition is preferred over hardware analogue demultiplexing.

The first modulation, f_1 , applied at 25 kHz, induces a wavelength variation $\Delta\lambda$ to produce phase quadrature given by

$$\Delta\theta = \theta_2 - \theta_1 = 4\pi nd \left(\frac{1}{\lambda_2} - \frac{1}{\lambda_1} \right) = 4\pi nd \left(\frac{\Delta\lambda}{\lambda_2 \lambda_1} \right) = \frac{\pi}{2} \quad (2.10)$$

This is equivalent to having 2 distinctive interference signals, V_y and V_x , at 2 different wavelengths. For $\Delta\lambda$ relatively small compared to λ_1 and λ_2 , then $\lambda_1 \approx \lambda_2 \approx \lambda$. Hence, using the condition $\Delta\lambda/\lambda^2 = 1/8nd$, (2.8) and (2.9) can then be re-arranged into

$$A_1 = \cos\theta = \frac{V_x - V_{0x}}{V_{mx}} \quad \text{for } A_1 : [-1, +1] \quad (2.11)$$

$$A_2 = \sin\theta = \frac{V_y - V_{0y}}{V_{my}} \quad \text{for } A_2 : [-1, +1] \quad (2.12)$$

The desired phase is next calculated as the arctangent of (2.12) divided by (2.11) and adding a π phase shift to give

$$\theta = \arctan 2 \frac{A_2}{A_1} + \pi \quad \text{for } \theta : [0, 2\pi] \quad (2.13)$$

modulo 2π . Note that the arctan2 function is used for its added advantage of directly computing the signs as well as treating only the real parameters of the input arguments. Due to double reflection, d is now modulo $\lambda/4$ and calculated incrementally from the phase variation from θ_n at point n to θ_{n+1} at point $n+1$ as

$$d = d_{n-1} + \frac{\theta_n - \theta_{n-1}}{F_d} \quad (2.14)$$

where $d_0 = 0$ at $\theta_0 = 0$ and $F_d = 8\pi n/\lambda$ is the displacement factor. Further, an angular correction, otherwise known as phase unwrapping, is provided if the detected phase varies by an angle $>\pi$, given as

$$\begin{aligned} \Delta &= \Delta - 2\pi & \text{if } \Delta > 0, \text{ else} \\ \Delta &= \Delta + 2\pi \end{aligned} \quad (2.15)$$

with $\Delta = \theta_n - \theta_{n-1}$. This correction however implies that θ must not vary by π or more between 2 sampling points since this will lead to errors in determining its positive or negative variation (mathematically $+3\pi/2$ is equivalent to $-\pi/2$). Nevertheless, this condition imposes a limit on the maximum velocity of the object which is given by the Nyquist limit to be $\lambda/8 \times f_s$, with f_s the sampling frequency.

The demodulation first proceeds by normalizing V_y and V_x via

$$\begin{aligned}
V_0 &= \frac{V_{x \max} + V_{x \min}}{2} \\
V_1 &= \frac{V_{x \max} - V_{x \min}}{2} \\
V_2 &= \frac{V_{y \max} + V_{y \min}}{2} \\
V_3 &= \frac{V_{y \max} - V_{y \min}}{2}
\end{aligned} \tag{2.16}$$

where $(V_{x \max} ; V_{x \min})$ and $(V_{y \max} ; V_{y \min})$ represent the minimum and maximum amplitudes of V_x and V_y respectively. The actual normalization stage is then

$$\begin{aligned}
A_x &= \frac{V_x - V_0}{V_1} && \text{for } A_x: [-1, +1] \\
A_y &= \frac{V_y - V_2}{V_3} && \text{for } A_y: [-1, +1]
\end{aligned} \tag{2.17}$$

An illustrated in Fig. 2.32, two pairs of quadrature interference signals from the EFFPI sensor in a differential configuration demodulated to obtain two displacements, **dcal1** (~1.105 μm) and **dcal2** (1.097 μm). Note also that the amplitude difference between **dcal1** and **dcal2** (i.e. **dcal12**) is ~8 nm while the relative difference over the entire duration (~17 mins) is less than 30 nm. This can be attributed to a very slight dissymmetry between the 2 sensor probes (fiber lengths, and misalignment, etc).

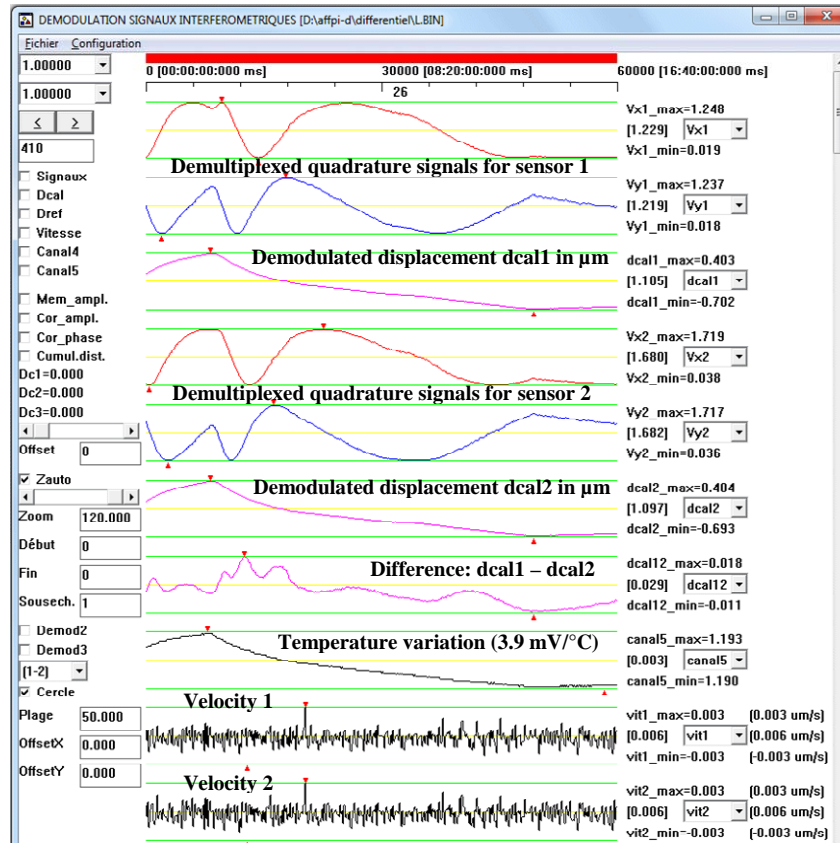


Fig. 2.32. Example program for demodulating 2 sensor in differential configuration

The demodulation program also incorporates functions to correct for quadrature phase errors as well as compensate signal amplitude and source power variations incurred during the modulation process as described in [1,39,40].

2.3.3 Dual-modulation EFFPI sensor characteristics and performance

The laser holder (*Thorlabs* TCLDM9) employed, incorporating a Peltier cooling stage is modified and, together with the DFB-LD are characterized in a precision temperature chamber (*Spirale3* from *CLIMATS*). The EFFPI sensor is set up in a differential configuration for stationary T so that any apparent displacements due only to temperature-induced wavelength shifts are measured, as shown in Figs. 2.33.

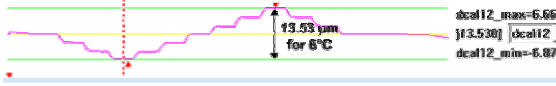


Fig. 2.33(a). Sensor response with TEC deactivated

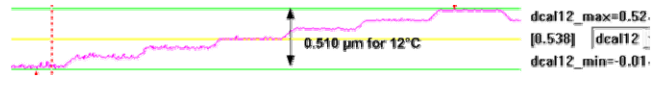


Fig. 2.33(b). Sensor response with TEC activated

Subsequent measurements result in an apparent displacement coefficient of ~ 40 nm/°C and 2.25 $\mu\text{m}/^\circ\text{C}$ with and without temperature regulation respectively. By proportional computation, the temperature sensitivity of the EFFPI sensor is estimated to be better than 0.017°C translating to a displacement error of ~ 13 nm.

While PIF is negligible here, possible errors due to angular orientation of the sensor probe with respect to the target surface could occur and incur an apparent displacement due to the $\cos \alpha$ term described previously in Section 2.2.4. Fig. 2.34 plots the variation of the reflected optical signal under no vibration against the orientation angle, α . No major decrease in signal amplitude is observed over a variation of $\pm 1.0^\circ$ (i.e. within the -3dB range). Now, when the target is set in vibration at constant amplitude, the displacement error measured is < 4 nm vis-à-vis normal incidence for variations of up to $\pm 0.5^\circ$ while an error of < 8 nm is obtained for a $\pm 1.5^\circ$ variation from the normal. This consequently allows the alignment tolerance to be relaxed significantly compared to a typical interferometric system. In addition, the modulation current amplitudes required are halved compared to a single-reflection system for identical d , with the advantage of limiting further perturbation to the DFB-LD [32].

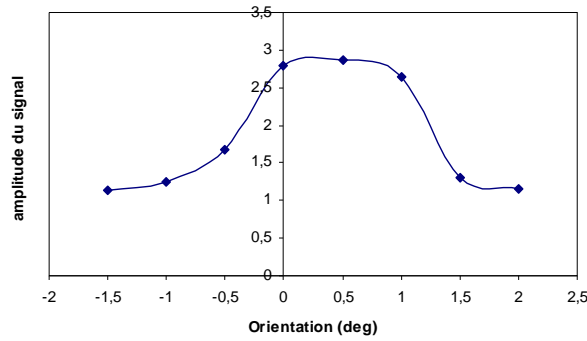


Fig. 2.34. Measured alignment tolerance of modulation-based EFFPI under double reflection

A parameter of paramount importance in terms of performance is the sensor's precision. This is quantified experimentally from the noise level of the EFFPI sensor for an immobile target, as shown in Fig. 2.35. For a 14-bit DAQ system operating at a sampling frequency of $f_s = 1$ MHz with data saved at 1 kHz over a period of ~ 17 mins, the subsequent rms displacement is ~ 2.2 nm over a 10^{-3} –500 Hz range. This value is also considered as corresponding to the absolute precision of the sensor over the investigated bandwidth. The sensor resolution, on the other hand, is estimated to be in the order of several tens of pm from the recorded data.

In the context of geophysics applications, both long-term drifts and the sensitivity of the interferometric probe to temperature variations have to be quantified. The fiber sensor is set up for differential mode measurement since any common-mode "noises" such as parasitic vibration, as well as power, temperature and slight wavelength variations can be reduced.

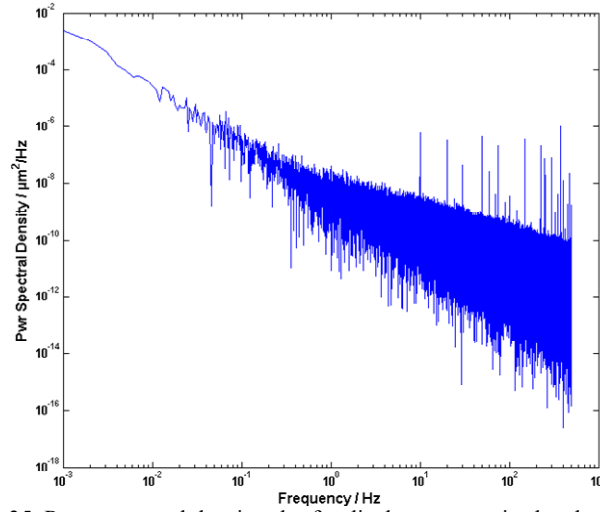


Fig. 2.35. Power spectral density plot for displacement noise level of EFFPI

A simple stainless steel cage system is employed, as illustrated in Fig. 2.36, enabling probes S1 and S2, derived from the same DFB-LD source, to be pointed collinearly at two identical stationary mirrors.

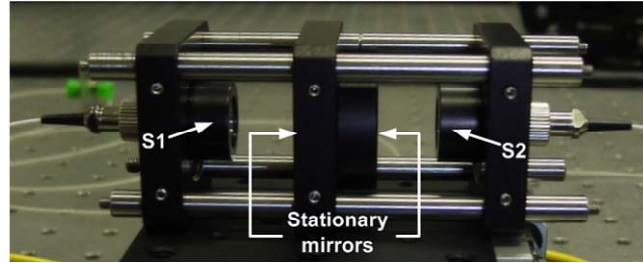


Fig. 2.36. Differential EFFPI sensor configuration mounted in cage system

No discernable displacement excitation is introduced apart from variations of the environmental conditions (vibration noise and temperature variations). As previously, f_s is 1 MHz and data are saved at 1 kHz. The small differential drift displacements (~ 14 nm) as plotted in Fig. 2.37 are induced by the thermal expansion of the cage system and associated mechanical components employed, and are a direct consequence of slow temperature variations in the sensing environment.

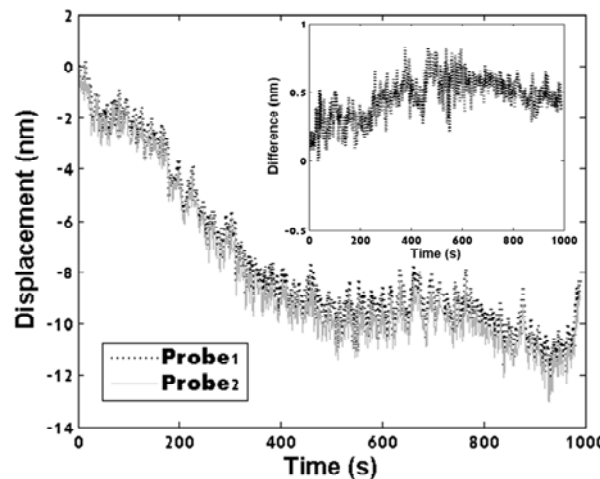


Fig. 2.37. Displacements detected by differential EFFPI probes. Inset illustrates relative difference between S1 and S2

The stability of the sensor system is also demonstrated through the relative difference between S1 and S2 where both probes measure almost identical values, with a maximum difference of <1 nm as shown in the inset of Fig. 2.37 (min. difference is ~ 0.14 nm).

The differential probes are next subjected to a very slow temperature increase in a precision temperature chamber. The subsequent temperature-induced displacements detected by both S1 and S2 over ~ 1 hr at 1 kHz are plotted in Fig. 2.38.

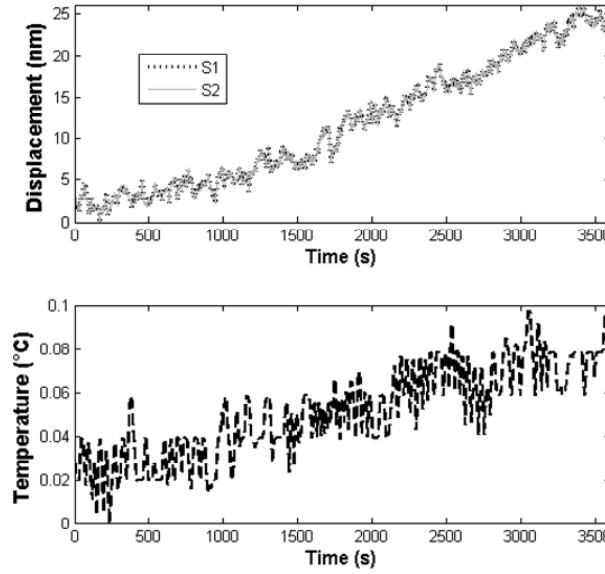


Fig. 2.38. Differential displacements for 0.098°C variation over 1 hr duration (top) and temperature profile (bottom)

A reference temperature probe (sensitivity $\sim 3.9 \text{ mV}/^\circ\text{C}$) is also inserted into the temperature chamber and positioned between S1 and S2 at the base of the mirrors to ensure that the most accurate image of the temperature is recorded. The displacements detected are an identical 25.82 nm for both S1 and S2 for a temperature variation of $\sim 0.1^\circ\text{C}$ over 1 hr. Notwithstanding these absolute values, both displacement profiles replicate the temperature variation, corresponding to the thermal expansion of the metal posts ($\sim 25.6 \text{ nm}$) used in the experiment, which are of stainless steel grade 410 with a thermal expansion coefficient of $\sim 10.5 \mu\text{m}/\text{m}/^\circ\text{C}$. The sensitivity and, more importantly, the stability of the EFFPI thus demonstrate its suitability for long-term metrology.

2.3.4 Applications to displacement measurements

The experimental calibration of the dual-modulation EFFPI sensor is next carried out against reference step movements through a *Polytech PI* PZT stage with a quoted precision of 2 nm (see Fig. 2.25). The *Thorlabs* PDA10CS-EC model *PD* gain is set at 30 dB with an NEP (noise equivalent power) of $1.25 \times 10^{-12} \text{ W}/\sqrt{\text{Hz}}$. The subsequent bandwidth is thereby limited to $\sim 780 \text{ kHz}$ but is considered more than sufficient for the current investigation. The DAQ unit is an *Agilent* U2351 USB device with a maximum sampling frequency of 2 MHz and 4 simultaneous analogue input ports plus 2 digital I/O ports.

The displacements measured by the fiber sensor against the "reference" PZT movement from 0.002 – $5 \mu\text{m}$ are plotted in Fig. 2.39. These are found to be well within the 2 nm precision of both devices, i.e. $\sim 2 \text{ nm}$, and demonstrate a very high linear correlation (of almost 1) with the PZT. The dashed line plots an ideal displacement ratio of 1 between the 2 measurements, again demonstrating the accuracy of the EFFPI sensor where the deviation from true displacement is actually only $\sim 1 \text{ nm}$ by considering the vertical error bar at each measurement point. Further, the inset shows the relative error between the 2 sensors being in the low nm range. In absolute terms, the errors are less than 1.5 nm up to the $2 \mu\text{m}$ displacement range. Between 2 and $5 \mu\text{m}$, the discrepancies between the 2 devices are ~ 19.9 and 46.2 nm , corresponding to errors of $\sim 0.99\%$ and 0.92% , respectively. This is attributed to the non-linear response of the reference PZT at these displacement points.

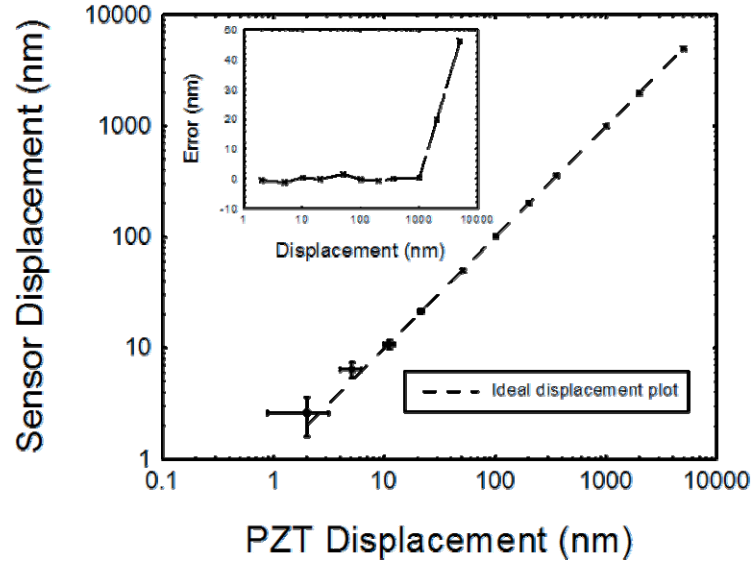


Fig. 2.39. EFFPI displacements against PZT movement over 0.002–5 μm range. Vertical bars : EFFPI precision (~ 2 nm); Horizontal bars: PZT precision (~ 2 nm)

An experimental calibration is also carried out to validate the EFFPI sensor performance under dynamic excitation. Fig. 2.40 plots the displacement measured for a squarewave excitation at ~ 5 μm at 10 Hz. The interference signals are recorded at 25 kHz from a sampling frequency of 1 MHz.

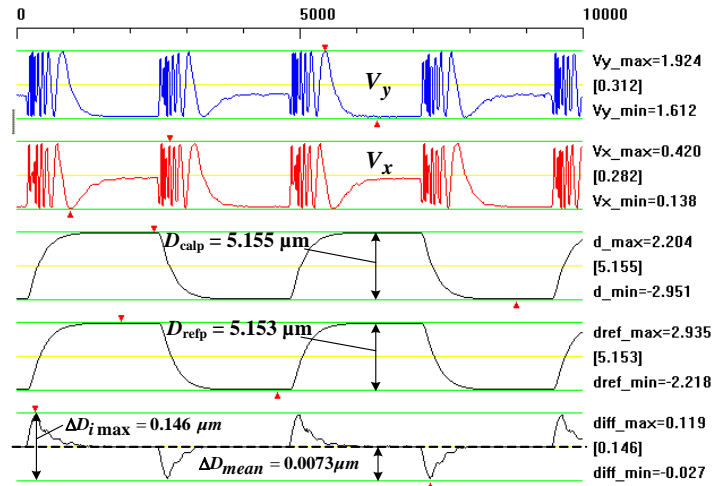


Fig. 2.40. Comparison of EFFPI and PZT displacement amplitudes under squarewave excitation at 10 Hz

The measured peak-to-peak displacement is ~ 5.155 μm while that of the reference sensor (PZT) is ~ 5.153 μm . This translates into an error of 2 nm (or ~ 0.04 %), which is coherent with earlier analysis on its performance and serves to validate the EFFPI sensor's precision.

2.3.5 Applications to geophysics

The need for new instruments in geophysics is motivated by the absence of a series of sensitive devices capable of monitoring earth strains within a seismic zone extending from the minute to 8 year period, as illustrated in Fig. 2.41. These strains are generally a consequence of naturally-occurring events such as earthquakes and volcanic eruptions as well as man-made circumstances such as artificial loading of the earth's surface, the examples of which are underground gas storage, subterranean mine and tunnel drilling, hydrocarbon exploration via ground fracture techniques and underground nuclear tests. The development of the dual-modulation EFFPI sensor tailored to geophysics instrumentation is thus a complement to existing instruments to provide cover for the "unknown zone" where important information can be obtained.

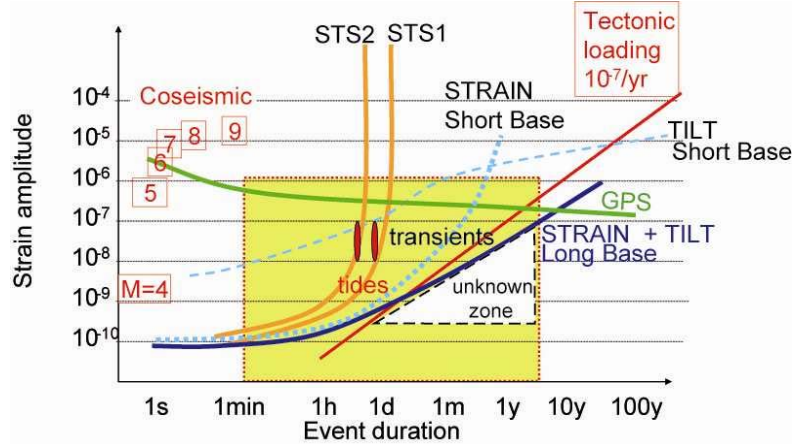


Fig. 2.41. Instruments currently employed for measuring earth strains with unknown zone (STS1 and STS2: 3-axis Streckeisen broadband seismometers; TILT: tiltmeters; STRAIN: strainmeters)

In the context of the ANR RiskNat project, three distinct novel instruments have been developed, namely a fiber optic-based long baseline tiltmeter (ILB-LINES), a fiber-based borehole tiltmeter (IF-LINES) and a fiber-based seismometer (SISMO-LINES). These instruments are expected to cover an operational zone extending from the low 10^{-3} to ~ 200 Hz range together with a relatively long operating lifetime (>1 year).

2.3.5.1 Fiber optic long baseline tiltmeter (ILB-LINES)

ILB-LINES is based on a set of hydrostatic communicating vases linked by water tubes, the operating principle of which is shown schematically in Fig. 2.42.

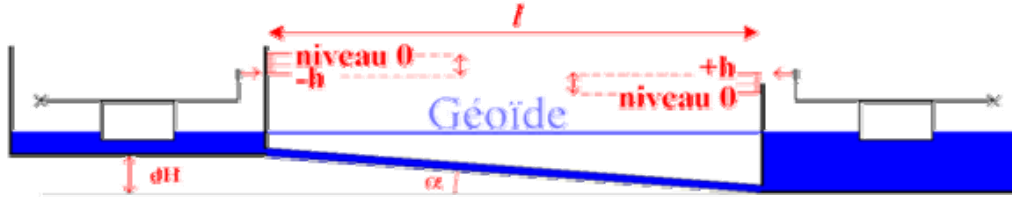


Fig. 2.42. Operating principles of long baseline tiltmeter

The resulting tilt angle induced by any ground movement over a baseline, l , between two vases is then given by simple geometry as

$$\sin \alpha \approx \alpha = \frac{dH}{l} = \frac{2h}{l} \quad (2.18)$$

Hence, the resolution of the tilt increases proportionally as the baseline. The EFFPI sensor is integrated into the all-glass tiltmeter under a differential configuration to reduce common-mode perturbations, as illustrated schematically in Fig. 2.43(a). Two silvered mirrors are fused onto the top end of a rigid silica rod and positioned in the middle of the differential probes as shown in Fig. 2.43(b). A reference LVDT sensor with a precision of ~ 10 nm is also installed in the same vase. The entire set-up is calibrated against known variations in liquid levels to locate the equilibrium position of the mirrors with respect to the differential probes.

ILB-LINES is next deployed to the LSBB (Laboratoire Souterrain à Bas Bruit) facilities in Rustrel (Vaucluse, South-East France) and has a 150 m baseline along the North-South direction. One of the longest in the world, it is also the longest tiltmeter system ever deployed in Europe.

ILB-LINES has been in operation since March 2012 and, notwithstanding a few electricity cut-offs, has been used to detect very slow minute ground tilts and various earthquakes. The benchmark of a sensor system in geophysics is the ability to measure cyclic earth tides, hence enabling one to characterize the device's sensitivity.

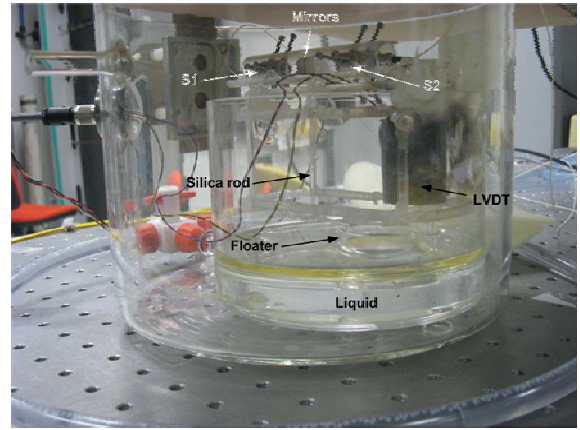
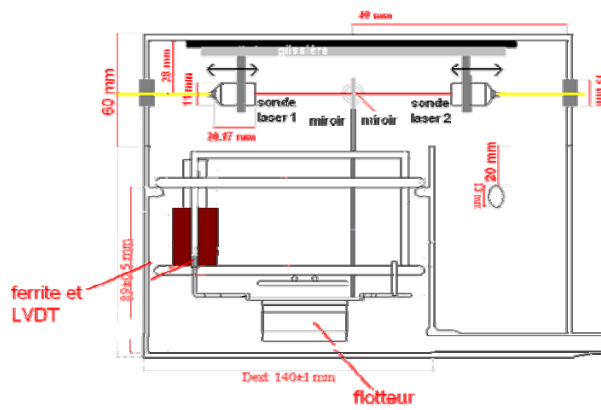


Fig. 2.43. (a) Schematic of ILB-LINES design and (b) positioning of differential probes, S1 and S2

The tide amplitudes are of the order of 10^{-7} radians and are cyclic over 12-hr periods, as shown in Fig. 2.44(a). Further, the high quality of the EFFPI sensor measurement is also evident from the noise level measured, implying that very small tilt movements can be subsequently resolved. The difference in tilt from both EFFPI and LVDT measurements is plotted in Fig. 2.44(b) and is within the low 10^{-11} radian range over a 36-hr observation period.

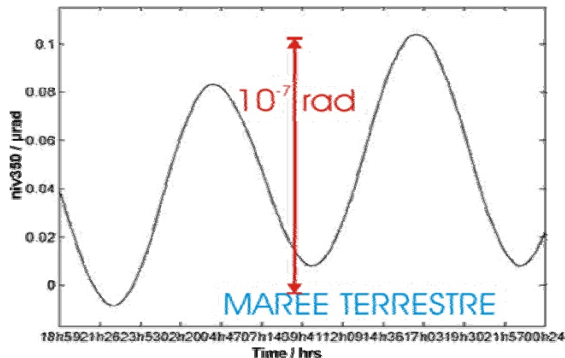


Fig. 2.44(a). Earth tides detected by EFFPI sensor of ILB LINES

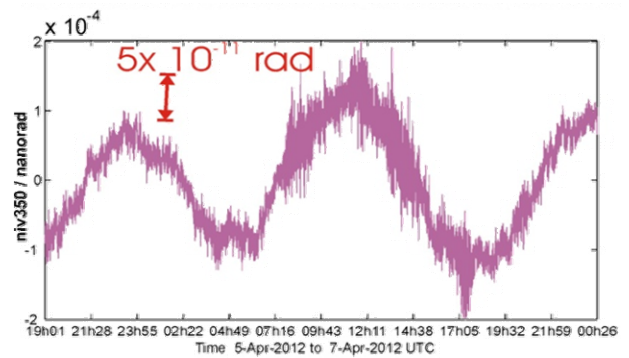


Fig. 2.44(b). Difference between LDVT and EFFPI measurements over 36 hrs

The sensitivity of ILB-LINES to minute tilts in the earth's movement is demonstrated in Fig. 2.45 during the Sumatra earthquake on 11 April 2012.

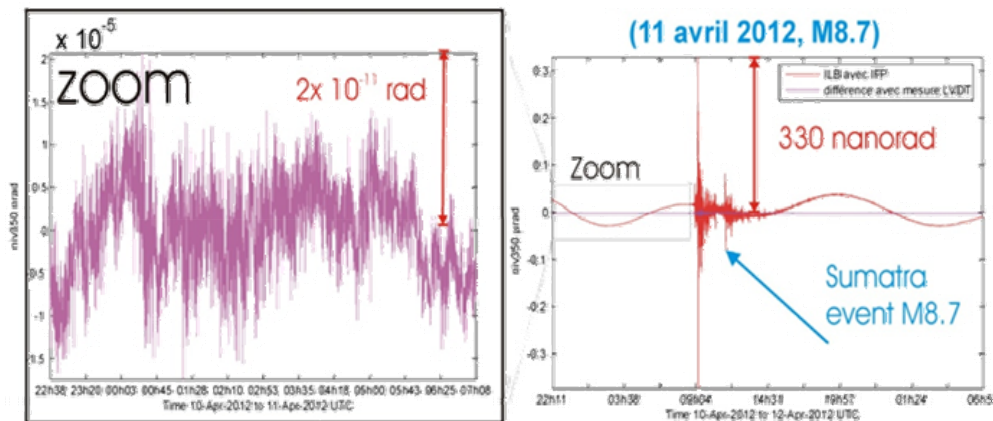


Fig. 2.45. Tilt measured by ILB-LINES during M8.7 Sumatra earthquake. Zoom shows the difference between LVDT and EFFPI of 0.2% over 9 hr period

Comparison of both LDVT and EFFPI measurements shows that just before the quake, the background noise is resolved to better than 2×10^{-11} rad (see zoom) over a 9-hr period, and their difference is $<0.2\%$. At the occurrence of the magnitude 8.7 (M8.7) quake, which translates into a 330 nrad tilt amplitude, both measurements are almost identical. A difference of only 8 nrad (or $\sim 3\%$) is observed and may be explained by the LVDT sensor being not compensated for

various noise effects (e.g. its temperature sensitivity $\sim 300 \text{ nm}/^\circ\text{C}$). Note also that the earthquake event is superimposed onto the periodic earth tide oscillations.

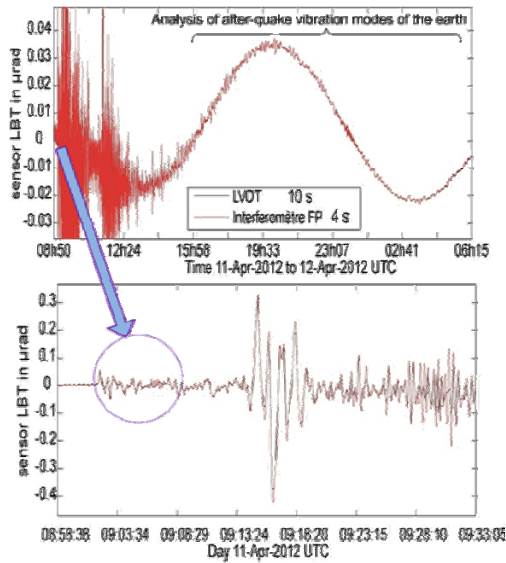


Fig. 2.46. Before and after-quake fine details from ILB-LINES measurements

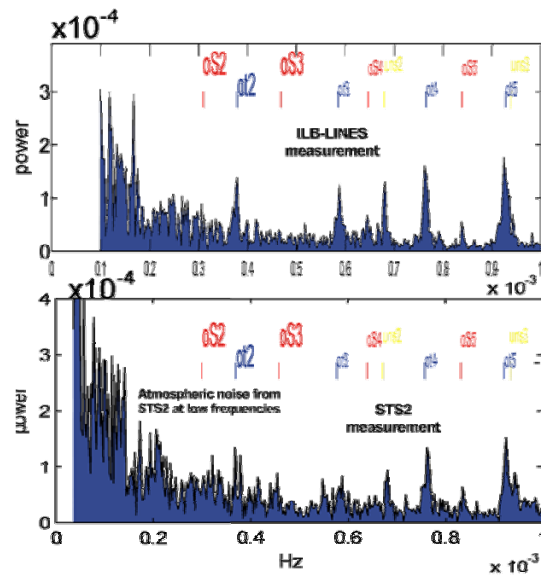


Fig. 2.47. Earth's oscillation modes induced by Sumatra quake from ILB-LINES and STS2 (oS: spheroidal modes; oT: Toroidal modes)

Figure 2.46 demonstrates the capability of ILB-LINES to resolve minute tilt details. Just before the quake, both LVDT and EFFPI measurements are identical and constitute the background noise of the earth's movement. During the quake, 2 distinctive groups of vibration can be observed, corresponding to the primary and secondary quakes respectively, together with smaller-amplitude oscillations of earth's movement, illustrating the μrad resolution achieved by ILB-LINES. A further comparison is next carried out with the reference wide-bandwidth Streckeisen STS2 3-axis seismometer. Both measurements are illustrated in Fig. 2.47.

Analysis of data from the Sumatra event shows ILB-LINES to be relatively more sensitive to the earth's after-quake oscillatory modes via its stronger power spectral density (PSD). In addition, towards the low-frequency region (i.e. $< 0.4 \times 10^{-3} \text{ Hz}$), the ILB-LINES signals are less influenced by atmospheric noise compared to those from the STS2.

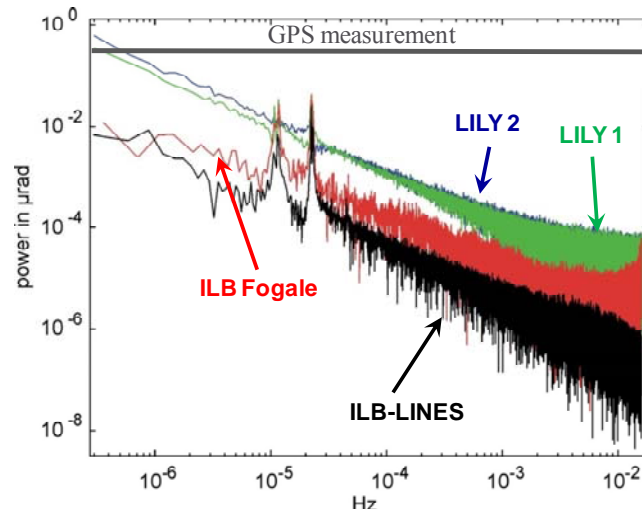


Fig. 2.48. Noise power from both ILB-LINES, FOGALE HLS, LILY borehole tiltmeter from Jewell, Inc & GPS

A final comparison is carried out with a commercial hydrostatic leveling sensor (HLS) from FOGALE, as shown in Fig. 2.48, which illustrates the noise level from each instrument over a bandwidth of 10^{-6} – 10^{-2} Hz . The PSD plot clearly shows the superior performance of ILB-LINES from $\sim 10^{-5} \text{ Hz}$ onwards which is ~ 10 times better than that of the FOGALE HLS. Also, from $\sim 6 \times 10^{-3} \text{ Hz}$ onwards, ILB-LINES is almost 100 times better in precision. Two further

curves are included for comparison purposes to illustrate that, over the entire bandwidth analyzed, ILB-LINES is 100–1000 times better in precision than either LILY (commercial borehole tiltmeter from Jewell, Inc) or GPS-based systems. The results obtained demonstrate the potential of ILB-LINES to be exploited in an industrial context.

2.3.5.2 Fiber optic borehole tiltmeter (IF-LINES)

IF-LINES is designed to measure displacements in 3 directions along a same plane thus providing redundancy on the position with a further advantage of enabling a 2D movement of the ground to be reconstructed. IF-LINES is based on a tri-axial measurement of a displacing mass, as illustrated schematically in Fig. 2.49. Its pendulum system is an equilateral triangular form allowing 3 optical mirrors to be mounted, spaced at 120° apart. The sensing beams are guided to these mirrors via a set of right-angle optical reflectors (see Fig. 2.50).

IF-LINES is designed so that the sum of the 3 displacements, $d_1 + d_2 + d_3 = \text{constant}$ thus providing redundancy to compensate for atmospheric noises and eliminate system drifts. The superstructure of IF-LINES is inserted into a second larger boro-silicate tubing serving as the support. Before sealing, a MEMS-based 2-axis positioning system is attached onto the top of the former device to enable orienting IF-LINES during down-hole installation.

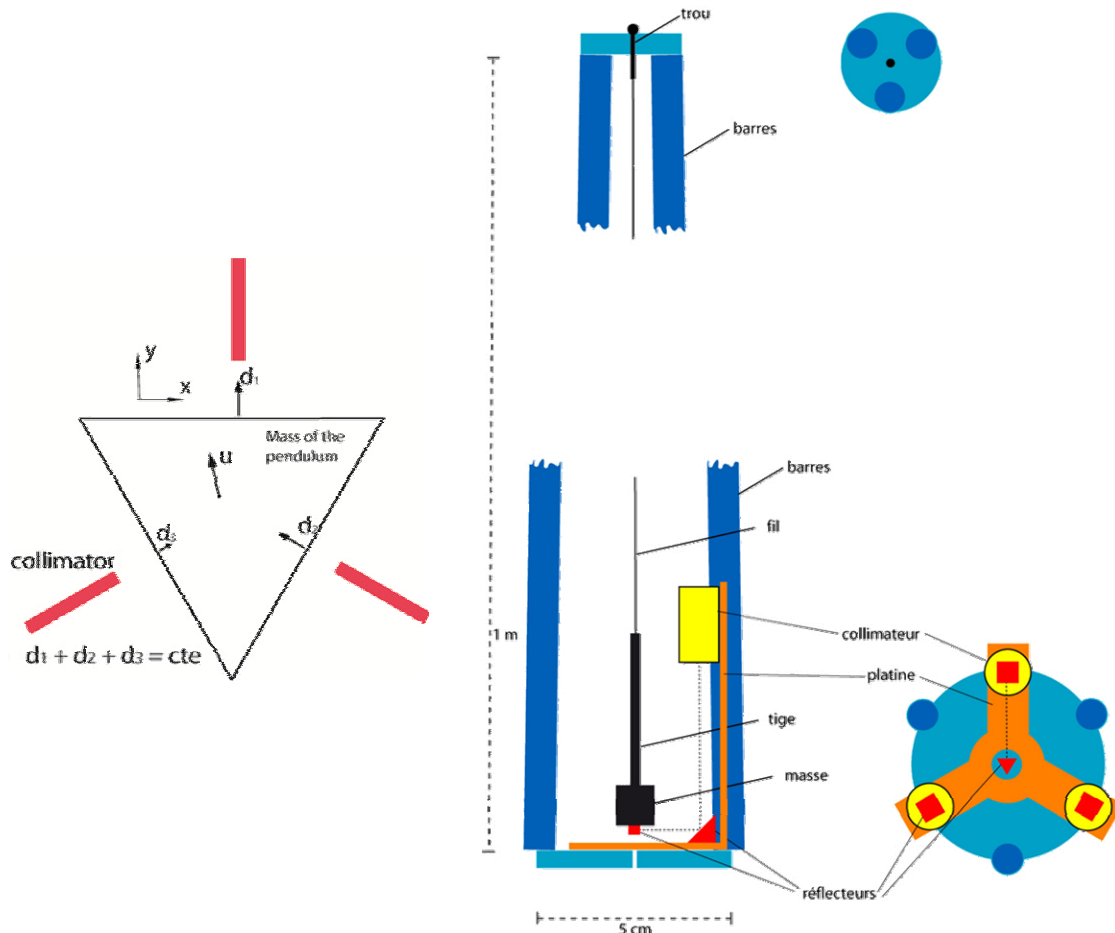


Fig. 2.49. Tri-axial measurement of displacement, d_1 , d_2 and d_3 in IF-LINES

Fig. 2.50. Pendulum system used in IF-LINES with reflectors to guide sensing beams to target surface

IF-LINES has also been deployed since March 2012 at the LSBB test site along the N–S line and is positioned in a borehole ~ 1 m deep under ~ 400 m of rocks at the extreme end of the test tunnel. The instrument-ground coupling is ensured by inserting tiny silica spheres between the instrument's outer surface and the inner wall of the borehole. For remote sensing, IF-LINES is connected via 3 identical 270 m long fibers to the DFB-LD and PDs situated at the tunnel entrance. IF-LINES is illustrated in Fig. 2.51 just before its insertion into the borehole.

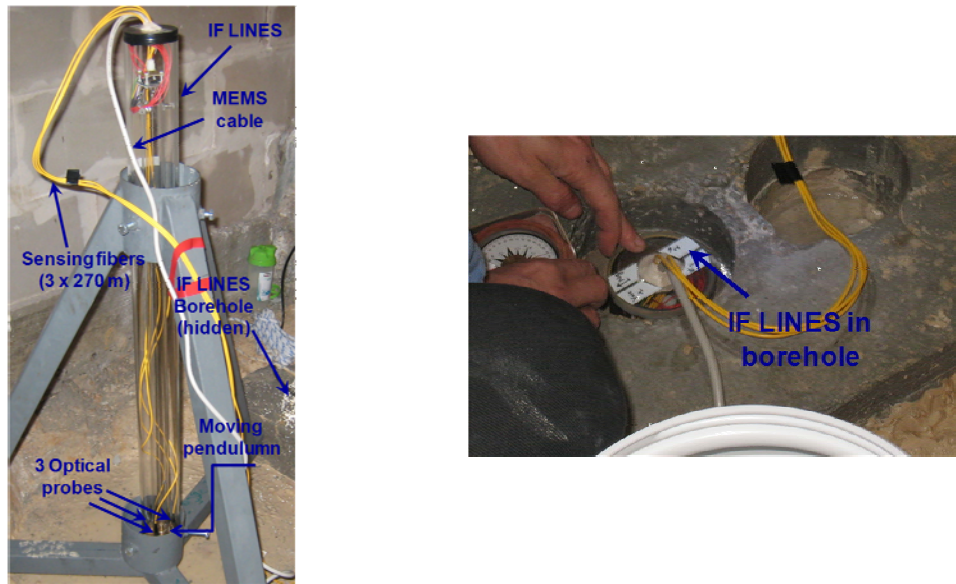


Fig. 2.51. IF-LINES and its insertion into borehole at LSBB test site

The characteristic response of IF-LINES to earth tides is shown in Fig. 2.52. These have amplitudes of 50–130 nm over 12-hr periods and can be measured to nm range resolution as illustrated in the bottom figure. The corresponding tilt resolution is ~ 1 nrad.

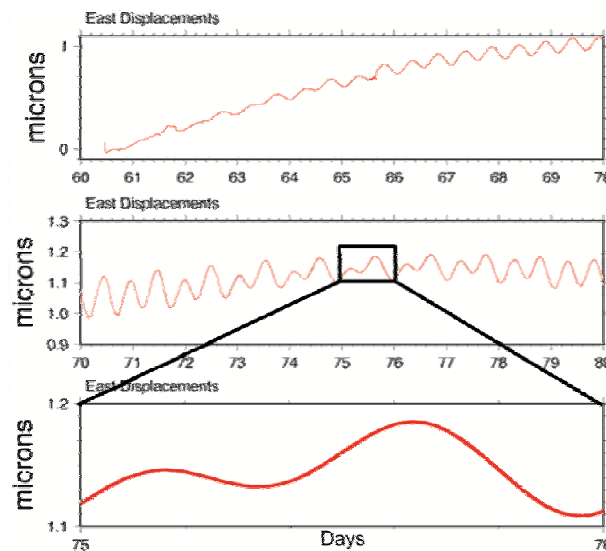


Fig. 2.52. IF-LINES earth tide measurements over 10 day period. Bottom figure demonstrates instrumental resolution in the nm order

The tri-axial measurement capability of IF-LINES enables a 2D observation of earth tides, as illustrated in Fig. 2.53, whose influence induces the instrument to trace a North–South direction superimposed onto which are the earth tides. This corresponds to the geographical orientation of the instrument with its first axis pointed due North.

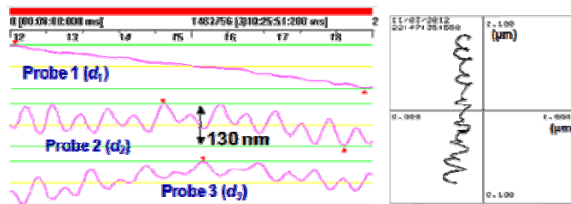


Fig. 2.53. IF-LINES tri-axial displacements from earth tides

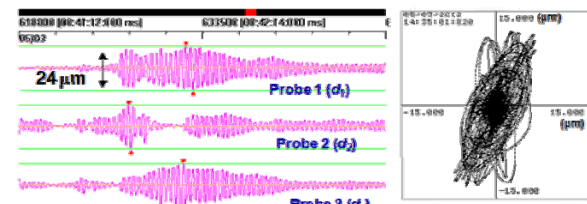


Fig. 2.54. IF-LINES tri-axial displacements from Argentina earthquake on 2 March 2012

The typical response of IF-LINES to the M6.1 Argentina earthquake on 5 March 2012 is next plotted in Fig. 2.54, in which the characteristic N–S "natural" response is slightly shifted

towards the N–E direction on the 2D plane. Further, the detected amplitudes are ~ 180 times that induced by earth tides. To validate the earlier hypothesis on 3-axis redundancy, the displacement sum is analyzed during a quake event as plotted in Fig. 2.55.

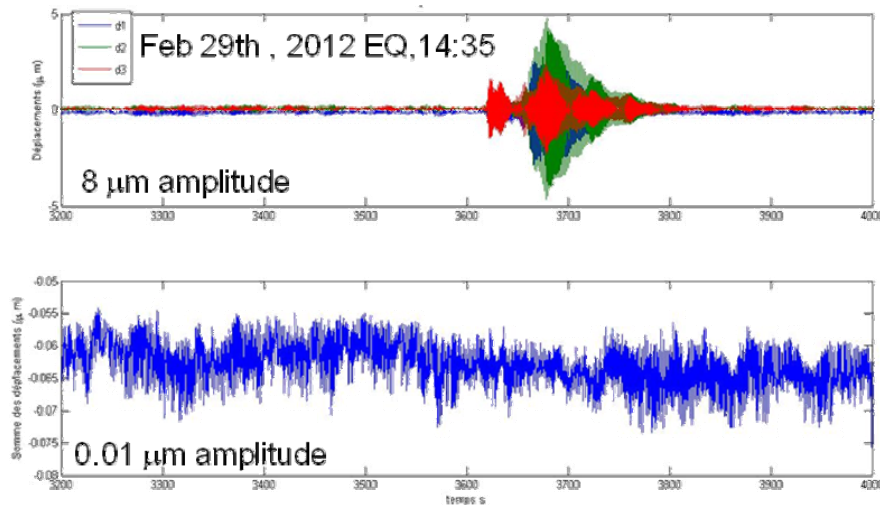


Fig. 2.55. Validation of displacement redundancy on d_1 , d_2 and d_3 during Japan earthquake on 29 Feb 2012.
Top: tri-axial displacements; Bottom: displacement sum

This event corresponds to the M5.8 Japan earthquake on 29 Feb 2012, lasting ~ 3.5 mins. The before and after-quake characteristics of IF-LINES have been analyzed over 800 secs (~ 13.3 mins). The maximum amplitude induced is $\sim 8 \mu\text{m}$, as detected by d_2 . From the redundancy calculation, the displacement sum averages out to less than 10 nm in amplitude and is a critical parameter to validate the operation of IF-LINES. A further validation means is also carried out in comparison with the Jewell LILY borehole tiltmeter over a period of more than 21 days, as plotted in Fig. 2.56.

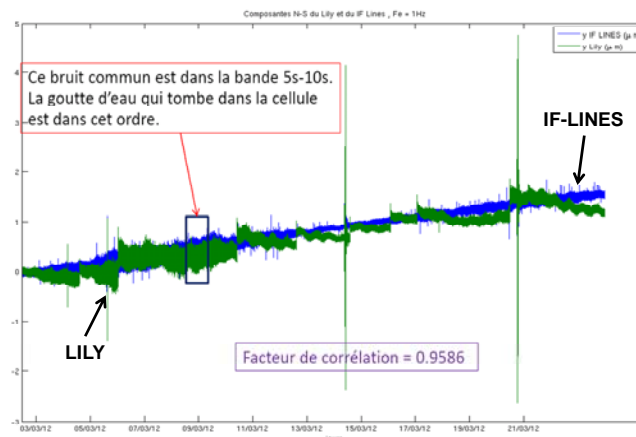


Fig. 2.56. Response of N–S components of IF-LINES and LILY to tunnel water precipitation: multiple discontinuities from LILY contribute to phase hopping and large offsets

LILY is installed in a borehole next to IF-LINES and similarly oriented. Both instrument outputs are comparable in terms of the displacements induced by the ground tilt along N–S, with a correlation factor of ~ 0.959 . The displacements within the rectangle represent a common noise level which is identical in both instruments and correspond to minute tilts induced by water droplets dripping from the tunnel ceiling. The most obvious difference, however, between IF-LINES and LILY lies in the multiple discontinuities from the latter instrument leading to significant phase hopping and large offsets over the entire duration.

A final investigation concerns the sensibility of IF-LINES to external parasites such as pressure variations which can typically occur in geophysics applications. The test tunnel pressure is measured over a 3-week period and plotted in Fig. 2.57 together with the E–W and N–S components of both IF-LINES and LILY.

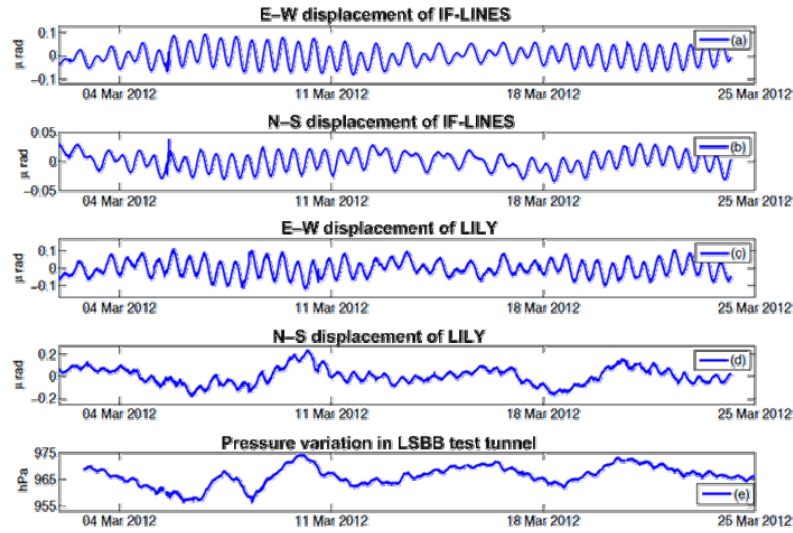


Fig. 2.57. Displacements from E–W and N–S components of IF-LINES and LILY versus pressure variation in LSBB test tunnel.

Both instruments are oriented along the tunnel's principal axis (i.e. N–S direction). Any pressure variation will thus induce a tilt movement in this direction. While IF-LINES is relatively insensitive to this parasitic disturbance, LILY is clearly affected as reflected by its N–S component which highly corresponds to the pressure profile. The E–W components of both IF-LINES and LILY, on the other hand, are relatively insensitive to pressure variations.

2.3.5.3 Fiber optic seismometer (SISMO-LINES)

SISMO-LINES, whose operating principle is the interrogation of a mobile mass of a 2Hz L22 Sercel seismometer with the modulation-based EFFPI, is illustrated in Figs. 2.58.

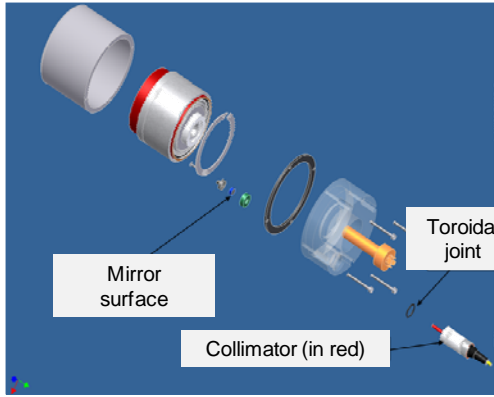


Fig. 2.58(a). Exploded view of SISMO-LINES based on L22 seismometer with collimator representing EFFPI

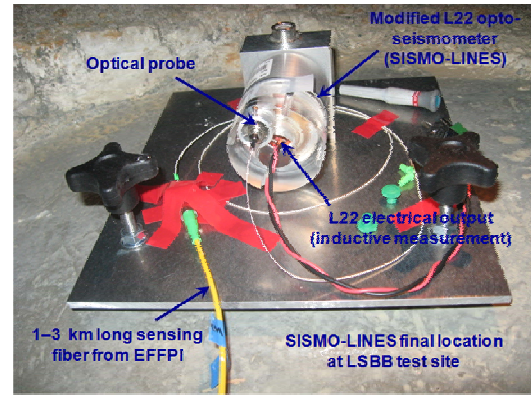


Fig. 2.58(b). SISMO-LINES deployment at LSBB test site with 1–3 km fiber for remote sensing

The L22 device is modified to integrate the optical probe of the EFFPI whose sensing beam is guided to an optical mirror secured to the moving mass. The electrical output (inductive measurement) from the device is employed as reference for initial calibration purposes.

The response from SISMO-LINES and the L22 seismometer to random shocks are plotted in Fig. 2.59. A difference of <2% in peak-peak velocity is obtained between the 2 instruments and is attributed to the mechanical friction between the mobile mass and the inductive rod. Both sensors, however, detect the same number of shocks with identical velocity profiles of similar amplitudes. Initial requirements specify an operating range of 2–200 Hz but SISMO-LINES can be operated up to 5 kHz which is within the specifications of the best seismometer available (the Streckeisen STS2 broadband sensor). An analysis of the optical instrumental noise under earth's natural movement (i.e., no quake) results in a precision of less than 2 nm over a 2 Hz–5 kHz bandwidth (see Fig. 2.60), corresponding to previous estimation for the EFFPI sensor.

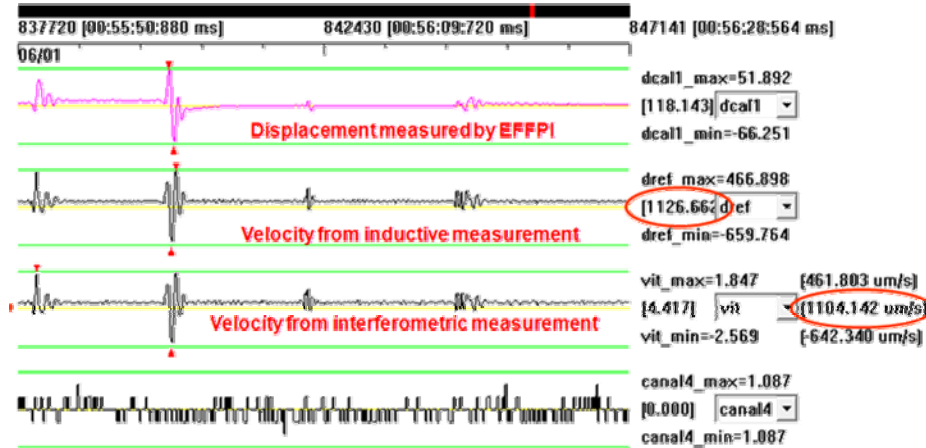


Fig. 2.59. Comparison of optical and inductive measurements from SISMO-LINES: velocity in $\mu\text{m/s}$

Further, over a 5000-sec duration, the displacement resolution achievable is better than 70 pm (right). Another calibration phase for SISMO-LINES lies in its ability to detect low-frequency earth-tides, as shown in Fig. 2.61 over an observation period of >270 hrs where their cyclic (~ 12 hrs) profile can clearly be distinguished.

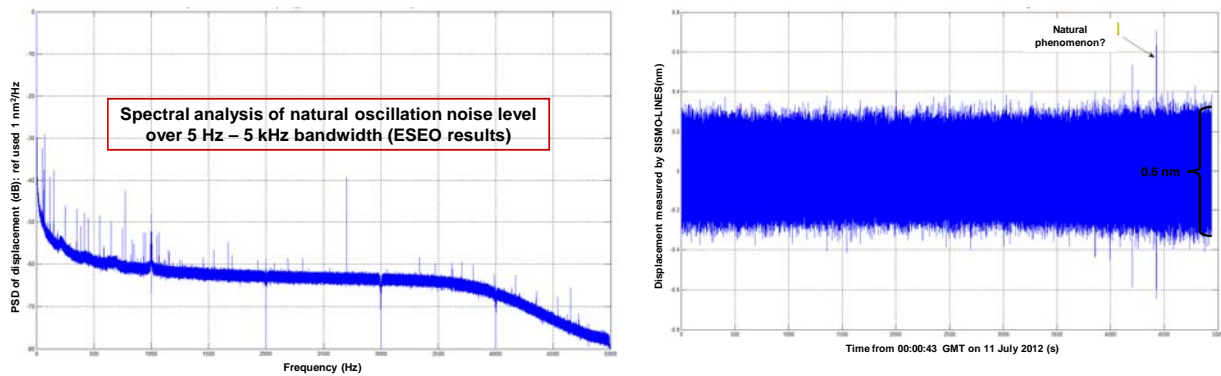


Fig. 2.60. Left: spectral analysis of SISMO-LINES noise level for natural vibrations over 0–5 kHz bandwidth (< 2 nm precision); Right: 0.6 nm displacement amplitudes with 70 pm resolution over 5000 sec period

Nevertheless, the detected tide amplitudes (max amplitude ~ 15 nm) are considerably smaller than those from both ILB-LINES and IF-LINES, and can be attributed to the fact that the mobile mass axis is not collinear with the ground movement (i.e. not perpendicular).

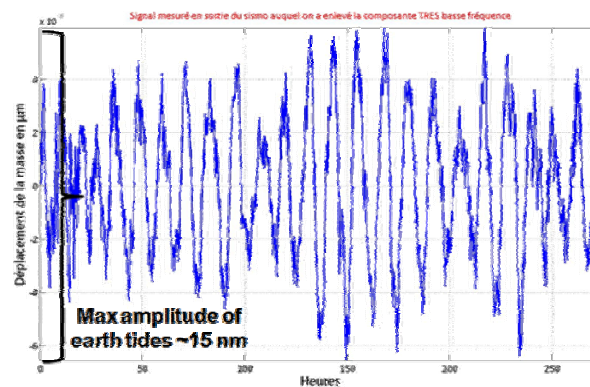


Fig. 2.61. Earth tides measured by SISMO-LINES over 270 hrs observation period

The final calibration stage of SISMO-LINES is a comparison with the STS2 seismometer during the M8.7 Sumatra quake on 11 Apr 2012 (Figs. 2.62). The accelerations detected by both instruments are of highly similar profile and amplitudes throughout the entire quake event (Fig. 2.62(a)). Both the STS2 and SISMO-LINES are also able to simultaneously detect low-amplitude rumblings just before the actual quake.

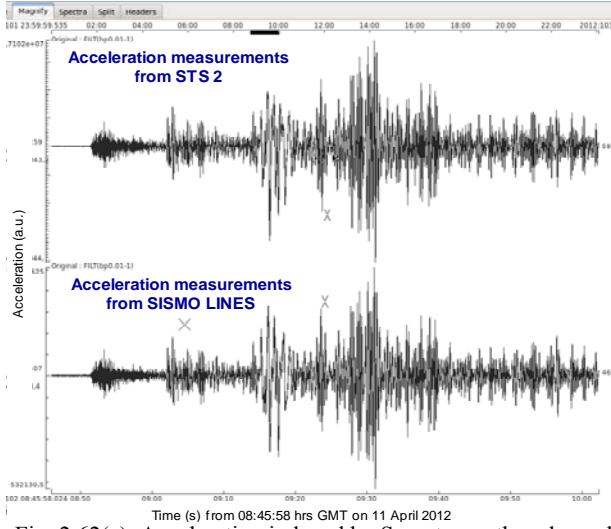


Fig. 2.62(a). Acceleration induced by Sumatra earthquake and detected by both STS2 and SISMO-LINES

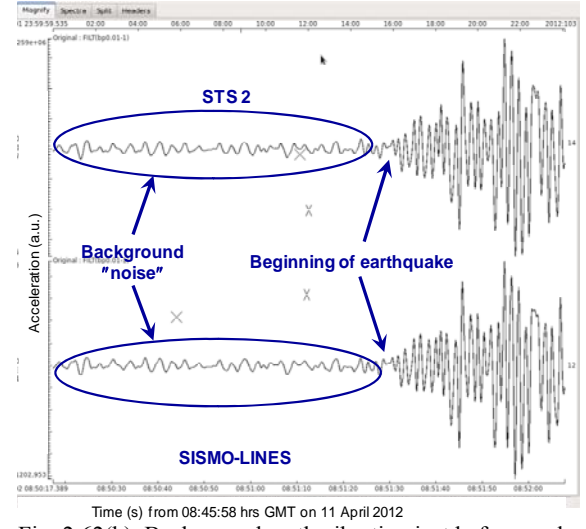


Fig. 2.62(b). Background earth vibration just before quake event: both STS2 and SISMO-LINES are identical

In addition, SISMO-LINES is able to measure highly-resolved details of the induced acceleration just before the quake with respect to the STS2 device, as demonstrated in Fig. 2.62(b). It is thus comparable to the reference STS2 seismometer while suffering very little or no electrical noise, a major advantage of using long optical fibers. In this project, both 1 km and 3 km fibers are tested successfully.

2.4 Conclusions and Perspectives

Two variants of the EFFPI sensor have been developed and analyzed. These are subsequently tested for vibration and displacement measurements with relatively high precision and good stability.

The polarization-based EFFPI is highly suitable for very fast displacement measurements as it does not employ any modulation scheme on the laser source. It thus has a very high bandwidth, the limit of which is dependent on that of the photodetectors and the temporal coherence of the LD employed. In addition, depending on the DFB-LD coherence length, the target can be positioned at a relatively long working distance away from the optical probe. Although not mentioned in this manuscript, we have worked at a distance of >1.80 m using a collimated beam from the DFB-LD and the displacement values obtained are identical to those obtained at near field. By exploiting the modified fringe-counting demodulation technique, the interferometer has also been demonstrated to be sufficiently robust for tracking displacements of various profiles. Further, the use of a polarization-based dual optical cavity enables both the displacement amplitudes and direction to be determined with a relatively good precision ($\lambda/64$) over a large dynamic range. However, the minimum detectable displacement of the sensor is ultimately limited to only $\lambda/2$. There is, however, a major disadvantage in that the polarization stability cannot be guaranteed over the long-term unless the sensing fiber can be isolated from environmental perturbation, in particular temperature variations and vibration. Polarization control via polarization scrambler or active systems can be used to maintain suitable visibilities in the quadrature interference signals. Another possible solution is the use of polarization-maintaining fibers and components. Although the use of such materials can reduce the cost-effectiveness of the sensor, this is perhaps a favorable compromise if the "passivity" of the sensor system is a priority. In the work on the dual-cavity EFFPI sensor, efforts have been made to ensure that polarization state degradation is not produced during experimental measurements. In addition, with the experimental set-up employed, there is an unlikelihood of complete simultaneous extinction of the quadrature pair. Hence, interference signals are always present for the sensor to be exploitable.

In terms of application domains, the dual-cavity EFFPI sensor can be employed for high-speed measurements such as in the study of impacts on materials and shock-waves generated after a high-velocity impact, which are short-lived phenomena. Another potential use of this sensor is in gravitational wave measurements in which a mass released from a pre-determined height is tracked through its trajectory to calculate its gravity profile. This is another ephemeral phenomenon lasting several ms.

The modulation-based EFFPI has been successfully integrated for applications in geophysics and 3 fiber-geophysics instruments have been deployed at the LSBB test-site for this purpose. The specifications achieved have enabled the system to be coupled to 2 long baseline tiltmeters (ILB-LINES), a borehole tiltmeter (IF-LINES) and a seismometer (SISMO-LINES) for long-term monitoring of earth tilts as well as seismic activities (since March 2012). The instruments developed in the context of the LINES project have equaled or even out-performed the current generation of "conventional" instruments employed in geophysics in terms of precision, instrumental resolution and sensibility. They are also demonstrated to be highly suitable for long-term deployment at natural sites. Although serious technical failures have been not been encountered, there are occasional electricity cut-offs which could have affected the continuity of the desired measurements. Preventive measures have been planned for such moments: use of uninterrupted power supplies to drive the PCs, DAQs, laser driver units and detectors. This, however, obviously leads to one major inconvenience in the current crop of LINES instruments: that of autonomous operation. It is therefore imperative to modify and further develop these instruments, in particular, the EFFPI sensor to operate on 12 or 24 V power supplies typically provided by batteries and/or solar cells for fully autonomous operation in remote zones (for example the Chilean desert, offshore sites, as well as various petrochemical prospection zones). Nonetheless, the modulation-based EFFPI has been terrain-tested for very slowly-varying movements. Currently limited to relative displacement measurements, a potential evolution would be to orientate the modulation-based EFFPI sensor into an instrument for absolute measurements (i.e. distance). This could be carried out by exploiting the synthetic wavelength generated during the modulation scheme in conjunction with the inherent double wavelengths to obtain approximate distance information using the synthetic wavelength for integer fringes which can then be completed with interferometric precision using the latter wavelengths for fractional fringes.

The potential of the instruments has been clearly demonstrated during the course of the research project. Note also that 3 patent applications with PCT extension are currently pending for the EFFPI sensor, ILB-LINES and IF-LINES, respectively. The next possible stage in R&D will be to implement a fully-distributed sensing scheme incorporating these instruments to facilitate their deployment in a sensor network. The ambition of such a scheme is to provide reliable and very large geographical coverage for natural risk monitoring, prediction and prevention. Negotiations are currently ongoing with the CERN to deploy an initial series of 3 prototype ILB-LINES for accelerator alignment. The future needs of the CERN will concern a minimum of 120 ILB-LINES systems and up to ~1000 units upon completion of all the particle accelerators. Further, discussions are also ongoing with FOGALE, a major industrial player in optical metrology, and ISP System for the technology transfer of the modulation-based EFFPI system in terms of future development and its commercial exploitation.

References

- [1] S. Pullteap, *Development of an extrinsic dual-cavity fiber Fabry-Perot interferometer: Applications to periodic and non-periodic vibration measurements*, PhD Thesis, INPT, Dec 2008
- [2] A. G. Ambekar, *Mechanical Vibrations and Noise Engineering*, Prentice-Hall of India, 2006
- [3] J. P. Den Hartog, *Mechanical Vibrations*, Dover Publications, 1985
- [4] P. E. Sanders, Advanced optical fibers for geophysical sensing applications, CLEO-QELS Conference, pp. 1-2, E-ISBN 978-1-55752-890-2, San Jose (USA), 16-21 May, 2010
- [5] B. Culshaw, *Optical Fiber Sensing and Signal Processing*, Peter Peregrinus Ltd., 1984
- [6] N. Singh, S. C. Jain, A. K. Aggarwal and R. P. Bajpai, "Development and experiment studies of fibre optic extrinsic Fabry-Pérot interferometric sensor for measurement of strain in structures", *Current Science*, vol. 86, no. 2, pp. 309-314, 2004
- [7] H. S. Park, G. Thursby and B. Culshaw, "Optical acoustic detector based on a fiber Fabry-Perot interferometer", *Appl. Opt.*, vol. 44, no. 4, pp. 489-492, 2005
- [8] J. M. Vaughan, *The Fabry-Perot interferometer: History, Theory, Practice and Applications*, Taylor & Francis, 1989
- [9] F. T. S. Yu and S. Yin, *Fiber Optic Sensors*, CRC Press, 2002
- [10] T. Wang, S. Zheng and Z. Yang, "A high precision displacement sensor using a low-finesse fibre optic Fabry-Pérot interferometer", *Sensors Actuators A*, no. 69, pp. 134-138, 1998
- [11] B. C. Chen, J. Luo and D. Li, "Code counting of optical fringes: methodology and realization," *Appl. Opt.*, vol. 44, no. 2, pp. 217-223, 2005
- [12] T. K. Gangopadhyay, "Non-contact vibration measurement based on extrinsic Fabry-Perot interferometer implemented using arrays of single-mode fibres", *Meas. Sci. Technol.*, vol. 15, no. 5, pp. 911-917, 2004
- [13] A. Dandridge, A. B. Tveten, and T. G. Giallorenzi, "Homodyne demodulation scheme for fiber optic sensors using phase generated carrier", *IEEE Trans. on Microwave theory and techniques*, vol. MTT-30, no. 10, pp. 1635-1641, 1982
- [14] F. Docchiot, U. Perinis and H. Tizianis, "A combined distance and surface profile measurement system for industrial applications: a European project", *Meas. Sci. Technol.*, vol. 5, pp. 807-815, 1994
- [15] H. C. Seat, S. Pullteap and T. Bosch, "An extrinsic fibre optic interferometer with possible signal fading compensation for vibrometric applications", *Proc. IEEE IMTC XXII*, pp. 2236-2241, Canada, 2005
- [16] L. Mertz, "Real time fringe pattern analysis", *Appl. Opt.*, vol. 22, no. 10, pp. 1535-1539, 1983
- [17] T. Haritomo, "Real-time", "Phase calculation based on curve fitting with a two-wavelength interferometer" *Opt. Express*, vol. 11, no. 8, pp. 895-898, 2003
- [18] M. A. Gdeisat, D. R. Burton and M. J. Lalor, "Real time hybrid fringe pattern analysis using a linear digital phase locked loop for demodulation and unwrapping", *Meas. Sci. Technol.* vol. 11, pp. 1480-1492, 2000
- [19] M. Servin, D. Malacara, and F. J. Cuevas, "Direct phase detection of modulated Ronchi rulings using a phase locked loop", *Opt. Eng.*, vol. 33, no. 4, pp. 1193-1199, 1994
- [20] C. E. Padillia, V. L. Karlov, L. Matson and H. M. Chun, "Advanced fringe tracking algorithms for low-light level ground-based stellar interferometry" *Proc. of American Control Conf.*, pp. 1585-1589, USA, 1998
- [21] M. Servin, F. J. Cuevas, D. Malacara, J. L. Marroquin, and R. R. Vera, "Phase unwrapping through demodulation by use of the regularized phase-tracking technique", *Appl. Opt.*, vol. 38, no. 10, pp. 1934-1941, 1999
- [22] T. K. Gangopadhyay and P. J. Henderson, "Vibration : history and measurement with an extrinsic Fabry-Perot interferometer sensor with solid-state laser interferometry", *Appl. Opt.*, vol. 38, no. 12, pp. 2471-2477, 1999
- [23] H. C. Seat, "A pseudo dual-cavity extrinsic fibre Fabry-Pérot interferometric vibrometer", *Sensors Actuators A*, vol. 110, pp. 52-60, 2004
- [24] A. J. Rainal, "Another zero-crossing principle for detecting narrowband signals", *IEEE Trans. Instrum. Meas.*, vol. 16, pp. 135-138, 1967
- [25] R. J. Niederjohn, "A Mathematical formulation and comparison of zero-crossing analysis techniques which have been applied to automatic speech recognition", *IEEE Trans. Acoustics, Speech and Signal Processing*, vol. 23, no. 4, pp. 373-380, 1975
- [26] S. Z. Hsue and S. S. Soliman, "Automatic modulation classification using zero-crossing", *IEE Proc.*, vol. 137, no. 6, pp. 459-464, 1990
- [27] S. Pullteap, H. C. Seat and T. Bosch, "Modified fringe-counting technique applied to a dual-cavity fiber Fabry-Perot vibrometer," *Opt. Eng.*, vol. 42, no. 11 pp. 15563/1- 8, 2007
- [28] A. Choudry, "Digital holographic interferometry of convective heat transport", *Appl. Opt.*, vol. 20, no. 7, pp. 1240-1244, 1981
- [29] A. Kasukawa, N. Matsumoto, I. J. Murgatroyd, T. Fukushima, S. Kashiwa and H. Okamoto "Temperature dependence of emission wavelength in 1.3 μm GaInAsP/InP GRIN SCH MQW laser diodes grown by MOCVD", *Semicond. Sci. Technol.*, vol. 5, pp. 498-501, 1990

- [30] S. Pullteap, H. C. Seat and T. Bosch, "Temperature and distance-dependent errors in a dual-cavity fiber Fabry-Perot interferometer for vibration analysis", *Proc. of IEEE IMTC XXIV*, pp. 1-6, Poland, 2007
- [31] W. Khunsin, A. Amann, G. Kocher-Oberlehner, S. G. Romanov, S. Pullteap, H. C. Seat, E. P. O'Reilly, R. Zentel and C. M. Sotomayor Torres, Noise-assisted crystallization of opal films, *Adv. Funct. Mater.*, vol. 22, pp. 1812-1821, 2012
- [32] H. C. Seat, P. Chawah, M. Cattoen, A. Sourice, G. Plantier, F. Boudin, J. Chéry, C. Brunet, P. Bernard and M. Suleiman, Dual-modulation fiber Fabry-Perot interferometer with double reflection for slowly-varying displacements, *Opt. Lett.*, vol. 37, no. 14, pp. 2886-2888, 2012
- [33] C. K. Kirkendall and A. Dandridge, Overview of high-performance fiber-optic sensing, *J. Phys. D: Appl. Phys.*, vol. 37, pp. R197-R216, 2004
- [34] O. Sasaki and K. Takahashi, Double sinusoidal phase-modulating laser diode interferometer for distance measurement, *Appl. Opt.*, vol. 30, no. 25, pp. 3617-3621, 1991
- [35] A. A. Kulkarni, S. Battacharya and A. Prabhakar, All-fiber interferometry: design and analysis, *Appl. Opt.*, vol. 50, no. 22, pp. 4450-4456, 2011
- [36] R. C. Addy, A. W. Palmer and K. T. V. Grattan, Effects of external reflector alignment on sensing applications of optical feedback in laser diodes, *J. Lightwave Technol.*, vol. 14, no. 12, pp. 2672-2676, 1996
- [37] H. Shalom, A. Zadok, M. Tur, W. D. Cornwell and I. Andonovic, On the various time constants of wavelength changes of a DFB laser under direct modulation, *IEEE J. Quant. Electron.*, vol. 34, no. 10, pp. 1816-1822, 1998
- [38] M. A. Zumberge, J. Berger, M. A. Dzieciuch and R. L. Parker, Resolving quadrature fringes in real time, *Appl. Opt.*, vol. 43, no. 4, pp. 771-775, 2004
- [39] S. Pullteap, H.C. Seat, M. Cattoen, P. Bernard, J.-C. Lépine, F. Boudin, J. Chéry & T. Bosch, *A phase-tracking fiber interferometer for seismologic applications*, IEEE Sensors 2008 Conference, Proc. of the 7th IEEE Conference on Sensors, Lecce (Italie), pp.938-941, 26-29 Oct 2008
- [40] M. Suleiman, H. C. Seat, M. Cattoen, *Capteur interférométrique fibré multiaxes à modulation*, 10th CMOI 2010, Toulouse-Labège (France), 15-19 Nov 2010

Chapter 3 - Self-mixing interrogation technique for fiber Bragg grating strain sensors

3.1 Introduction

This chapter is a résumé of the PhD research on developing a novel interrogating technique based on the self-mixing effect or optical feedback interferometry for fiber Bragg gratings under dynamic strain loading (Dr M. Suleiman, 2005–2008 [1]).

The ubiquitous fiber Bragg grating (FBG) was initially conceived for optical fiber telecommunications since its discovery by Hill *et al.* back in the late 1970s [2]. The Bragg grating structure is formed in the Ge-sensitized core of an optical fiber by UV inscription of a periodically modulated refractive index. Designed initially as a narrowband in-fiber optical reflector, a Bragg grating reflects a forward propagating lightwave into a counter-propagating mode with a centre wavelength exhibiting an extremely narrow spectral width, corresponding to the resonant Bragg condition, given by $\lambda_B = 2n_{eff}\Lambda$ (where n_{eff} is the effective index of the grating structure in the core region and Λ represents the grating pitch). The rest of the non-resonant propagating wavelengths/modes are transmitted along the fiber after the grating structure. FBGs can therefore serve as highly effective fiber-based optical filters whose bandwidth can be tuned to specific requirements during the manufacturing process. Although uniform gratings are the mane of the FBGs thus produced, tilted (or blazed), chirped and long-period gratings are also commercially available.

FBGs have, however, evolved from a uniquely telecommunications component to find wide-ranging applications in metrology and have now become synonymous with structural health monitoring (SHM). FBGs, with their many advantages such as their multiplexing capability, compact size which allows for embedding in advanced structures and materials, high precision and sensitivity, wavelength-encoded operation and their quasi-linear spectral response to external influences, are thus suitable in field applications for monitoring infrastructures in civil engineering, transportation and, in the gas and oil industry where preventive maintenance often leads to extended service lifespan while reducing the dire consequences of failure [3-5]. That FBGs are particularly suited to sensing applications is due to its inherent nature as a purely wavelength-dependent device, hence any fluctuations and/or drifts in the optical system do not, in any significant manner, affect their interrogation since, under most circumstances, only their unique wavelength-encoded response is monitored. Any applied perturbations, physical and mechanical, which results in changes to the Bragg condition via n_{eff} and Λ (due to the thermal-optic and/or photoelastic coefficients of the fiber material respectively) will therefore induce a shift in λ_B . Hence, sensors employing FBGs to measure physical quantities such as strains, bends, deformation, pressure and temperature can be envisaged since these devices are particularly sensitive along the axial or longitudinal axis. Most FBG interrogation techniques thus involve tracking this measurand-induced shift of λ_B . Although optical spectrum analyzers and monochromators with sufficient spectral resolution are obvious candidates for this purpose, they remain laboratory-based instruments, being fragile, cumbersome and costly to use in field applications besides having measurement rates that are somewhat limited. The recent FBG Interrogator (Micron Optics) is a suitable solution offering multi-channel interrogation capability but compromise must be found with respect to the size of the infrastructures to be instrumented in terms of cost-effectiveness. Various methods of interrogating FBGs have also been devised over the past two decades [4,5-10]. Most of these require some optical filtering using edge filters and its variants as well as interferometric wavelength detection although their robustness and sensitivity to external environmental factors have to be taken into consideration. Therefore, an

alternative technique offering simple, accurate and cost-effective interrogation of FBG-based sensors with sufficient robustness to be deployed in the field is highly attractive.

This work concerns a novel interrogation technique which exploits the self-mixing effect to detect dynamic strain variations in an FBG [11,121]. The sensing fiber is simply coupled to a fiber pigtailed DFB-type laser diode (DFB-LD) package incorporating an internal photodiode, leading to a greatly simplified configuration since the DFB-LD functions as both source and detector. The sawtooth-like interference signals typical of cavity optical feedback [13], which are obtained due to the optical retro-reflection off the grating structure, allow the Bragg grating reflectivity to be determined, from which both the Bragg wavelength shift and, more significantly, the embedded strain information, due to the applied mechanical loading, can be simultaneously extracted. This scheme thus enables a compact FBG sensor to be constructed to provide quasi-interferometric resolution inherent of self-mixing interferometry.

3.2 Operating principles

The dependence of the FBG reflectivity on induced strains resides on the sensitivity of n_{eff} and Λ to external disturbances. From coupled-mode theory [14,15], when the forward propagating mode reflected off the Bragg grating structure couples into the backward mode, resonance is obtained, leading to a reflected wavelength, λ_B . Thus, when this arises, a fraction of the incident optical power (P_I) is reflected by the grating (P_R) in accordance with the design reflectivity, R_{FBG} , as

$$R_{FBG} = \frac{P_R}{P_I} = \frac{\sinh^2\left(\sqrt{K^2 - \sigma^2} \cdot L_{FBG}\right)}{\cosh^2\left(\sqrt{K^2 - \sigma^2} \cdot L_{FBG}\right) - \frac{\sigma^2}{L_{FBG}^2}} \quad (3.1)$$

where L_{FBG} is the grating length, which when subjected to external strain perturbation, for example, becomes $L_{FBG}(\varepsilon_z)$ and $K = (\pi/\lambda)\Delta n_{eff}(z)$ is the coupling coefficient between modes in the grating having an index modulation amplitude along the optical axis, $\Delta n_{eff}(z)$. σ represents the detuning wave vector and is given by

$$\sigma = 2\pi n_{eff} \left(\frac{1}{\lambda} - \frac{1}{\lambda_B} \right) \quad (3.2)$$

A typical reflected spectrum from an FBG under no loading is shown in Fig. 3.1 for $R_{FBG} \sim 0.5$ at $\lambda_B \sim 1309.5$ nm.

The FBG is highly-sensitive to both longitudinal loading as well as to temperature variations. Under strain loading, Λ and n_{eff} will be caused to vary due to the elasticity and the photoelastic effects of the fiber material, respectively. And in the presence of temperature variation, the grating pitch Λ and the effective core refractive index n_{eff} will be modified accordingly due to the inherent thermal expansion and the thermal-optical effects of the fiber material. The combined influences will shift λ_B as [16,17]

$$\Delta\lambda_B = 2 \left(\Lambda \frac{\partial n_{eff}}{\partial L_{FBG}} + n_{eff} \frac{\partial \Lambda}{\partial L_{FBG}} \right) \Delta L_{FBG} + 2 \left(\Lambda \frac{\partial n_{eff}}{\partial T} + n_{eff} \frac{\partial \Lambda}{\partial T} \right) \Delta T \quad (3.3)$$

where the first term between brackets on the right represents the strain influence and the second term the subsequent temperature effects on the FBG. Only strain effects are studied in this work since temperature effects are considered to be too rapid to be of any significant influence. Hence, for an applied longitudinal strain, ε_z , at a nominally constant temperature, $\Delta\lambda_B = 2(\Lambda \partial n_{eff} / \partial L_{FBG} + n_{eff} \partial \Lambda / \partial L_{FBG}) \Delta L_{FBG}$ [18], with

$$\frac{\Delta\lambda_B}{\lambda_B} = \left(1 - \frac{n_{eff}^2}{2} [\rho_{12} - \nu(\rho_{11} + \rho_{12})] \right) \varepsilon_z = (1 - P_e) \varepsilon_z \quad (3.4)$$

where $P_e = n_{eff}^2/2[\rho_{12} - \nu(\rho_{11} + \rho_{12})]$ is the strain-optic constant, ρ_{11} and ρ_{12} Pockel's strain-optic tensor coefficients of the fiber, and ν Poisson's ratio of the fiber material. Further, in the presence of axial strain ε_z , the grating pitch length then becomes [19]

$$\Lambda(\varepsilon_z) = \Lambda_0(1 + \varepsilon_z) \quad (3.5)$$

with Λ_0 the strain-free pitch. n_{eff} also undergoes changes and takes the form

$$n_{eff}(\varepsilon_z) = n_{eff} + \partial n_{eff} = n_{eff} + \left(-\frac{n_{eff}^2}{2} [\rho_{12} - \nu(\rho_{11} + \rho_{12})] \varepsilon_z \right) \quad (3.6)$$

Then, (3.2) has to be modified into

$$\sigma = \frac{2\pi(n_{eff} + \partial n_{eff})}{\lambda} - \frac{\pi}{\Lambda_0(1 + \varepsilon_z)} \quad (3.7)$$

to take into account the external loading before re-injection into (3.1) for analysis. For 3 different values of ε_z , R_{FBG} can then be observed to shift towards the longer wavelengths with increasing axial strains while the peak reflectivity remains relatively constant, as shown in Fig. 3.2.

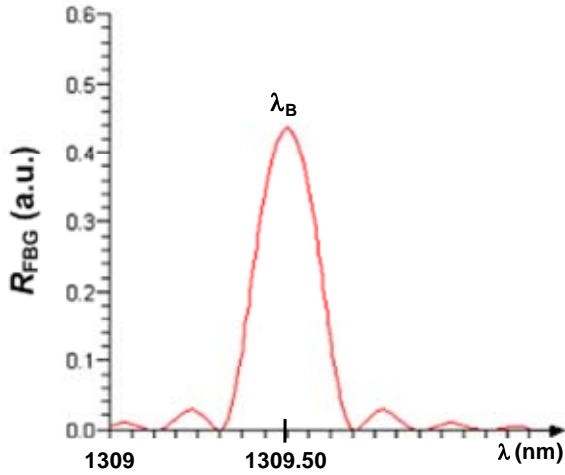


Fig. 3.1. R_{FBG} spectrum centered at $\lambda_B = 1309.50$ nm

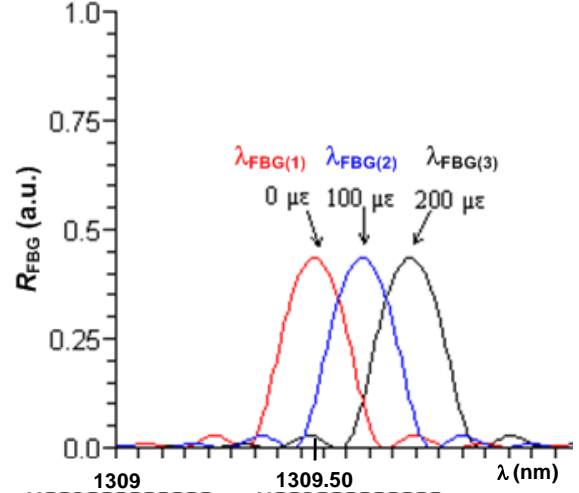


Fig. 3.2. Simulated shifts of λ_B towards longer wavelength via R_{FBG} with 3 different axial strains

The reflectivity spectra have been obtained analytically using the following parameters: $L_{FBG} = 6$ mm, $n_{eff} = 1.441$, $\rho_{12} = 0.27$, $\rho_{11} = 0.121$, $\nu = 0.17$, $\lambda_B = 1309.4$ nm, $\Delta n_{eff}(z) = 0.0001$. The simulation results ($\Delta\lambda_B \sim 1$ pm/ $\mu\varepsilon$) are in relatively good agreement with the values from published literature (1.04 pm/ $\mu\varepsilon$).

Hence, external strains imparted to the grating structure will modulate (3.7) leading to the grating reflectivity, R_{FBG} , which is intrinsically associated with a central wavelength, λ_B , being shifted. The displacement of R_{FBG} is thus a function of the strength of the induced strain and is exploited in the self-mixing (SM) technique as the optical feedback parameter subject to dynamic strain loading [20].

Optical feedback occurs when a fraction of the emitted beam is back-reflected into the laser cavity by an object along the beam path. This coherent back-reflection, which presents an optical phase or the variation thereof depending on the object distance and its reflectivity, mixes with the existing electric fields in the laser cavity. For a mobile object, this SM effect then modulates the subsequent laser output characteristics to result in a series of sawtooth-type fringes whose profile is a function of the characteristic parameter known as the feedback strength, C . Although

detrimental in optical telecommunications, this optical feedback has subsequently been employed for many sensing applications [21]. The FBG can therefore be used as an external resonant cavity to the SM laser as illustrated in Fig. 3.3.

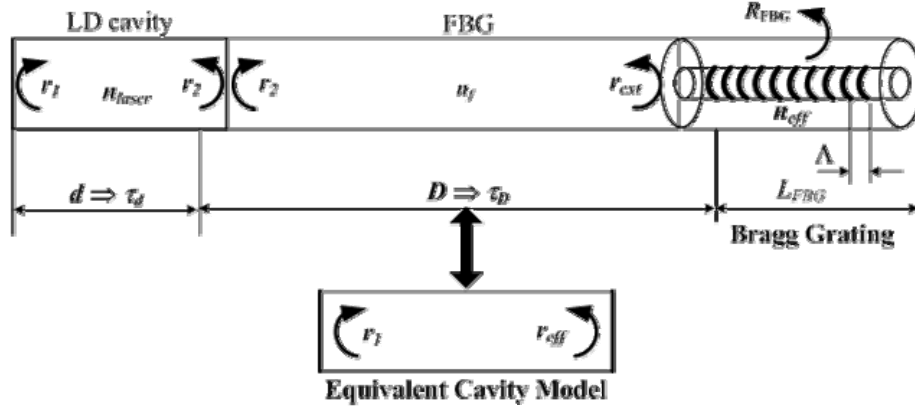


Fig. 3.3. FBG coupled to SM laser for strain sensing and its equivalent cavity

The external cavity represented by the FBG couples the incident laser power back into the laser cavity via a reflectivity, r_{ext} , which takes into consideration both R_{FBG} and the roundtrip feedback efficiency, η , between the DFB-LD and the FBG, to result in

$$r_{ext} = \eta \sqrt{R_{FBG}} \quad (3.8)$$

Equation (3.8) assumes identical polarization for the emitted and reflected light. The external cavity in conjunction with the DFB-LD facets can then be assimilated to an equivalent cavity with an effective reflection coefficient of $r_{eff} = r_2 [1 + \xi \exp(-j2\pi\nu\tau_D)]$ where $\xi = (1 - r_2^2) \cdot r_{ext} / r_2$ defines the coupling between the DFB-LD and the external FBG target. More importantly for SM interferometry, the grating-reflected optical feedback which is re-injected into the DFB-LD cavity results in a feedback parameter which is defined as

$$C = \xi \sqrt{1 + \alpha^2} \frac{\tau_D}{\tau_d} \quad (3.9)$$

where α is the linewidth enhancement factor, τ_D the roundtrip time delay from the grating and τ_d the roundtrip time in the laser cavity. Thus under optical feedback, the optical phase change in the subsequent DFB-LD emission frequency, ν , is then written in the form [22,23]

$$\Delta\phi(\nu) = 2\pi(\nu - \nu_0)\tau_d + \xi \sqrt{1 + \alpha^2} \cdot \sin[2\pi\nu\tau_D + \arctan(\alpha)] \quad (3.10)$$

with ν_0 its emission frequency without feedback. The optical phase under feedback, $\phi_F(t)$, and the free-running phase, ϕ_0 , can be re-arranged to yield

$$\phi_0(t) = \phi_F(t) + C \sin[\phi_F(t) + \arctan(\alpha)] \quad (3.11)$$

The influence of the C parameter thus manifests itself in the optical phase emitted by the DFB-LD under optical feedback (or retro-injection) and is an important consideration in applications involving SM as it conditions the SM fringes that can be obtained [24,25]. This is duly demonstrated in Fig. 3.4 for different values of C under identical target movement.

For small C , the SM fringes are almost sinusoidal (Fig. 3.4(a)) but there is evidence of a sharp gradient. Now, when C increases from 0.9 to 1.5, the sawtooth profile characteristic of SM interference is obtained. From $C = 2.5$ –6.7, an increasing hysteresis is observed in which the fringes become asymmetric dissimilar fringe amplitudes. For very high C (i.e. from 4.6 onwards), pronounced hysteresis is observed together with subsequent fringe loss on the right half-period, as illustrated in Fig. 3.4(e) and 3.4(f) where the lost of an additional fringe on both half-periods is observed for $C = 6.7$. Note that the inclination of the sawtooth gradient indicates

the direction of the movement while the point of inflection determines the object's directional change. Nevertheless, the principal objective of this work being the proof-of-concept of exploiting SM interrogation of FBGs under strain loading, the targeted application is restrained to only the weak and/or moderate feedback regime ($0.1 < C < 2$).

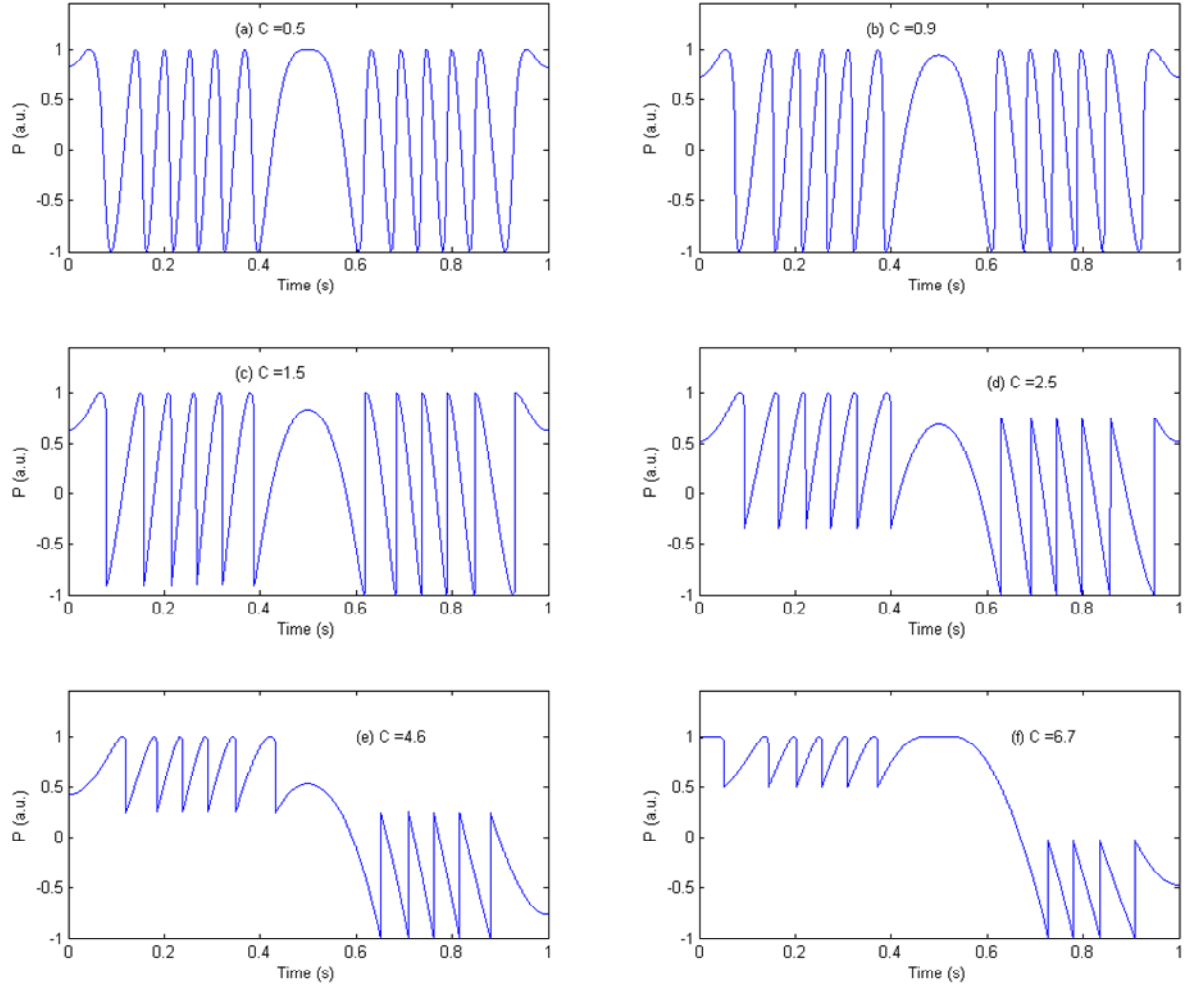


Fig. 3.4. Evolution of SM fringes as a function of C values

Hence, the detected optical power resulting from SM interference within the DFB-LD cavity can be written as [26]

$$P = P_0(1 + V \cos \phi_F) \quad (3.12)$$

with V a visibility function that may be defined in the usual form as $V = (P_{\max} - P_{\min}) / (P_{\max} + P_{\min})$.

3.3 Experimental validation and sensor characteristics under dynamic strain loading

The experimental validation of the SM interrogation technique consists of directly mounting the FBG for strain sensing in a cantilever beam configuration, as shown in Figs. 3.5. The DFB-LD without optical isolation functions as both source and detector thus greatly simplifying the experimental set-up. The emitted light is transmitted to the FBG ($\lambda_B = 1309.43$ nm) with a measured R_{FBG} of $\sim 17\%$ via a 1x2 fiber coupler. The signal processing algorithm reported in [12] is used to describe the behavioural model of this technique and to numerically estimate the value of C (~ 0.95). Hence, we can safely assume to be working within the weak feedback regime. The resonant reflection off the Bragg grating structure is retro-injected into the DBF-LD cavity on its return trip where it perturbs the existing fields. As a precaution, the reflected FBG spectrum is monitored by an *ANRITSU MS9710A* optical spectrum analyzer (OSA) via the second port of the coupler. An integrated photodiode in the DFB-LD package then

detects these back-reflected optical signals which are subsequently amplified by an external electronic circuit before being transferred to a digital oscilloscope for display and recording.

The FBG is glued onto a test plate by epoxy adhesive and secured onto a solid metal structure to form a cantilever beam set-up. The *PASCO Scientific* wave vibrator, fixed onto the free cantilever end just below the Bragg grating, is used to provide dynamic loading and is driven by a function generator at 88 Hz for excitation amplitudes ranging from 180 mV to 926 mV. For comparison of strain measurements obtained with the SM–FBG sensor, the *Philtec D63* displacement sensor (sensitivity -2.786 mV/ μ m) is employed to measure the deflection applied by the vibrator. The induced strain are then extracted using the strain-bending relationship for a cantilever beam

$$\varepsilon_z = \frac{3(l-b)(h+d_f)}{a^2(3l-a)} \delta_{\max} \quad (3.13)$$

with ε_z the axial strain applied at the point $b=20$ mm measured on either side from the center of the FBG, $h=2.5$ mm the thickness of the beam under test and d_f (~ 0.13 μ m) the fiber diameter. The distance from a reference fixed support to the loading point is denoted as a ($=135$ mm) and $l=300$ mm is the distance between the fixed support and the free end while δ_{\max} is the cantilever deflection incurred.

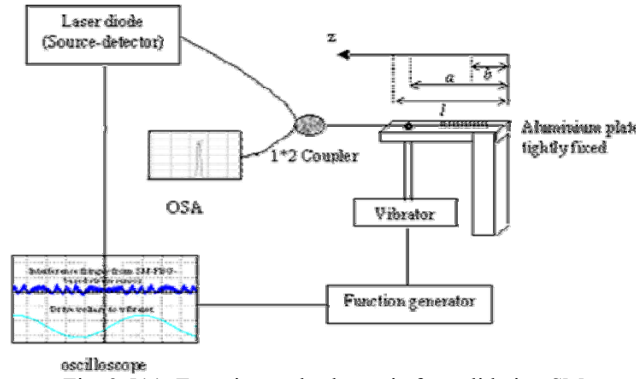


Fig. 3.5(a). Experimental schematic for validating SM interrogation technique

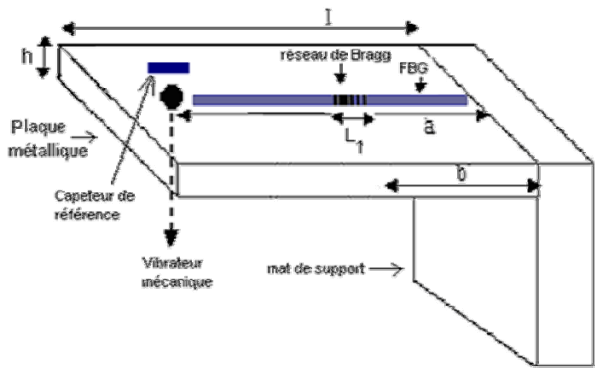


Fig. 3.5(b). Positioning of *Philtec D63*-model reference sensor on cantilever beam

The tension-compression nature of the dynamic strain effects leads to the modification of the FBG characteristics (via $\Lambda(\varepsilon_z)$ and n_{eff}). These are translated into modifications of the resulting DFB-LD emission characteristics, leading to a series of sawtooth-type optical SM interference signals in which the desired strain information are directly embedded. Although the wavelength shift induced by the applied strains can classically be determined by using (3.4), the induced strains measured by the FBG sensor are calculated using simple fringe counting where one complete fringe is equivalent to a variation in the optical path length of $\lambda_B/2$. The resulting relationship between the elongation of the FBG, ΔL_G , and the number of sawtooth fringes, N , can thus simply be written as $\Delta L_G = N \cdot \lambda_B / 2n_{eff}$. The desired strain information, by definition, can then be extracted via

$$\varepsilon_z = \frac{\Delta L_G}{L_G} = N \frac{\lambda_B}{2n_{eff}L_G} \quad (3.14)$$

where $\lambda_B = 1309.43$ nm, $L_G = 25$ mm is the total fiber length of the FBG sensor under strain loading (i.e. the gauge length).

Two typical SM signals (channel 1) are illustrated in Figs. 3.6 for two values of mechanical deflections applied (in the form of excitation amplitudes). Channel 3 is the drive voltage to the mechanical vibrator while Channel 2 shows the detected voltage signals from the reference sensor positioned at the free end of the cantilever beam, whose peak-to-peak amplitude

can be converted into deflection for this point. The sawtooth fringes in Fig. 3.6(a) are induced by an excitation amplitude of 840 mv. In spite of the relatively important noise level, ~ 7.5 fringes can be observed distinctly and corresponds to a demodulated strain value of $135 \mu\epsilon$. In Fig. 3.6(b), the demodulated strain from the detected 8.5 fringes corresponds to $\sim 153 \mu\epsilon$ at 926 mV of excitation amplitude. The low amplitude of these signals and the absence of hysteresis, in particular, further validate the weak feedback regime under which this work has been performed. The peak-to-peak deflections measured by the reference sensor, estimated at ~ 301 and $332 \mu\text{m}$ respectively, resulted in corresponding induced strains of $126 \mu\epsilon$ and $138 \mu\epsilon$. The results thus confirm the feasibility of our interrogation scheme for FBG-based strain sensors.

Fig. 3.6(a). SM signal from FBG strain sensor with ~ 7.5 sawtooth fringes

The strain response of the SM-interrogated FBG (SM-FBG) sensor over a deflection range of 65–332 μm is plotted in parallel to that of the reference sensor in Fig. 3.7, thus corroborating the SM-FBG measurements.

Fig. 3.7. Strain response from SM-FBG sensor over 65 – 332 μm deflection range

3.4 SM-FBG Sensor limits and improvements to sensor performance

(~ 0.14 nm) which corresponds to a measurable strain of $160 \mu\epsilon$. This can, in part, be resolved by using FBGs with larger spectra and/or a more costly tunable laser diode. During the measurements, the effects of laser power fluctuations which could ultimately introduce errors in the obtained results are also taken into consideration. This fluctuation is important when the power varies rapidly. Over an 8-hour period, the laser power does not vary significantly (equivalent wavelength variation of ~ 4 pm from the set point). Hence, this slowly-varying parameter is considered negligible in the outcome of the results over the relatively short duration of the experiments.

As mentioned in Section 3.3, the reference sensor detects a deflection of the cantilever beam which intrinsically introduces an angle from the perpendicular. As such, the deflection measured is not in the normal incidence configuration in which the sensor has to perform. This can explain the slight deformation of the reference voltage from the sinusoidal form which subsequently induces relatively large errors between the 2 devices. Further, there is a limit to the dynamic strain range which can be measured by the current SM-FBG sensor, as discussed above. Also, since the gauge length cannot be infinitely increased, a means has to be found to extend the dynamic range of our sensor. The previous experiment requires fine adjustment of the passively-operated or fixed DFB-LD wavelength (λ_{LD}) to closely match the FBG peak wavelength. The wavelength requirement at the initial stages thus pertains only to an FBG sensor with a dynamic range symmetric about the FBG central wavelength and this consequently limits the dynamic range when the latter shifts beyond the fixed DFB-LD spectrum. To extend this dynamic range, a simple modulation scheme to drive the interrogating λ_{LD} across both extreme ends of the displacing FBG wavelength under loading is introduced here, thus allowing the dynamic range to be improved by a factor of at least half the FBG spectrum width. In order to have a better appreciation of the SM-FBG sensor, a further experiment is carried out with a set of 4 strain gauges as reference, as illustrated in Figs. 3.8.

The same DFB-LD is temperature-regulated at room temperature. Temperature regulation is also used to provide a coarse adjustment of λ_{LD} to correspond to the resonant λ_B (~ 1309.91 nm) of the FBG employed while the source current is driven by a precision LD current driver. In addition, a precision function generator is employed to modulate the injection current to the DFB-LD to enable scanning λ_{LD} across the FBG spectrum and, hence, increase the dynamic range capacity of the sensor.

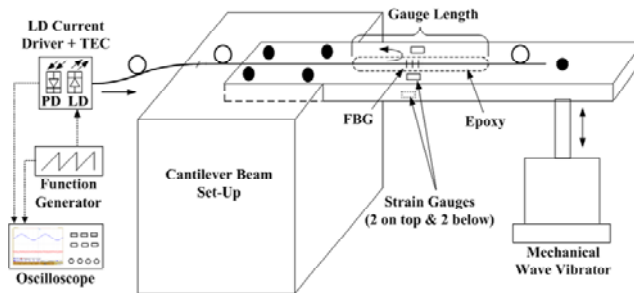


Fig. 3.8(a). Experimental schematic for strain sensing with current modulation

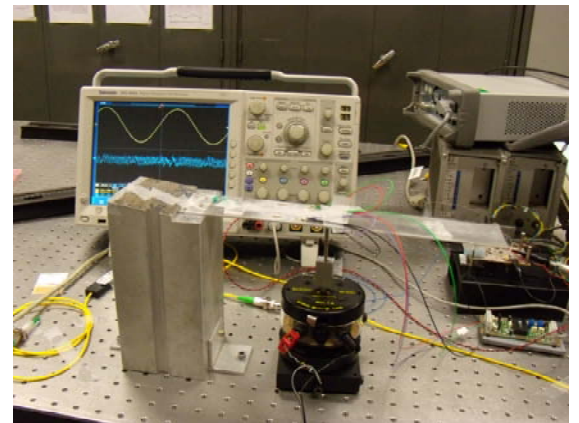


Fig. 3.8(b). Image of experimental set-up for modulation-based SM-FBG sensor

The DFB-LD emission is injected directly via the fiber pigtail into the FBG which has been attached with epoxy-based adhesives onto the cantilever beam over a length of ~ 87 mm, as shown in Fig. 3.9. This length is defined as the gauge length, L_G , of the FBG strain sensor since the fiber material is considered homogeneous. Note that the grating length is $L_{FBG} \sim 8$ mm and has been inscribed at approximately 30 cm from the input end of the fiber. The same mechanical wave generator is used to apply the necessary strain to the FBG by deflecting the cantilever

beam. For comparison purposes, four strain gauges are employed and mounted in a full-Wheatstone bridge configuration at approximately the same position as the FBG, with two gauges glued to the top section of the beam and two others onto its bottom section.

λ_{LD} is initially adjusted to approximately match the center of λ_B which has a FWHM spectrum width of $\delta\lambda_{FBG} \approx 0.14$ nm so that optical feedback can be obtained upon the application of strain to the grating structure. Measurements are first carried out with a fixed DFB-LD current. Excitation to the mechanical vibrator is then increased at a constant frequency of to ~ 18 Hz. The SM fringes are recorded using a 500 MHz digital oscilloscope translating into ~ 15 – 130 $\mu\epsilon$, as given by the reference strain gauge measurement, beyond which no further fringes can be observed.

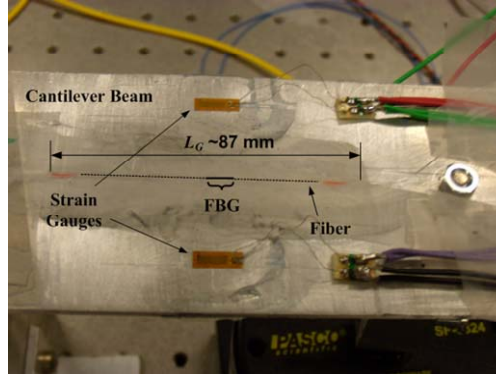


Fig. 3.9. Close-up view of SM-FBG strain sensor with $L_G \sim 87$ mm

Before proceeding to extract strain information from the SM fringes, a smoothing procedure is applied to the detected raw data from the PD to reduce electronic noise which can consequently prevent clear identification of the fringe peaks. The induced strains measured by the SM-FBG sensor are then calculated using (3.14) and plotted against the reference strain gauge values in Figs. 3.10 over a range of ~ 15 – 122 $\mu\epsilon$ together with the associated error. Very good concordance from the 2 devices is achieved. This is clearly demonstrated by the slope of the SM-FBG sensor versus reference sensor plot, with a gradient (or ratio) of ~ 1.019 instead of the ideal ratio of 1. In addition, a maximum error of $\sim 3.55\%$ is committed at ~ 104 $\mu\epsilon$ over the entire strain range studied while the minimum error is $\sim 0.09\%$ at 122 $\mu\epsilon$.

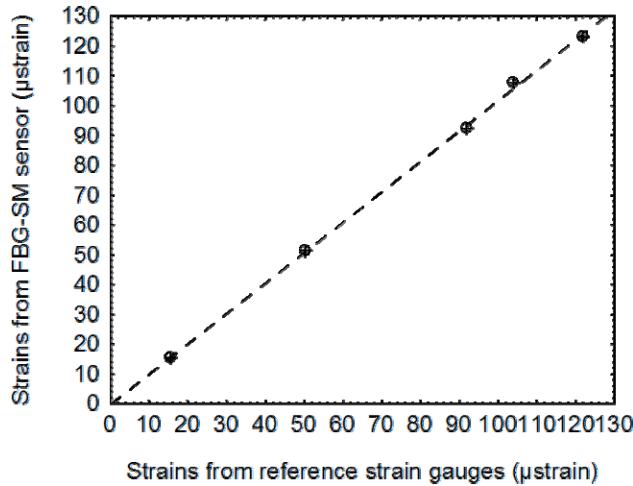


Fig. 3.10(a). Measured strains from SM-FBG sensor and strain gauges over 15 – 122 $\mu\epsilon$ range

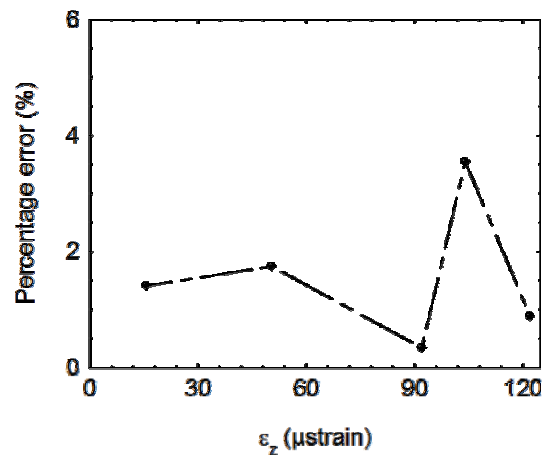


Fig. 3.10(b). Relative error plot in %

There is however an intrinsic limit to the above sensor system where induced strains > 130 $\mu\epsilon$ can no longer be measured since no SM fringes are detected. In the current sensor configuration, λ_{LD} is kept constant during the measurement whereas R_{FBG} (spectral width $\delta\lambda_{FBG} \sim 0.14$ nm) is continuously displaced about λ_B under dynamic strain loading. In the optimal case

where both extremities of R_{FBG} displace across the fixed λ_{LD} , then its 0.14 nm spectral width will correspond to a measurable physical strain of $\sim 134.6 \mu\epsilon$ for the SM-FBG sensor. Beyond this range, no reflection, and hence no optical feedback is re-injected into the DFB-LD cavity, hence the absence of SM fringes in the above experiment. In order to increase the dynamic range of the SM-FBG strain sensor, λ_{LD} has to be continuously matched to the displacing R_{FBG} to ensure that optical feedback is constantly retro-injected into the cavity.

The modulation scheme subsequently implemented in this work to increase the measurement range of the SM-FBG sensor involves scanning the DFB-LD injection current above threshold ($I_{LD0} \sim 7$ mA) as illustrated in Figs. 3.11.

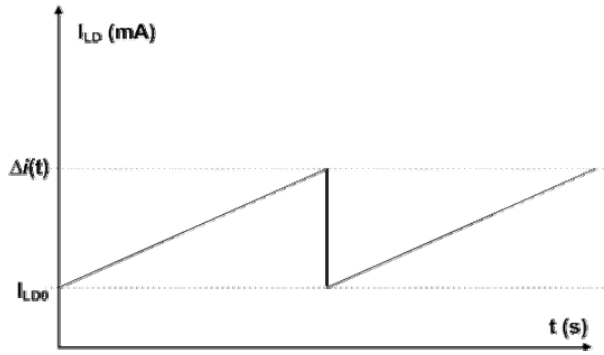


Fig. 3.11(a). Ramp profile current modulation on SM-FBG sensor

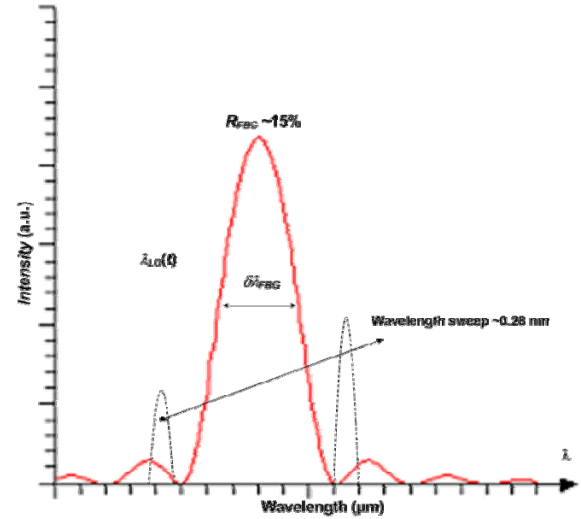


Fig. 3.11(b). Equivalent wavelength modulation

The limit in the scanning range is constrained by the maximum tolerable injection current to which the DFB-LD can be subjected (~ 60 mA). The laser employed has a linear wavelength-current relationship of ~ 6 pm/mA over the operating current range above threshold. A very low scanning frequency of 10 mHz is used so that the approximation of the variation in λ_{LD} remains linear and can be justified by considering the equivalent optical phase for a slow modulation coefficient, $\delta(t)$, which takes the form

$$\Delta\phi \approx \frac{4\pi n_{eff}}{\lambda_{LD}} [L_{FBG} + \partial L_G(t)] [1 - \delta(t)] \approx \frac{4\pi n_{eff}}{\lambda_{LD}} [L_{FBG} + \Delta L_G(t)] \quad (3.15)$$

with $\Delta L_G(t) \approx \partial L_G(t) + \delta(t) \cdot L_{FBG}$ which takes into account the modulation coefficient. Here, $\partial L_G(t)$ represents the temporal fiber elongation, equivalent to the definition in (3.14). For slow modulation frequencies and hence small $\delta(t)$, the elongation due to induced strains can then be approximated as $\Delta L_G(t) \approx \partial L_G(t)$. Under dynamic strain loading, λ_{LD} is thus considered to be scanned linearly to cover both extremities of the moving R_{FBG} .

The feasibility of this modulation scheme is experimentally proven here. λ_{LD} is initially positioned at one extremity of R_{FBG} and, using a ramp excitation, swept across 0.28 nm while the vibrator amplitude is simultaneously increased beyond the previous strain limit of $130 \mu\epsilon$ defined by $\delta\lambda_{FBG}$ (~ 0.14 nm) to $\sim 190 \mu\epsilon$. The experimental signals obtained from the SM-FBG sensor for $190 \mu\epsilon$ are illustrated in Fig. 3.12.

The reference strain gauges output a dynamic strain of $\epsilon_z = 190 \mu\epsilon$ while the SM-FBG sensor measures an axial strain of $\sim 200 \mu\epsilon$, a value which is 1.5 times the previous strain that can be technically measured using a fixed DFB-LD current scheme. This corresponds to approximately 39 fringes with an error measurement of $\sim 5.26\%$. The low-frequency current modulation scheme applied to the interrogating DFB-LD can thus enable the dynamic range to

be equivalently extended from $\delta\lambda_{FBG}$ to $\delta\lambda_{FBG} + \frac{1}{2}\delta\lambda_{FBG}$. One limiting point is that the sensor resolution attainable via simple fringe-counting is only $\sim 6 \mu\epsilon$ (corresponding to 1 fringe). Further, the maximum error of the present sensor system is of identical order due to potential fringe identification difficulties. The sensor performance in terms of resolution and precision can, however, be further improved by using a more advanced phase demodulation technique for SM interferometry [29,30].

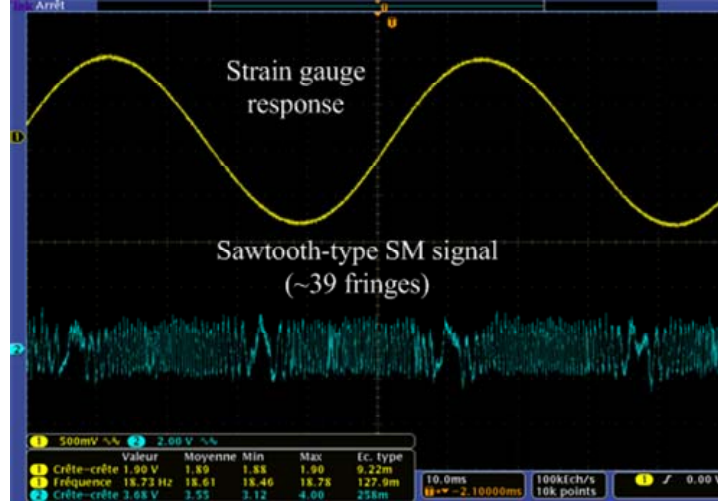


Fig. 3.12. Extending SM-FBG strain sensing to 190 μ strains under modulation scheme

3.5 Conclusion and Perspectives

Exploiting the self-mixing phenomenon for demodulating Bragg wavelength shifts in an FBG device under dynamic strain loading can be highly practical in designing a cost-effective and uncomplicated fiber-based strain sensor. The fundamental principles behind this interrogation technique have been described and include a combination of two individual technologies which have, up to this day, only been employed separately. In addition to the theoretical description and supporting simulation, we have experimentally demonstrated the feasibility of exploiting SM interferometry to interrogate FBGs under dynamic strain-induced perturbations. The strain response has been found to be relatively linear in relation to the wavelength shift of a uniform FBG under strain loading and its variation is found to be proportional to the optical displacement generated due to the grating elongation. This has been competently demonstrated by determining the number of sawtooth fringes detected and subsequently calculating the elongation of the fiber grating in order to extract the desired strain information. Further, comparison with reference strain values measured by a reference deflection sensor corroborates the experimental results thus obtained using the proposed technique. Although relatively large discrepancies have been encountered at the high strain ranges, the current experimental configuration can be further improved by taking into consideration the measured precision of the dimensions of the mechanical parameters employed. The current resolution achievable is $\sim 8 \mu\epsilon$ although this is in relation to the gauge length employed.

In order to extend the dynamic strain range, a modulation scheme is applied to the DFB-LD current in which its wavelength is swept across the FBG spectrum under dynamic strain loading. This ensures that the previously fixed λ_{LD} is never out of range of the displacing FBG spectrum $\delta\lambda_{FBG}$ and subsequently allows the measurement range to be extended by $\sim 50\%$. In addition, we also obtained a slightly improved strain resolution ($\sim 6 \mu\epsilon$) which is suitable for most field applications. Another significant advantage in the SM interrogation scheme relates to the capability of the FBG strain sensor to directly determine directional movement of dynamically-changing measurands without any ambiguity where the symmetrically-opposed inclination of the sawtooth fringes on either half of each period of the measurements corresponds to the

tension/compression exerted on the FBG. Therefore, no further processing techniques are necessary to extract both the strain information as well as its direction.

The proof-of-concept from this preliminary work thus provides the basic framework for carrying out further investigation into a potentially networked or multiplexed sensor system with several FBGs simultaneously interrogated using a single wavelength-modulated laser source and incorporating a more robust signal processing scheme to demodulate SM fringes the individual FBGs. The principal ambition is not to compete with established techniques (for example, Micron Optics interrogation boxes for multiple FBG sensors) but to achieve quasi-distributed sensing on a smaller network scale (of 5–8 FBGs) for monitoring of small civil infrastructures. In addition, the problem of cross-sensitivity to both strains and, in particular, temperature has to be addressed. This sensitivity can be a major inconvenience under certain sensing environments when more than one parameter is present since the resulting λ_B shifts are due to their combined influences. Ambiguities in the measurement of the desired quantity can then arise rendering the process of distinguishing the individual influence from the specific parameter(s) difficult. In most occurrences, thermal fluctuations are the major problem during measurements (which can arise due to source stability, environmental changes, etc). Therefore, if another physical parameter other than temperature is to be monitored, then it is essential to separate the combined contributions, which under certain conditions remains almost impossible. Existing techniques used to compensate temperature influence involve the use of very costly tunable laser sources, multiple overlaid Bragg gratings, reference cavities (which also include Bragg grating-based cavities), etc.

Further, there is also intense interest in long-term monitoring of infrastructures where the mechanical or physical deformation can be slowly-varying as well as being subject to thermal influences. In this case, the possibility of detecting static strains must also be investigated. One potential solution is to further develop the modulation-based SM interrogation scheme to compensate for temperature effects with the inclusion of one FBG dedicated to temperature measurement. Work is also currently ongoing to exploit "exotic" laser diodes with multiple emission wavelengths to interrogate multiple FBG strain sensors for quasi-static strain measurements in field applications.

References

- [1] S. Suleiman, *FBG-based dynamic strain sensors demodulated by self-mixing interferometry*, PhD Thesis, INPT, Dec 2008
- [2] K. O. Hill, Y. Fujii, D. C. Johnson, and B. S. Kawasaki, Photosensitivity in optical fiber waveguides: application to reflection fiber fabrication, *Appl. Phys. Lett.*, vol. 32, pp.647-649, 1978
- [3] K. O. Hill and G. Metz, Fiber Bragg grating technology fundamentals and overview, *J. Lightwave Technol.*, vol. 15, pp. 1263-1276, 1997
- [4] Y. J. Rao, Recent progress in applications of in-fibre Bragg grating sensors, *Opt. Laser Eng.*, vol. 31, pp. 297-324, 1999
- [5] J. M. Lopez-Higuera, Fiber optic sensors in structural health monitoring, *J. Lightwave Technol.*, vol. 29, pp. 587-608, 2011
- [6] B. J. Peng, Y. Zhao, Y. Zhao, and J. Yang, Tilt sensor with FBG technology and matched FBG demodulation method, *IEEE Sensors J.*, vol. 6, no. 1, pp. 63-66, 2005
- [7] Y. Zhao and Y. Liao, Discrimination methods and demodulation techniques for fiber Bragg grating sensors, *Opt. Lasers Eng.*, vol. 41, pp. 1-18, 2004
- [8] Y. N. Ning, A. Meldrum, W. J. Shi, B. T. Meggitt, A. W. Palmer, K. T. V. Grattan and L. Li, Bragg grating sensing instrument using a tunable Fabry-Perot filter to detect wavelength variations, *Meas. Sci. Technol.*, vol. 9, pp. 599-606, 1998
- [9] L. A. Ferreira, J. L. Santos, and F. Farahi, Pseudoheterodyne demodulation technique for fiber Bragg grating sensors using two matched gratings, *IEEE Photon. Technol. Lett.*, vol. 9, pp. 487-489, 1997
- [10] A. D. Kersey, T. A. Berkoff and W. W. Morey, Fibre optic Bragg grating strain sensor with drift-compensated high-resolution interferometric wavelength shift detection, *Opt. Lett.*, vol. 18, pp. 72-74, 1993
- [11] M. Suleiman, A. Ali-Yahia, H. C. Seat, T. Bosch, Interrogation of fiber Bragg grating dynamic strain sensors by self-mixing interferometry, *IEEE Sensors J.*, vol. 8, no.7, pp. 1317-1323, 2008
- [12] G. Plantier, C. Bes and T. Bosch, Behavioral model of a self-mixing laser diode sensor, *IEEE J. Quant. Electron.*, vol. 41, pp. 1157-1167, 2005
- [13] G. Giuliani, M. Norgia, S. Donati and T. Bosch, Laser diode self-mixing technique for sensing applications, *J. Opt. A: Pure and Appl. Opt.*, vol. 4, pp. 283-294, 2002
- [14] A. Yariv, Coupled-mode theory for guided-wave optics, *IEEE J. Quant. Electron.*, vol. QE-9, pp. 919-933, 1973
- [15] T. Erdogan, Fiber grating spectra, *J. Lightwave Technol.*, vol. 15, pp. 1277-1294, 1997
- [16] A. D. Kersey, A. Davis, J. Patrick, M. LeBlanc, K. Koo, C. Askins, M. Putnam, and E. Friebele, Fiber grating sensors, *J. Lightwave Technol.*, vol. 15, pp. 1442-1463, 1997
- [17] G. I. Duck, *Distributed Bragg Grating Sensing-Strain Transfer Mechanics and Experiments*, PhD dissertation, University of Toronto, 2000
- [18] C. D. Butter and G. B. Hocker, Fiber optics strain gauge, *Appl. Opt.*, vol. 17, pp. 2867-2869, 1978
- [19] M. LeBlanc, Y. Huang, M. Ohn, M. Mesures, A. Guemes and A. Othonos, Distributed strain measurement based on a fiber Bragg grating and its reflection spectrum analysis, *Opt. Lett.*, vol. 21, pp. 1405-1407, 1996
- [20] M. Suleiman, H. C. Seat and T. Bosch, Interrogation of fiber Bragg grating dynamic strain sensors by self-mixing interferometry, *IEEE Sensors J.*, vol. 8, pp.1317-1323, 2008
- [21] T. Bosch, N. Servagent and S. Donati, Optical feedback interferometry for sensing applications, *Opt. Eng.*, vol. 40, pp. 20-27, 2001
- [22] L. Goldberg, F. Taylor, A. Dandridge, F. Weller and R. Miles, Spectral characteristics of semiconductor lasers with optical feedback, *IEEE J. Quant. Electron.*, vol. QE-18, pp. 555-564, 1982
- [23] K. Peterman, External optical feedback phenomena in semiconductor lasers, *IEEE Sel. Top. Quant. Electron.*, vol. 1, pp. 480-489, 1995
- [24] R. Tkach and A. Chraplyvy, Regimes of feedback effects in 1.5- μ m distributed feedback lasers, *J. Lightwave Technol.*, vol. 4, pp. 1655-1661, 1986
- [25] G. A. Acket, D. Lenstra, A. J. Den Boef and B. H. Verbeek, The influence of feedback intensity on longitudinal mode properties and optical noise in index-guided semiconductor lasers, *IEEE J. Quant. Electron.*, vol. 20, pp. 1163-1169, 1984
- [26] W. Wang, K. Grattan, A. Palmer and W. Boyle, Self-mixing interference inside a single-mode diode laser for optical sensing applications, *J. Lightwave Technol.*, vol. 12, pp. 1577-1587, 1994
- [27] B. Yun, Y. Wang, A. Li, and Y. Cui, Tunable fiber laser based fiber Bragg grating strain sensor demodulation system with enhanced resolution by digital signal processing, *Microwave and Opt. Technol. Lett.*, vol 48, pp. 1391-1393, 2006
- [28] D. Tosi, M. Olivero and G. Perrone, "Self-mixing based interrogation techniques for high-reflectivity fibre Bragg grating sensors, *Electron. Lett.*, vol. 44, pp. 405-406, March 2008
- [29] W. Xia, M. Wang, Z. Yang, W. Guo, H. Hao, and D. Guo, High-accuracy sinusoidal phase-modulating self-mixing interferometer using an electro-optic modulator: development and evaluation, *Appl. Opt.*, vol. 52, no. 4, pp. B52-B59, 2013

- [30] U. Zabit, O. D. Bernal and T. Bosch, Self-mixing laser sensor for large displacements: signal recovery in the presence of speckle, *IEEE Sensors J.*, vol. 13, no. 2, 2013

Chapter 4 - Research administration

4.1 Introduction

This chapter summarizes the research duties and administrative tasks that I have performed throughout the course of my research career, from PhD supervision to the various research projects that have been awarded. There is also a brief discussion on the various perspectives and/or future work based on my current research activities. Note, however, that this is principally a summary of the different potential possibilities that have already been described in the three preceding chapters.

I have also included a selected list of publications in Section 4.5 while Section 4.6 summarizes my services and duties to the fiber sensing research community. This is followed by a short description of my teaching duties at ENSEEIHT-INPT. Last, but not least, I have included a curriculum vitae which illustrates succinctly my career path in research.

4.2 PhD and Post-Doctoral Supervision

I have supervised 2 PhD students both of whom have defended their work back in Dec 2008. I am currently co-supervising 2 PhD students working on fiber optic sensor projects.

Siegfried CHICOT is currently pursuing his research on the modeling and characterization of photonic crystal fibers for biochemical sensing, a novelty subject within my research group since Oct 2012 while Laura LE BARBIER is working on developing a self-mixing based fiber sensor for measuring very high-velocity impacts and their effects on material behavior.

I have equally supervised 4 MSc research students on various optical signal processing and fiber sensor projects from 2007–2011.

Last, but not least, I have also supervised 5 post-doctoral research fellows who have worked on various projects on fiber sensor research. These are:

- Dr Yue WANG (Oct 2005–Jun 2006)
- current employment: unknown, China
- Dr Mingyi GAO (Oct 2006–Jun 2007)
- current employment: Researcher, National Institute of Advanced Industrial Science and Technology, Tsukuba, Ibaraki, Japan
- Dr Maha SULEIMAN (Mar 2009–Sept 2010)
- current employment: Research Engineer, National Institute for Intense Magnetic Fields, Toulouse, France
- Dr Olivier CARRAZ (Mar 2011–Sept 2012)
- current employment: Researcher, European Space Agency, The Netherlands
- Dr Laurent BOUYERON (Oct 2012–Sept 2013)
- current employment: Research Engineer, CODECHAMP, Limoges, France

1) **Saroj PULLTEAP** (Nov 2004 – Dec 2008): supervisor

Title: Development of an extrinsic dual-cavity fiber Fabry-Perot interferometer: Applications to periodic and non-periodic vibration measurements

Summary: This PhD research primary concerns the further development and characterization of the already-proven dual-cavity extrinsic fiber Fabry-Perot interferometer for periodic and non-periodic vibration measurements. Improvements are made to the optical components employed

in the device to render it more robust and resistant to polarization-induced fading. The principal properties of the interferometer have been determined. A modified fringe-counting technique is also developed to increase the performance of the sensor. A $\lambda/64$ precision has been obtained and the sensor has been successfully tested under various vibration profiles. A further characteristic of the uniquely optical dual-cavity nature of the interferometer manifests itself in its almost infinite bandwidth, hence allowing very fast phenomenon to be measured. Another important work in this PhD research concerns the implementation of a phase-tracking demodulation scheme to demodulate the quadrature interference pair into displacement information. This scheme enables the precision of the sensor to be further improved, subsequently leading to better performance.

PhD Viva: 11 Dec 2008

Viva panel: Y. Gourinat (ISAE)
 K. T. V. Grattan (City University London)
 C. Boisrobert (Univ. Nantes)
 J.-C. Mollier (ISAE)
 M. Cattoen (LAAS-OSE)
 G. Plantier (ESEO)
 P. Ferdinand (CEA-Saclay)
 H. C. Seat (LAAS-OSE)

***Note that Saroj PULLTEAP is today Assistant to the President of Silpakorn University, Thailand**

2) **Maha SULEIMAN** (Apr 2005 – Dec 2008): co-supervisor with T. Bosch (LAAS-OSE)

Title: FBG-based dynamic strain sensors demodulated by self-mixing interferometry

Summary: This PhD research seeks to demonstrate the feasibility of exploiting self-mixing interferometry as a novel technique to interrogate fiber Bragg gratings subject to dynamic strain loading. During strain loading, the back-reflected Bragg wavelength, λ_B , is caused to displace as a function of the loading strength. By optimally positioning the interrogating laser wavelength into the Bragg grating spectrum, the variation of λ_B is then coherently retro-injected into the laser cavity to "interfere" with the existing electric fields. The wavelength-dependent reflectivity from the Bragg grating is investigated as the principal coupling effect into the cavity and integrated as the basic mechanism of the overall C coupling strength within the cavity fields. This interaction leads to the emission of a series of sawtooth-type fringes, which is widely recognized as the phenomenon of "self-mixing". Demodulation of the detected fringes by simple fringe or phase demodulation then enables the desired parameter to be extracted. Although the initial detection scheme based on a fixed laser wavelength leads to a limited dynamic strain range corresponding to the spectrum width of the FBG, preliminary work has been explored in this thesis on improving this measurement range by scanning the interrogating wavelength across and beyond the FBG spectrum. An improvement of at least 50% has been demonstrated.

PhD Viva: 11 Dec 2008

Viva panel: C. Boisrobert (Univ. Nantes)
 N. Butterlin (ISIFC)
 D. Leduc (Univ. Nantes)
 C. Fontaine (LAAS)
 P. Ferdinand (CEA-Saclay)
 J.-C. Mollier (ISAE)
 T. Bosch (LAAS-OSE)
 H. C. Seat (LAAS-OSE)

3) **Siegfried CHICOT** (Oct 2012 –): co-supervisor with M. Cattoen & O. Bernal (LAAS-OSE)

Title: Analysis, modeling and characterization of photonic crystal fibers for fiber optic sensing applications

Summary: This PhD research is principally geared towards the study and modeling of photonic crystal fibers (PCFs) via finite element or effective index methods in order to analyze and characterize specific properties which can contribute to validating the proposed theoretical model. The outcome of these preliminary studies will be exploited in the development of fiber sensors based on PCFs for applications in biochemistry in the medical domain, for example, for the detection of cancerous protein molecules via chirality measurement. Although PCFs were initially designed for fiber optic telecommunications due to their endlessly single mode behavior, dispersion compensation ability, very high power density threshold, etc, they are increasingly being exploited for metrological applications where the presence of air-holes render these devices particularly advantageous such as their potential insensitivity to temperature variations. A series of experiments will also be carried out to validate the proof-of-concept of the studied technique.

PhD Viva: Expected end 2015

Viva panel: NA

4) **Laura LE BARBIER** (Dec 2012 –): co-supervisor with T. Bosch (LAAS-OSE) & J. Luc (CEA-Gramat)

Title: Development of an optoelectronic interferometric sensor for the study of material dynamics via velocity measurements

Summary: The research work consist of developing a novel bulk or fiber optical interferometer to measure the velocity of materials subjected to shocks (plane shock, isentropic compression, etc) in the mm/s to 10 km/s range. The interferometer will be employed in 2D measurements of velocity profiles with sufficient spatial and temporal resolution to understand the various phenomena under investigation. The principle objective is to obtain and correlate the experimental characteristics to optimize numerical simulation codes currently employed in material dynamics studies. Spectrograms obtained using time-frequency analysis of interference signals will also be investigated to quantify any eventual ejectas (particles) from the resulting shocks in order to reverse-calculate the original particle characteristics. An experimental test bench will be setup to achieve theses objectives.

PhD Viva: Expected end 2015

Viva panel: NA

4.3 Research Projects and Collaborations

This section lists the research projects in which I have participated, essentially as Principal Investigator (PI). They are listed chronologically without any distinction on the type of projects.

International, National and Regional Projects

1. *In-situ cure monitoring and post-cure characterisation of advanced fibre-reinforced composite materials with optical and fibre sensors*

Objective: Design and development of fiber optic sensors for characterization of nanoparticle reinforced composite panels during synthesis and post-fabrication.

International *MERLION* program funded by French Ministry of Foreign Affairs (2007–2008)

Collaboration: LAAS-OSE – IMRE (Institute of Materials Research and Engineering, Singapore)
Capacity: PI
Funding budget: 30k€

2. **Laser INterferometry for Earth Strain (*LINES*): *Development of fiber interferometric sensors for geophysics applications***

Objective: Design and development of high-resolution high-precision extrinsic fiber Fabry-Perot interferometer for remote sensing (baseline 120–3000 m) in geophysics: long baseline inclinometry, pendulum-based tiltmetry and seismometry for natural risk assessment.

French National Research Agency (*ANR*) Natural Risks program (2008–2012)
Collaboration: LAAS-OSE – Institut de Physique du Globe de Paris (IPGP) – Géosciences Montpellier (GM) – Ecole Supérieure d'Electronique de l'Ouest ESEO Angers – Géosciences Azur and 2 industrial partners in support (Total & Schlumberger)
Capacity: PI for LAAS-OSE
Funding budget: 550k€

3. ***Microlaboratoires d'Analyses In Situ pour des Observatoires Environnementaux (MAISOE): Development of a fiber optic micro-system for in-situ detection of methane in hydrothermal fluids***

Objective: Design and development of fiber optic sensors for undersea detection of dissolved methane gas under the "long-term development" program.

French Regional RTRA STAE Research program (2009–2013)
Collaboration: LAAS-OSE – LCA – LAAS – CIRIMAT – LEGOS – LGC – GET
Capacity: PI for LAAS-OSE
Funding budget: 1.2M€

4. ***Feasibility studies of a fiber optic gravimetric wave detector***

Objective: Feasibility studies of exploiting a laser diode-based fiber Fabry-Perot interferometric sensor to develop a novel gravimeter wave detector with 10 μ Gal precision

Geophysics research project funded by CNRS INSU (2013–2014)
Collaboration: LAAS-OSE – GM
Capacity: member
Funding budget: 7k€

5. ***Development of a prototype HLS-LINES for accelerator alignment at the CERN***

Objective: Development of Long Baseline Inclinometer from LINES project for compensation of earth tilt in accelerator alignment at CERN

Development project funded by SATT TTT (2014–)
Collaboration: LAAS-OSE – GM – CERN – SATT TTT – SATT AxLR
Capacity: PI
Funding budget: ~100k€

6. ***PROfiling METHane Emission in the Baltic sea: Cryptophane as in-situ chemical Sensor***

Objectives: PROMETHEUS seeks to further develop the fiber optic-based refractometer for dissolved methane detection in subsea zones by improving the current sensor architecture and reinforcing its robustness together with better design of molecular receptors for methane capture. The final ambition of this project is the deployment of a functioning prototype fiber-based CH₄ sensor to the Institut Océanographique de Warnemünde (IOW)-managed GODESS oceanic platform in the Baltic Sea, Germany.

French National Research Agency (ANR) International program (2014–2017)

Collaboration: GET OMP – LAAS-OSE – LC ENS Lyon – IOW

Capacity: PI for LAAS-OSE Group

Funding budget: 272k€

Local BQR projects

7. *Intelligent signal processing for an embedded system for vibrational analysis by fiber optic interferometry*

Objective: Development of signal processing scheme for dual-cavity extrinsic fiber Fabry-Perot interferometric sensor with applications to vibration analysis.

Local BQR program funded by INPT (2006–2007)

Collaboration: LAAS-OSE– IRIT – LAAS-DISCO

Capacity: PI

Funding budget: 26k€

8. *Development of an embedded micro-system exploiting fiber Bragg grating sensors for the characterization of composite materials, quality control and intelligent signal processing of fiber Bragg gratings*

Objectives: Design and development of embedded fiber Bragg grating strain sensors for characterizing composite materials during fabrication, development of interrogation and demodulation scheme for fiber Bragg gratings under dynamic strain loading.

2 Local BQR programs funded by INPT (2007–2009)

Collaboration: LAAS-OSE– LAAS-DISCO – IRIT

Capacity: PI

Funding budget: 31k€

9. *Development of novelty FBG-based sensors and novelty interrogation techniques quasi-static and dynamic strain detection in structural monitoring of civil infrastructures and advanced composite materials*

Objective: Development of novel interrogation technique based on bi and tri-mode lasers for fiber Bragg grating strain sensors with applications to structural health monitoring of small civil infrastructures

2 Local BQR International Mobility programs funded by INPT (2010–2011)

Collaboration: LAAS-OSE – ISRC (Instrumentation and Sensors Research Center, City University London, UK)

Capacity: PI

Funding budget: 3.1k€

10. *Simulation and model optimization and experimental validation of optical and hyper-frequency waveguides*

Objective: Conception of mathematical model for behavioral modeling of photonic crystal fibers for optical metrology in biochemical environments

Local BQR program funded by INPT (2013–2014)

Collaboration: LAAS-OSE – LAPLACE-GRE – IMT

Capacity: responsible for photonic crystal fibers

Funding budget: 16k€

4.4 General Perspectives and Future Work

As described in Chapter 2, two variants of the EFFPI sensor have been developed for vibration and displacement measurements.

The polarization-based dual-cavity EFFPI possesses a potentially very large bandwidth and is thus highly suitable for very fast displacement measurements since no modulation scheme is involved. By exploiting the modified fringe-counting demodulation technique, the interferometer has also been demonstrated to be sufficiently robust for tracking displacements of various profiles. The sensor's minimum detectable displacement, on the other hand, is ultimately limited, intrinsically, to only $\lambda/2$.

The dual-cavity EFFPI sensor is currently being adapted for gravitational wave measurements with the aim of tracking the free-fall of a mass released from a pre-determined height to calculate the gravity profile. The attractiveness of such a system lies in the simplicity and geometrical flexibility of an LD-illuminated fiber sensor with interferometric precision. The fiber sensor is to be integrated into a vacuum filled free-fall drop mechanical set-up which will also incorporate a seismometer for parasitic vibration compensation of the natural ground movement. In comparison with a conventional absolute gravitational wave detector which requires very stringent alignment procedures, implicating a long preparation time, the EFFPI sensor system can be rapidly set-up. More importantly, remote measurements can be achieved, allowing the fiber-based gravitational wave detector to be deployed to isolated and hostile sites. Amongst the applications targeted, the device is principally designed for monitoring volcanic activities before eruption as well as in geodesic measurements for tracking water reserves which are becoming a scarce commodity. Another perspective is in the petrochemical sector for monitoring oil wells as well as prospection in remote zones where these devices can be installed in networks. The EFFPI sensor is undergoing initial testing in feasibility studies for gravitational wave detection in collaboration with colleagues from Géosciences Montpellier (supported by a CNRS INSU grant).

Although, the modulation-based EFFPI has been specifically designed for applications in geophysics, its application field is, nonetheless, wide-ranging. As a metrological tool, the EFFPI sensor is robust and exhibits performance suitable for industrial measurements of thickness variation in semiconductor wafers during production. We are currently in negotiation with FOGALE for a technology transfer scheme in this application field. We are also in talks with ISP System for an eventual technology transfer of the sensor as a high-precision metrological tool. In geophysics, the ILB-LINES system is undergoing development into a pre-industrial product with the support of SATT TTT (Société d'Accélération du Transfert de Technologies Toulouse Tech Transfer). The prototype sensor will be evaluated by the CERN in field trials before being exploited for precise alignment of its particle accelerators for nuclear research in a radioactive environment. Again, the advantage of remote sensing is cited here as a major advantage where the sensor electronics can be installed in an isolated and protected area. Further, another ILB-LINES system will be developed to cater to needs in the petrochemical industry for oil well and underground gas storage monitoring, in collaboration with TIGF (Transport Infrastructures Gaz France)

The IF-LINES system (borehole tiltmeter) is currently on standby for a technology transfer program to Pinnacle, Inc, a subsidiary of Haliburton due to its novelty design and performance achieved by interferometric precision with fiber optic sensor probes.

SISMO-LINES, the fiber-based seismometer, is currently under development into a 3-axis seismometer system for subsea applications in both geophysics research and petrol exploration (supported by another CNRS INSU grant). One perspective of the modulation-based EFFPI sensor is to implement autonomous operation capability in the current system for deployment to remote terrains without any power supply. One of the development paths under consideration is integrating 12 or 24 V power supplies typically provided by batteries and/or solar cells for fully autonomous operation in remote zones (for example the Chilean and sub-Saharan deserts, offshore sites and oil fields).

Another constraint of the current sensor is in its relative displacement measurement capacity. Hence, when the system is disrupted due to power cut-off, difficulty will arise in assessing the previous position of the measurement before power failure. The measurements will thus have to recommence from zero. A potential perspective would be to orientate the modulation-based EFFPI sensor for absolute measurements (i.e. distance). A means to the evolution towards absolute sensing would be by exploiting the synthetic wavelength generated during the modulation scheme to achieve distance measurement capability. In this case, the interrogating wavelength will have to be guaranteed to the fm (femtometer) order and a very high stability will have to be ensured for long-term sensor operation. Work is currently under way to assess the feasibility of an absolute system without incurring heavy expenses. A further perspective is to implement the above instruments in a sensor network which can then provide large geographical coverage for natural risk monitoring of earthquakes, volcanic eruptions, etc.

The proof-of-concept in exploiting self-mixing interferometry for interrogating FBGs under mechanical loading for strain sensing has been amply demonstrated in Chapter 3. Further, the dynamic strain range can be extended by more than 50% by using low-frequency modulation of the DFB-LD current to sweep the interrogating wavelength across the FBG spectrum under dynamic strain loading. Hence, λ_{LD} is never out of range of the displacing FBG spectrum $\delta\lambda_{FBG}$. Also, a strain resolution of $\sim 6 \mu\epsilon$ is obtained which is suitable for most field applications.

A future challenge is to develop a multiplexed sensor system for interrogating multiple FBGs with a single wavelength-modulated laser source. The fringe counting technique used in processing the detected SM fringes limits the precision of the current system and has to be replaced by a more robust signal processing scheme dedicated to demodulating the individual FBGs via the detected phase variation. In addition, FBGs are sensitive to both strains and, in particular, temperature. This cross-sensitivity is a major inconvenience that has to be compensated/eliminated to distinguish the influencing physical parameters so that true measurements (strains) can be accurately carried out. One perspective is to extend the scanning of the interrogating wavelength so that 2 or more FBGs can be monitored. This will involve the use of DBR-based lasers which can afford a larger wavelength excursion compared to the DFB-LD currently used. Hence, if one FBG is under uniquely thermal influence while the rest subject to both influences, then temperature effects can be compensated. Work is also currently ongoing to exploit "exotic" laser diodes with multiple emission wavelengths to interrogate multiple FBG strain sensors for quasi-static strain measurements in field applications.

Another long term perspective is the development of metrological systems based on photonic crystal fibers (PCFs). Particular emphasis will be placed on biochemical and gas sensing applications in the biopharmaceutical and environmental domains. The ultimate ambition of this PhD project is to develop a prototype PCF-based gas and biochemical sensor for in-situ measurements.

PCFs, also commonly known as microstructured, holey or photonic bandgap fibers, can be classed into solid-core PCFs, where waveguiding is via modified total internal reflection (similar to conventional fibers) due to a periodic modulation of the refractive index (RI) in the cladding region and hollow-core PCFs where light is guided along the length of the air hole by the photonic bandgap effect, which will only allow certain modes within a spectral bandwidth to be propagated. Another property of prominence in index-guided PCFs is their endlessly single-mode propagation characteristics. The RI in PCFs is represented by an effective index $n_{\text{cleff}}(\lambda)$ due to the air hole-silica geometry and can be configured for a specific band of wavelengths since n_{cleff} is wavelength dependent. Initial work will essentially concentrate on analyzing the evanescent wave penetration depths into the transverse fiber structure since the propagation of evanescent fields is, in turn, strongly dependent on $n_{\text{cleff}}(\lambda)$ in the cladding. This research is thus concerned with designing PCFs to exhibit strong leakage of the evanescent fields in the presence of RI variation, together with identifying ways to enhance their sensitivity to biochemical agents/molecules and gases in the context of the ANR PROMETHEUS project on the detection of dissolved methane gases in aqueous environments.

Another set of optical properties achievable in PCFs concern their polarization state conservation and extremely high birefringence, which is of the order of 0.001 to 0.01 ($>10^2$ times higher than in standard optical fibers). Consequently, these specifically-designed PCFs can allow the propagation of single-mode lightwave without altering the original polarization state. Hence, due to this polarization "passivity", the PCF can be used to transmit, without polarization transformation, any eventual shift in the polarization state of the reflected lightwave which comes into contact with certain biomolecules. This is particularly applicable to enantiomers which are mirror images of the same molecule presenting a specific optical rotation with respect to its dipole orientation. The chiral nature of certain molecules can be of critical importance since, in general, only one enantiomer is biologically safe and beneficial in the synthesis of medical drugs. The mirror-image twin, on the other hand, which has opposite chirality, can be potentially harmful. Thus probing molecular chirality can have a serious implication in the pharmaceutical industry. The role of PCF-based chiral sensors can thus be advantageous since they can be exploited for analyzing small sample volumes of the analytes in-situ during production.

4.5 Publications

4.5.1 Patent Application

- [1] "Dispositif à fibre optique extrinsèque pour la mesure d'un paramètre physique", M. Cattoën & H. C. Seat, FR10 56230, 28/07/2010 (patent pending)

Patent Family (27/07/2011)

US 13/810, 453 (patent pending)

EP 11738699.5 (patent pending)

JP PCT/EP2011/062890 (patent pending)

4.5.2 Journal Papers

- [1] J. H. Sharp, C. W. P. Shi & H. C. Seat, Er-doped sapphire fibre temperature sensors using upconversion emission, *Measurement + Control*, vol. 34, no. 6, pp. 170-171, 2001
- [2] H. C. Seat, J. H. Sharp, Z. Y. Zhang & K. T. V. Grattan, Single-crystal ruby fiber temperature sensor, *Sensors Actuators A*, vol. 101, pp. 24-29, 2002
- [3] H. C. Seat & J. H. Sharp, Er³⁺+Yb³⁺-codoped Al₂O₃ crystal fibres for high temperature sensing, *Meas. Sci. Technol.*, vol. 14, pp. 279-285, 2003

- [4] H. C. Seat, E. Ouisse, E. Morteau & V. Métivier, Vibration-displacement measurements based on a polarimetric extrinsic fibre Fabry-Pérot interferometer, *Meas. Sci. Technol.*, vol. 14, pp. 710-716, 2003
- [5] H. C. Seat, A pseudo-dual cavity extrinsic fibre Fabry-Pérot interferometric vibrometer, *Sensors Actuators A*, vol. 110, no. 1-3, pp. 52-60, 2004
- [6] H. C. Seat & J. H. Sharp, Dedicated temperature sensing with c-axis oriented single-crystal ruby ($\text{Cr}^{3+}:\text{Al}_2\text{O}_3$) fibers : Temperature and strain dependences of R-line fluorescence, *Special Joint Issue IEEE Trans. on Instrum. Measure. & J. of Lightwave Technol.*, 53, no. 1, pp. 140-154, 2004
- [7] J. H. Sharp, C. W. P. Shi, I. A. Watson & H. C. Seat, Production and applications of single crystal optical fibres, *Asian J. Phys.*, vol. 15, no. 3, pp. 233-242, 2006
- [8] S. Pullteap, H.C. Seat & T. Bosch, Modified fringe counting technique applied to a dual-cavity fiber Fabry-Perot vibrometer, *Opt. Eng.*, vol. 46, n°11, pp 115603/1-8, 2007
- [9] M. Suleiman, H.C. Seat & T. Bosch, Interrogation of fiber Bragg grating dynamic strain sensors by self-mixing interferometry, *IEEE Sensors J.*, vol. 8, n°7, pp 1317-1323, 2008
- [10] W. Khunsin, A. Amann, G. Kocher-Oberlehner, S. G. Romanov, S. Pullteap, H. C. Seat, E. P. O'Reilly, R. Zentel and C. M. Sotomayor Torres, Noise-assisted crystallization of opal films, *Adv. Funct. Mater.*, vol. 22, pp. 1812-1821, 2012 (DOI: 10.1002/adfm.201102605)
- [11] P. Chawah, A. Sourice, G. Plantier, H. C. Seat, F. Boudin, J. Chéry, M. Cattoen, P. Bernard, C. Brunet, S. Gaffet, and D. Boyer, Amplitude and phase drift correction of EFPI sensor systems using both adaptive Kalman filter and temperature compensation for nanometric displacement estimation, *J. Lightwave Technol.*, vol. 30, no. 13, pp. 2195-2202, 2012
- [12] H. C. Seat, P. Chawah, M. Cattoen, A. Sourice, G. Plantier, F. Boudin, J. Chéry, C. Brunet, P. Bernard and M. Suleiman, Dual-modulation fiber Fabry-Perot interferometer with double reflection for slowly-varying displacements, *Opt. Lett.*, vol. 37, no. 14, pp. 2886-2888, 2012

4.5.3 Conference Papers (Selected)

- [1] H. C. Seat & J. H. Sharp, *Single-crystal fibres for sensor applications* in: *In-Fibre Bragg Gratings and Special Fibres*, Half-Day Meeting of the Optical Group of the Institute of Physics (Invited), London (G. B.), 3, 12 May 1999
- [2] J. H. Sharp, H. C. Seat, Z. Y. Zhang & K. T. V. Grattan, *Single-Crystal Ruby Fibres for Fluorescence-Based Temperature Sensing*, *Sensors and their Applications X*, N. M. White and A. T. Agosti (Eds.), IOP Publishing, ISBN 0-7503-0662-9, 219, Cardiff (UK), 5-8 Sept 1999
- [3] J. H. Sharp & H. C. Seat, *Temperature and strain characteristics of ruby fibre fluorescence emission*, OFS14, Venice (Italy) Proc. SPIE, vol. 4185, p. 54, 11-13 Oct 2000
- [4] H. C. Seat, E. Ouisse, V. Métivier & E. Morteau, *Demonstration of a dual-cavity extrinsic fibre Fabry-Pérot interferometer for vibration-displacement measurements*, 5th Int'l Conf. on Vibration Measurements by Laser Techniques, Ancona (Italy), Proc. SPIE, vol. 4827, p. 298, 5-6 Nov 2002
- [5] H. C. Seat & J. H. Sharp, *$\text{Er}^{3+}+\text{Yb}^{3+}$ -codoped Al_2O_3 crystal fibres for high temperature sensing*, 16th Europ. Conf. on Solid-State Transducers, Prague (Czech Rep.), Proc. Eurosensors XVI, vol. 2 (TP38), p. 661, 15-18 Sept 2002
- [6] V. Métivier, E. Morteau, E. Ouisse & H. C. Seat, *Dual-cavity extrinsic fibre Fabry-Pérot interferometer for vibration-displacement measurements*, 16th Europ. Conf. on Solid-State Transducers, Prague (Czech Rep.), Proc. Eurosensors XVI, vol. 1 (M3A3), p. 383, 15-18 Sept 2002
- [7] H. C. Seat, *A non-ambiguous fibre-based vibrometer with potential polarisation-induced fading compensation*, 4th Top. Meet. on Optoelectronic Distance/Displacement Measurement and Applications, Oulu (Finland), Proc. ODIMAP IV, pp. 54-59, 16-18 Jun 2004
- [8] H. C. Seat, *An extrinsic fibre optic interferometer with possible signal fading compensation for vibrometric applications*, IEEE Instrumen. Measure. Technol. Conf., Proc IMTC 2005, vol. 3, pp. 2236-2241, Ottawa (Canada), 16-19 May 2005
- [9] H. C. Seat, Y. Wang, T. Bosch & W. Hu, *Self-mixing-based demodulation technique for dynamic fiber Bragg grating strain sensors*, IEEE Instrument. Measure. Technol. Conf. 2006, Proc. IEEE IMTC 2006., pp. 1-5, Sorrento (Italy), 24-27 Apr 2006

- [10] S. Pullteap, H.C. Seat & T. Bosch, *Reflectance characterisation of a fibre optic interferometer for displacement determination in vibration analysis*, 5th Top. Meet. on Optoelectronic Distance/Displacement Measurement and Applications, Proc. ODIMAP V, pp. 27-32, Madrid (Spain), 2-4 Oct 2006
- [11] S. Pullteap, H.C. Seat & T. Bosch, *Temperature and distance dependant errors in a dual cavity fibre Fabry-Perot interferometer for vibration analysis*, IEEE Instrumen. Measure. Technol. Conf. 2007, Proc. IEEE IMTC 2007, pp. 1-6, Warsaw (Poland), 1-3 May 2007
- [12] H.C. Seat & S. Pullteap, *An extrinsic fiber Fabry-Perot interferometer for dynamic displacement measurement*, IEEE Int'l Conf. on Mechatronics and Automation 2007, Proc. IEEE ICMA 2007, pp. 3027-3032, Harbin (China), 5-8 Aug 2007
- [13] H. C. Seat, M. Suleiman & T. Bosch, *Demodulation of fiber Bragg grating wavelength shifts by optical feedback interferometry*, Adv. Laser Techniques, Proc. SPIE, vol. 7022, 70220F (published June 2008), DOI 10.1117/12.803923, Levi (Finland), 3-7 Sept 2007
- [14] S. Pullteap & H. C. Seat, *Dynamic displacement measurements with a dual-cavity fiber Fabry-Perot interferometer*, Int'l Workshop and Conf. on Photonics and Nanotechnology, Proc. SPIE, vol. 6793, 67930A (published Mar 2008), DOI 10.1117/12.798958, Pattaya (Thailand), 16-18 Dec 2007 (awarded Third Prize for Oral Presentation)
- [15] M. Suleiman, H.C. Seat & T. Bosch, *Remote fiber Bragg grating strain sensing by self-mixing interferometry*, 3rd Int'l Conf. on Information and Communication Technologies: From Theory to Applications, Proc. IEEE ICTTA 2008, pp. 1-6, Damascus (Syria), 7-11 Apr 2008
- [16] S. Pullteap, H.C. Seat, M. Cattoen, P. Bernard, J.-C. Lépine, F. Boudin, J. Chéry & T. Bosch, *A phase-tracking fiber interferometer for seismologic applications*, IEEE Sensors 2008 Conference, Proc. of the 7th IEEE Conference on Sensors, Lecce (Italie), pp.938-941, 26-29 Oct 2008
- [17] M. Suleiman, H. C. Seat & T. Bosch, *FBG-based dynamic strain sensors demodulated by self-mixing interferometry: Improving strain measurement resolution*, IEEE Instrum. and Measure. Technol. Conf. 2009, Proc. IEEE IMTC 2009, pp. 332-336, Singapore (Singapore), 5-7 May 2009
- [18] T. B. Pham, H. C. Seat, O. Bernal & M. Suleiman, *A novel FBG interrogation method for potential structural health monitoring applications* (Invited Special Session), IEEE Sensors Conf. 2011, Proc. IEEE Sensors 2011, pp. 1341-1344, Limerick (Ireland), 28-31 Oct 2011 (sponsored by EU COST TD1001 program)
- [19] J. Chery, F. Boudin, M. Cattoen, H. C. Seat, M. Suleiman, P. Chawah, G. Plantier, A. Sourice, P. Bernard, C. Brunet, S. Gaffet, D. Boyer, *High resolution tiltmeters and strainmeters based on extrinsic fiber Fabry-Perot interferometry: the LINES project*, AGU Fall Meeting, San Francisco (USA), 5-9 Dec 2011
- [20] C. Boulart, O. Carraz, H. C. Seat, V. Chavagnac, *Tracking methane in the deep sea: A new in situ chemical sensor for deep sea hydrothermal vent exploration*, Deep-Sea and Sub-Seafloor Frontier Conference, Barcelona (Spain), 11-14 Mar 2012
- [21] J. Chery, F. Boudin, M. Cattoen, H. C. Seat, P. Chawah, G. Plantier, A. Sourice, P. Bernard, C. Brunet, S. Gaffet, D. Boyer, *A new class of tiltmeters and seismometers based on optic fiber Fabry-Pérot interferometry: results and use for active tectonics*, WEGENER 2012, Strasbourg (France), 17-20 Sept 2012
- [22] S. Aouba, C. Boulart, O. Carraz, Ph. Arguel, M. Aufray, Ph. Behra, O. Bernal, A. Castillo, M. Cattoen, V. Chavagnac, B. Dubreuil, J. -P. Dutasta, F. Lozes, P. Gisquet, H. C. Seat, *Emerging technologies for in-situ dissolved methane measurements*, Gordon-like Conference, Anglet (France), 23-28 Sept 2012
- [23] J. Chery, F. Boudin, H. C. Seat, M. Cattoen, P. Chawah, G. Plantier, A. Sourice, P. Bernard, C. Brunet, S. Gaffet, D. Boyer, *Detecting Aseismic Transient Motion on Faults Using New Optical Tiltmeters and Seismometers*, AGU Fall Meeting San Francisco (USA), 3-7 Dec 2012
- [24] T. B. Pham, O. Bernal, H. C. Seat, F. Surre & T. Bosch, *Self-mixing sensing under strong feedback using multimode semiconductor lasers*, ThF3-2, CLEO Pacific Rim, Kyoto (Japan), 21-23 Jul 2013
- [25] L. Le Barbier, J. Luc, H. C. Seat, T. Bosch, *Etude du principe de la rétro-injection optique pour la mesure de hautes vitesses en dynamique des matériaux*, 13th CMOI 2013, Orléans (France), 18-22 Nov 2013
- [26] L. Bouyeron, A. Lefrançois, J. Luc, H. C. Seat, *Modélisation du comportement dynamique d'un capteur à réseau de Bragg pour la mesure de pression en détonique*, 13th CMOI 2013, Orléans (France), 18-22 Nov 2013

4.5.4 Invited Seminars & Miscellaneous

- [1] "Capteurs à Fibres Optiques", "Microlaboratoires d'analyses in situ pour des observatoires environnementaux" Workshop, Boussens, France (22-23 Apr 2008)
- [2] *Fiber interferometers for seismology and fiber Bragg grating sensors demodulated by optical retro-injection*, Institute of Materials Research & Engineering (IMRE), Singapore (05 Feb 2009)
- [3] *Fiber optic sensors for geophysics and strain measurements*, 4th Technical Meeting, COST ACTION TD1001, Aston University, United Kingdom, 3-4 May 2012
- [4] "Les espions qui écoutaient la fibre optique", Sciences et Avenir Magazine, pp. 82-84, April 2014

4.6 Administrative Duties and Service to the Community

One of my fundamental research duties include reviewing for various journals on fiber optic and optical sensors:

- IEEE J. Quant. Electron.
- IEEE I&M Magazine
- IEEE Trans. Instrum. Measurement
- IEEE Sensors J.
- Sensors & Actuators A
- J. Lightwave Technol.
- Opt. Laser Eng.
- Opt. Eng.
- Meas. Sci. and Technol.
- J. Opt. A

I have been Scientific Assessor for the Belgian ARC Project proposal entitled "*Optical-fibre-based vibration Sensors for Industrial Measurement and Biomedical Applications (SIMBA)*". I have been on the PhD Viva panel of Dr Patrick CHAWAH as well as being member of the DRT Viva panel of Mr Nicolas PERAUD. I am currently a serving member of the ENSEIHT-INPT evaluation panel for the recruitment of Assist. Profs. under the 61/63 Section.

I am also currently serving on the Technical Committee board of the IEEE International Conference on Photonics and the IEEE International Conference on Sensing Technology.

I also participate in the COST Action TD1001 program for "Novel & Reliable Optical Fibre Sensor Systems for Future Security & Safety Applications" as substitute member representing France. Further, in collaboration with Dr F. SURRE of City University, I am organizing the Final Technical Meeting of COST TD1001 in conjunction with a Workshop on fiber optic sensors for safety and security in autumn 2014.

4.7 Teaching Duties

Since my appointment to ENSEIHT-INPT, I have been involved in teaching various subjects with a total number of teaching hours varying from 200 – 250 hrs per year. Below is a list of subjects I teach, including lectures, tutorials and laboratory classes within the Electronics Department:

- **Optoelectronics:** ENSEIHT & Masters Programs
 - practical laboratory class for 2nd Yr students
 - design of fiber optic experiments for 2nd Yr students (chromatic dispersion, optical losses in fibers, fiber optic Michelson interferometer): I have been in charge of the Optoelectronics Laboratory class for 2nd Yr students
 - lectures for MNS Masters students (Photonic Systems)

- lectures for MEMO Masters students (Photodetection)
- lectures for M2 ICES Masters students (principles of optics and fiber optic sensors)
- design of laboratory work for M2 ICES
- **Analog Electronics:** ENSEEIHT
 - tutorial class in linear electronics for 1st Yr students
- **Digital Electronics:** ENSEEIHT
 - practical laboratory class for 1st Yr students
 - principles of digital electronics and components, conception of digital circuits
 - design and validation of digital circuits with VHDL
- **VHDL Digital Electronics Design:** ENSEEIHT
 - practical laboratory class for 2nd Yr students
 - synthesis and modeling of digital components with VHDL
- **Object-Oriented Programming with MS Visual C++:** ENSEEIHT
 - practical laboratory class for 2nd Yr students
 - numerical analysis of 1st and 2nd order electronic circuits with objected oriented C++
- **Supervision of 2nd and 3rd (final) year projects:** ENSEEIHT
 - association of student projects to on going research activites on fiber optic sensors: design and modeling of fiber optic refractometer and EFFPI sensor

4.8 Curriculum Vitae

Han Cheng SEAT

5 rue Daniel Sorano
31100 Toulouse
France

Tel : +33.(0)5.34.32.25.61 (work)

Fax : +33.(0)5.34.32.25.68 (work)

Email: seat@enseeiht.fr (work)

Nationality : Singapore Citizen

Date of Birth : 5th June 1972

Residency Status : French Permanent Resident

***Note** : Free from further military obligations
(Military service completed : 2 ½ yrs)



EMPLOYMENT & WORK EXPERIENCES

09/2003– Assistant Professor (Faculty Position)
Optoelectronics for Embedded Systems Group of the Laboratory for Analysis and Architecture of Systems (LAAS-OSE), ENSEEIHT–INPT, France

Research

- Supervision of 1 PhD student and co-supervision of 3 PhD students (2004–)
- Supervision of 5 Post-Doctoral Fellows (2005–2013)
- Supervision of 4 MSc students (signal processing and fiber optic sensors; (2007–2011)
- R & D in high-precision, high-resolution fiber optic interferometric techniques
- PI in MERLION Project, ANR LINES and PROMETHEUS Projects and Regional MAISOE Project

Teaching

- Lectures: optoelectronics , fiber optic sensors at MEng level
- Tutorials & demonstration labs: analogue and digital electronics, C++ object-oriented programming, VHDL project, semiconductor physics, fiber optic sensors at MEng level
- Total teaching volume 200–250 hrs/yr

09/2002–08/2003 Research Engineer

Détecteurs Group, Laboratoire SUBATECH, Ecole des Mines de Nantes (EMN), France

- Design of fiber sensor system for high-energy particle detection (x and soft- γ rays) based on scintillating crystals and crystal fibers (collaboration with *LOSEC*, Glasgow University)
- R & D in fiber optic interferometric sensors for precision mechatronics
- Co-supervision of 1 PhD student

10/2001–08/2002 Post-Doctoral Research Fellow
Instrumentation et Capteurs Group, EMN, France

- Lead R&D in fiber optic interferometric sensors
- Design of dual-cavity extrinsic fiber Fabry-Perot interferometric (EFFPI) sensor
- Supervision of 2nd Yr group projects (fiber optic sensing), management of project resources and security measures
- Co-supervision of 1 PhD student

10/1997–05/2001 PhD Student
Laser and Optical Systems Engineering Centre, Glasgow University, UK

- Fabrication of doped and undoped single-crystal fibers by *laser-heated pedestal growth* (LHPG)
- Characterization of crystal fibers for sensing applications in extreme environments
- Design of thermometric, strain and bend crystal fiber sensing systems
- Co-supervision of Final Year Undergraduate Projects (BEng. Hon.) + 1 PhD
- First reported growth of rare-earth doped sapphire crystal fibers by LHPG technique

Teaching

- 2nd and 3rd Yr Dynamics laboratory (software packages: DADS et IDEAS)
- 3rd Yr LabVIEW Instrumentation laboratory
- Tutorial classes for 1st and 2nd Yr Thermodynamics

EDUCATION AND QUALIFICATION

10/1997–06/2001 PhD in Eng. (pass without corrections¹) – University of Glasgow (UK), *Laser and Optical Systems Engineering Centre (LOSEC)*

Title : ***“Growth and Characterisation of Single-Crystal Fibres for Sensing Applications”***

10/1994–07/1996 B.Eng in Mech. Eng. (1st Class Honours) – University of Glasgow (UK)
Final Year Project : ***“Laser Welding of Magnetic Materials”*** (see AWARDS/GRANTS)

07/1989–05/1992 Diploma in Mech. Eng. – Singapore Polytechnic

AWARDS & GRANTS

10/2013 NOVELA Toulouse for Innovation (on modulation-based EFFPI sensor)

10/2012 Laurier INPT for Patent Application on modulation-based EFFPI sensor

10/2001 - 08/2002 Post-Doctoral Research Scholarship, *“Région des Pays de la Loire”*, FR

10/1997 - 09/2000 Overseas Research Scholarship (ORS) Award, Committee of Vice Chancellor and Principals (CVCP), UK

10/19/97 - 09/2000 Engineering Faculty Research Scholarship, University of Glasgow

07/1996 Institution of Mechanical Engineers (IMechE) Best Project Prize

¹ PhD Grade in UK : 1) Pass without corrections ; 2) Pass with minor corrections ; 3) Pass with major corrections ; 4) Re-write thesis ; 5) Fail

IT SKILLS

- Borland Delphi, Mathcad, MS Visual C++, Matlab, COMSOL (beginner)
- VHDL

LANGUAGES

- English, Chinese Mandarin, French, Malay (notions)
- Dialects : Teochew, Hokkien, Cantonese
- **French** : 06/1997 – Diplôme d'études de la langue française (DEL F), Université de Nantes
06/2002 – Diplôme approfondi de la langue française (DALF) – EMN

PROFESSIONAL MEMBERSHIP & MISCELLANEOUS

- Member SPIE (2007-2011 and 2013–)
- Leisure: rowing, swimming, reading